Decomposition of Pharmaceuticals and Personal Care Products by Water Plasma

金, 淳浩

Decomposition of Pharmaceuticals and Personal Care Products by Water Plasma

令和 4 年度　博士論文

九州大学大学院工学府 化学システム工学専攻

第 5 講座 KIM SOONHO

Contents

1. Introduction

1.1 Plasma Definition

Plasma is defined as the fourth state of matter which is composed of electrons, ions, and neutral particles, and the atmosphere is overall electrically neutral [1,2]. The solid is a ground or first state of matter at the lowest temperature with a specific enthalpy value. As shown in **Fig. 1.1** [1], the meting of solid starts with the increase of the specific enthalpy corresponding to temperature increase. It reaches the liquid state which is the second state of matter. With the further rise of the specific enthalpy, the temperature increases until the vaporization temperature point of the liquid, which results in the vapor phase. Then, the vapor phase as the third state of the matter finally reaches the fourth state of matter that is to say the plasma state by a consecutive increase of the specific enthalpy. In the plasma state, molecules are dissociated, and atoms are ionized resulting in forming a mixture of molecules, atoms, and ions in local electrical neutrality. For instance, more than 99% of the revealed universe is the state of plasma including the sun and furthermore, lightning, fluorescent lamps, and neon lights are also in the plasma state [3–5].

The ion and neutral are much heavier than the electron. In the case of the hydrogen atom as the lowest atom mass, the mass ratio of hydrogen atom and electron is 1836. Therefore, ion as well as neutral are called as heavy particles. The mixture of neutrals, ions, and electrons can be considered to be plasma only if they are balanced positively or negatively. This characteristic is known as quasi neutrality, by which plasma conducts electricity with a conductivity close to that of a molten salt state because of a significant degree of ionization [6]. The distinctive characteristic of plasmas allows for the maximization of chemical processes and increases their efficiency and chemical reactions which are hard to be obtained in typical chemistry [5].

Plasma is classified by a wide range of criteria, of which it can be divided based on its origin as

natural or man-made plasmas. The classification is shown in **Fig. 1.2** [1]. The different kinds of plasmas are indicated by the electron temperature (T_e) according to the number density of charged particles (m^{-3}). The electron densities (n_e) corresponding to pressure (p) variations are in the range of 10^8–10^{24} (m^{-3}). The electron temperatures (T_e) are represented regarding electronvolt (eV) (1 eV is about 7,740 K for a Maxwell-Boltzmann plasma) and Kevin (K) [3].

As natural plasmas, the ionosphere exists at a relatively low temperature range near 0.1 eV or 10^3 K in the condition of the low number densities of charged particles or pressure. On the other hand, the nebula and solar corona are located at nearby 10^6 K. Lightning can be observed most among natural plasmas at nearby atmospheric pressure and above.

Most man-made plasmas are characterized by energy levels around 1 to 2 eV corresponding to temperatures between 10,000–20,000 K, where high-pressure arcs and radio frequency (RF) discharges are included. Moreover, glow discharges, flames, microwave (MW) plasmas, and dielectric barrier discharges (DBD) fall in man-made plasmas with relatively low temperature. In particular, they can be also divided by the degree of ionization which is defined as $\xi = n_e / (n_e + n)$ where n_e and n represent the number densities of electrons and particles (m^{-3}), respectively. The flames are low at 10^{-10} and high-pressure arcs show a few percentages in the range of 5–10%. Thermonuclear fusion plasmas are characterized by extensive ionization levels.

Here, the abovementioned plasmas can be often subdivided depending on temperatures. For instance, thermal and non-thermal (or cold) plasmas are considered as low temperature plasma, and they which have been widely applied to industrial fields [1].

1.2 Thermal Plasma

1.2.1 Definition of Thermal Plasma

The plasma technology for industries primarily utilizes two different plasmas such as “thermal plasma” or “equilibrium”, and “cold plasma” or “non-equilibrium” [7,8]. The plasma close to local thermodynamic equilibrium (LTE) is known as thermal plasma. It provides a distinct flow with high temperatures of electrons as well as heavy species including strong light emission, various properties, and active chemical reactions [9].

The collision between heavy particles (ions and neutrals) and electrons most significantly affects the maintenance and generating plasma. Under the applied electric field, the ions and electrons are accelerated with obtaining energy in the plasma, and then the energy is exchanged. The exchange of energy can occur between the same species or different species by direct collisions.

The exchanged energy between two species with masses m_1 and m_2 is proportional to $2m_1 \cdot m_2 / (m_1 + m_2)^2$ [10]. However, this is not corresponded to electrons due to a very low mass. Therefore, the energy exchange is very small in the case of collision between an electron and a heavy species, which is proportional to $2m_e / m_h$, where m_e is an electron mass and m_h is the mass of the heavy species. Therefore, there will always be a temperature difference between them in plasma with a high collision frequency. The temperature difference can be expressed as follows:

$$\frac{T_e - T_h}{T_e} = \frac{3\pi m_h}{32 m_e}\left(\frac{e l_e E}{\frac{3}{2}kT_e}\right)^2 \tag{1.1}$$

where T_e and T_h represent the electron and the heavy particle temperatures, respectively. e, E, and l_e mean the elementary charge, the electric field, and the mean free path of electrons, respectively. k is the Boltzmann constant. If assuming $l_e \sim \frac{1}{p}$ (p is pressure), Eq. (1.1) can be given as follows:

$$\frac{T_e - T_h}{T_e} = \frac{\Delta T}{T_e} \sim \left(\frac{E}{p}\right)^2 \tag{1.2}$$

The ratio of an electric field to pressure (E/p) therefore is important in the temperature deviation between T_e and T_h, and this manifests the kinetic equilibrium of plasma. Here, the temperature of

heavy particles reaches the electron temperature when *E/p* is small by a decrease of E, an increase of p, or both. This is essential for LTE plasma. Excitation and chemical equilibrium in the plasma gradient are also required [11–13]. Here, plasma satisfying all the above conditions is called thermal plasma with high energy density and temperature equality between the heavy particles and the electrons [8]. Non-equilibrium plasmas, on the other hand, have a lower degree of ionization, which result in lower energy density and a large temperature gap between the electrons and the heavier particles. These plasmas are also identified with "cold" plasmas.

The detailed characteristics of thermal and non-thermal plasma are summarized in **Table 1.1** [7,14]. Thermal plasmas are generated at pressures of over 10 kPa with a high temperature over 10^4 K and a relatively high electron density (the order of 10^{21}–10^{26} m^{-3}). In contrast, non-equilibrium plasmas are generated at pressures under 10 kPa or less up to atmospheric pressure. Temperature and electron density are less than 10^4 K and 10^{19} m^{-3}, respectively. Therefore, the distinctive properties of these two categories of plasmas give rise to different processing applications.

1.2.2 Characteristics of Thermal Plasma

The characteristics of a thermal plasma highly rely on the thermophysical properties of the plasma gas. The properties are mainly separated into three properties: plasma composition, thermodynamic properties, and transport properties [15]. They contribute to the modeling and application of thermal plasma.

1.2.2.1 Plasma Composition

Plasma composition is calculated by minimization of the Gibbs free enthalpy, considering the van't Hoff's laws for dissociation and ionization, the conservation of different elements, the electrical neutrality, and Dalton's law [3]. Results are indicated by the number densities of species

with respect to the temperature under specific pressure.

Since the molecular components used for plasma gas are nearly dissociated and atomic species are also ionized in thermal plasma, the energy is transported by transfer of kinetic energy as well as the heat of dissociation and ionization [16]. Especially, the heat is more efficiently transported by higher thermal conductivity than that of gases.

Table 1.2 shows the ionization and dissociation energies of various plasma gases [10]. Therefore, the number density of plasma gas species will vary at the same temperature in different plasma gases, by which thermodynamic and transport properties can be controlled and changed.

1.2.2.2 Thermodynamic Characteristics

The thermodynamic characteristics of plasma are characterized by many factors such as enthalpy, specific heat, mass density, internal energy, and entropy.

The specific enthalpy in plasma is heavily reliant upon the dissociation and ionization of plasma gases. The specific enthalpy (MJ/kg) of the various plasma gases with respect to temperature is shown in **Fig. 1.3** [10]. The steep change of enthalpy is attributed to the dissociation and ionization, where the high enthalpy in H_2 results from the low mass. On the other hand, due to higher ionization energy, the ionization of He is difficult.

The monatomic gases generate ionic species. For example, Ar and He are ionized to Ar^+, Ar_2^+, and He^+ with free electrons [17]. The diatomic gases such as N_2 and H_2 have higher enthalpies for a given temperature. This is concerned with the molecular structure for dissociation, which is followed by ionization. Therefore, the specific enthalpy of plasma can be increased and changed by the addition of different gases like He or H_2 [18]. The internal energy, the specific heat, and the entropy also have a significant contribution to the evaluation for the thermodynamic functions [2].

1.2.2.3 Transport Characteristics

(a) Thermal conductivity

Thermal conductivity (κ) controls the energy losses during the plasma discharge with heat transfer from plasma to the material. Therefore, this is an important factor for thermal plasmas. The thermal conductivity is deduced from Fourier's law which is expressed as follows:

$$\vec{q} = -\kappa \cdot \text{grad}\, T \tag{1.3}$$

where $\vec{q}$ is the heat flux (W/m^2), κ is the thermal conductivity (W/m·K), and grad T is the temperature gradient of plasma (K/m). Thermal conductivity is the sum of three components as follows:

$$\kappa_{total} = \kappa_{tr}^{h} + \kappa_{tr}^{e} + \kappa_{R} \tag{1.4}$$

where κ_{tr}^{h}, κ_{tr}^{e}, and κ_R are the translational thermal conductivities of heavy species and electrons, and reactions, respectively [10,19]. **Figure 1.4** shows the change of thermal conductivity with an increase of H_2 in an Ar-H_2 mixture, in which the changes of peaks are associated with dissociation and ionization reactions [10].

(b) Electrical conductivity

Plasma is an electrically conductive fluid flow of electric charges such as electrons and positive ions of plasma gas in the presence of an electric field. Here, the characteristic of electrical conductivity (σ_e) in the electric charges has a significant effect on the current density as well as the heat flux of plasma [14]. Electrical conductivity (σ_e) is deduced from Ohm's law and is expressed as follows:

$$\sigma_e\ (S/m) = \frac{n_e e^2}{\sqrt{2Tm_e} n_a \sigma_{en}} \tag{1.5}$$

where n_e is the electron density, e is the electron charge (1.6×10^{-19} As), m_e is the electron mass, T is the plasma temperature, n_a is the neutral particle number density, and σ_{en} is the electron-

neutral collision cross section. The electrical conductivity is proportional to the electron density. The electrical conductivities are to a certain degree close for various gases because of their similar ionization energies of them as shown in **Fig. 1.5** [4]. However, this is not related to He showing a significant difference due to higher ionization energy.

(c) Viscosity

The viscosity is one of the key parameters in determining the characteristic of plasma fluid, i.e., velocity and diffusion of plasma [20]. The viscosity (μ) is proportionate to the square root of the atomic mass and is also inverse proportion to the collision cross-sections of the species, which is expressed as follows:

$$\mu\ (kg/m \cdot s) = \frac{2}{3\sqrt{\pi}} \frac{\sqrt{mkT}}{\sigma_0} \tag{1.6}$$

where m is the particle mass, σ_0 is the total collision cross section, and k is the Boltzmann constant.

The values of viscosity for various plasma gases according to temperature are presented in **Fig. 1.6** [10]. H_2 has the lowest viscosity due to low mass. The weak collision cross-section for interactions between He atoms results in a relatively higher viscosity despite of low mass. Moreover, the strong Coulomb interaction does not dominate the collision cross-sections until temperatures of around 20,000 K since He can be ionized at a high temperature. This means that the viscosity of He is maintained high until about the above temperature. The viscosity for Ar and He decreases over 20,000 K by the long-distance interactions between charged particles.

1.2.3 Classification of Thermal Plasma

Various methods are commonly applied to generate thermal plasmas, such as direct current (DC) arc, alternating current (AC) arc, radio frequency (RF) thermal plasma, and microwave (MW)

plasma. Schematic diagrams of thermal plasma generation methods are shown in **Fig. 1.7**, and more detailed discussions will be presented as follows.

1.2.3.1 DC Arc

DC arc is classified into two categories namely, DC non-transferred and transferred arc depending on the arrangement of electrodes [21]. These have been mainly applied to the pyrolysis of liquids and gases, synthesis of nanopowders, and waste treatment [22].

DC non-transferred arc torches have been widely used for spray coatings, synthesis, and waste decomposition [23,24]. They produce an arc with a high temperature that interacts with plasma gas and then a hot plasma jet is generated, by which the material can be injected for vaporization. A schematic diagram of a DC non-transferred arc torch is shown in **Fig. 1.7** (a). Here, an arc is formed between cathode and anode. The anode is parallel to the plasma jet. The plasma gas is crossed between the arc column and the anode's inner surface, and then is pushed from upstream to downstream by the pressure of the gas flow in the torch.

The DC transferred arc is distinguished by a distinct separation between the cathode and anode as shown in **Fig. 1.7** (b) [25]. The distance between electrodes can be controlled by a few centimeters. Torches can be anodic or cathodic and the electrode is coaxial with the plasma jet. The arc is transferred to the external electrode that is usually the workpiece as the electrically conductive material. In particular, DC transferred arc torches can produce intense thermal fluxes because the arc is not affected by the water cooling of the torch [26]. This manifests that they have higher efficiency than DC non-transferred arc torches because of the minimization of radiant heat transfer losses to the cold torch body. DC transferred arc torches are usually used for plasma welding, cutting, and particle formation [27,28].

1.2.3.2 Multiphase AC Arc

Multiphase AC arcs have been highlighted for innovative nanomaterial synthesis and in-flight technology. Compared to DC arcs showing a high velocity of the plasma gas, the multiphase AC arcs have low velocities, long residence times of particles as well as large high-temperature volumes. Therefore, these characteristics are highly advantageous to evaporate the treated materials in multiphase AC arcs [29].

Three-phase AC arc plasmas were applied to plasma welding, nanoparticle synthesis, and particle spheroidization [29,30]. However, these processes were not adapted for large-scale production due to the economic aspect such as electrode erosion and energy consumption, and low yield of synthesized particles.

Multi 6-phase or 12-phase AC arcs have been developed and investigated to address the above challenges [31–34]. The arc distribution of multiphase AC arc plasma with 12-phase is presented in **Fig. 1.7** (c). The symmetrical arrangement of 12 electrodes is placed by the 30° where the electrodes are organized by 2 layers: 6 electrodes are divided into the upper and lower layers, respectively. The above multiphase AC arc generator is characterized by a high energy efficiency of 70–90%, low plasma velocity, and large plasma diameter. Based on the advantages, multiphase AC plasmas are suitable for producing functional materials such as in-flight material, spheroidization, nanoparticles, and waste treatments in terms of their large plasma volume and low flow velocity [34–36].

1.2.3.3 Radio Frequency Plasma

Radio frequency (RF) plasma is generated by high-frequency current flowing in a coil surrounding the chamber. The frequency varies from 2 to 27 MHz [13]. An illustration for RF plasma is shown in **Fig. 1.7** (d).

The electric field generated by the induction coil is induced inside the chamber and initiates a current along a ring-shaped route inside the chamber generating the plasma. RF plasmas operate in the absence of electrodes, which prevents the plasma from being contaminated by the vapors from electrode materials. RF plasma technology possesses the advantages such as a relatively large volume of plasma and low velocity of plasma gases, which enable many particles to be melted [37]. RF plasma torches have been gradually taken into account for the synthesis of nanoparticles and the destruction of hazardous gases [38–41].

1.2.3.4 Microwave Plasma

Electromagnetic radiations in the frequency range from 300 MHz to 10 GHz generate microwave (MW) plasma without electrodes. MW plasma torch is shown in **Fig. 1.7** (e). MW plasmas work at usually 2.45 GHz and are generally denser compared to RF plasmas [42]. In addition, the area affected by MW plasma is larger. Therefore, MW plasmas produce a higher concentration of active species than other plasma techniques, which would be effective for the degradation process of gases and liquids together with material synthesis [43–46].

MW plasma can be more divided into several categories such as surface wave discharges, cavity-induced plasma, electron cyclotron resonators, etc. Moreover, all of the MW-induced plasmas operate in a wide range of operating conditions such as variable power from a few W to several hundred kW and pressure from around 0.1 Pa to over a hundred kPa, using both noble and molecular gases [42,47,48].

1.3 Application of Thermal Plasma

1.3.1 Spraying and Coating

Plasma spraying is one of the primary technologies to protect the surface of a substrate or improve its function with various coating thicknesses from a few hundred micrometers to a few millimeters. The applied industrial fields are aeronautics, industrial gas turbines, biomedical, automotive, and electronics [49].

The versatile character of the plasma spraying allows easier deposition for various materials. The ceramics, metallic alloys, and composites can be deposited to protect a substrate when used in aggressive environments such as high temperature, severe wear, and corrosion [50–52]. The energy source in plasma spraying torches is an electric discharge that can be generated by either a DC non-transferred arc source (DC plasma spraying) or a radio frequency (RF) discharge (induction plasma spraying) [10,53]. For both of plasma secures, typical operation conditions for power are between 30 and 100 kW and maximum powder flow rates are in the range of 6–18 kg/h [54].

1.3.2 Welding and Cutting

Thermal plasmas have been extensively applied to metal welding and cutting as a well-established technology. Arc plasma is used for welding by the transfer of intensive energy to one of the electrodes, the workpiece, which is composed of the metal components to be joined. This results in the melting of the workpiece and forms a weld pool. There are some kinds of thermal plasma welding. Both tungsten inert gas (TIG) and metal inert gas (MIG) welding processes are used broadly [55]. A transferred arc is usually used in TIG, where the tungsten electrode performs as the cathode and the external anode is the workpiece. Gas mixtures or an inert gas such as Ar and He flows to restrain contamination along the cathode from the surroundings. In the case of MIG welding, the arc is generated between the workpiece and a wire electrode. Here, the wire electrode is kept being supplied from inside the torch at constant speeds. At the same time, inert gas is fed

from the torch to the weld zone, which protects the weld from contamination by the atmosphere [56]. In addition, submerged arcs can be also used for welding.

Plasma cutting is another well-established technology. This is applied to cut conducting material using a high current in the range from 30 to 1,000 A between the cathode and the workpiece [57,58]. Plasma torches for cutting with a stick- or button-type cathodes made of tungsten or hafnium are used with plasma-forming gas [59,60]. The specific heat fluxes into the workpiece are higher than for arc welding with at least one order of magnitude. This difference implies that the arc for plasma cutting has to be constricted intensively, which finally leads to high current densities and high temperatures of arc, even at relatively low currents at 20 A.

1.3.3 Metallurgy

Thermal plasma is used for plasma metallurgy such as direct reduction of oxide ores, carbon reduction smelting of metal oxides, decomposition of ores, and reduction of chlorides, etc. [7]. Plasma furnaces have a high melting efficiency and can produce alloys with low contents of carbon, hydrogen, and oxygen. The transferred arc plasmas are usually used in the metallurgical industry because of high-efficiency concentration, high thermal efficiency, excellent heat and mass transfer conditions, and adequate residence time. Nanoparticles of titanium oxides (TiO_2) used for manufacturing paints, varnishes, and lacquer were completely prepared from ilmenite ($FeTiO_3$) powder as a precursor using a DC non-transferred arc at atmospheric pressure [61]. Furthermore, RF plasma source with Ar and H_2 injection was conducted for the purification of metallurgical grade silicon [62].

1.3.4 Synthesis of Nanoparticles

Nanoparticles are expected to be potential next-generation materials for various applications

such as in electronics, energy, and environmental fields. This is because they have unique physical and optical properties unlike their bulk materials [63]. In particular, nanoparticle synthesis by thermal plasmas has been advantageous due to the fact that thermal plasma is used as a high-enthalpy source for the evaporation of raw material [64]. DC arcs are one of the reliable tools widely used for nanoparticle synthesis. For example, cubic boron nitride nanoparticles which have received attention for their high hardness and high thermal conductivity were synthesized by DC non-transferred arc [65]. Furthermore, the RF thermal plasma is nearly uncontaminated by impurities due to no electrode. This reduction of contamination from the electrodes is beneficial for the synthesis of pure nanoparticles. nitrides [66], carbides [67], and lithium metal oxides for solid oxide fuel cells [68,69] were successfully synthesized.

1.4 DC Arc Discharge

The regions between the electrodes in the DC arc are separated into three regions: the cathode region, the anode region, and the arc column region. The characteristics of these regions including arc attachments of both electrodes and arc further fluctuation phenomena are introduced in the following subsections.

1.4.1 Cathode Region

1.4.1.1 Characteristics of Cathode Region

The near-cathode region for high-pressure arcs consists of two zones: the space-charge sheath and the ionization layer [70–72]. In the space-charge sheath layer, the electron is emitted from the cathode surface by a high temperature of the cathode surface and high electric field. While the electric field decreases the effective work function of the cathode, it is not enough to provide

electron tunneling through the cathode. The combined emission mechanism is called the thermo-field emission [73]. The thermionic emission from the cathode is described by the Richardson-Dushman equation as follows:

$$j_s = AT^2 exp\left(-\frac{W}{kT}\right) \tag{1.7}$$

where j_s is the current density of the emission (mA/mm^2), A is Richardson's constant (mA/mm^{2}K^2), W is the work function of cathode materials (J or eV), k is the Boltzmann constant, and T is the cathode temperature (K). A is multiplied by a correction factor depending on the cathode material. For example, the correction factor of tungsten is 0.5.

If electrons emit through the collision less space-charge sheath, the electrons collide and ionize the neutral particles from the cathode in the ionization layer. The ions are also accelerated toward the cathode where ions recombine with the release of their kinetic and potential energies on the cathode surface. The ionization layer above the space-charge sheath layer is a state of quasi-neutral [74]. The sum of the length of the two layers is generally less than 0.1 mm, which leads to high electric fields [75].

1.4.1.2 Cathode Attachment

The observations of the cathode region show that the arc attachment is composed of one or several, and mobile spots. The spots split into smaller in the range of 10–100 μm during the movement of the attachment on the cathode surface. And the current per spot is dependent on the cathode material and is in the range of 0.5–300 A [76].

The major factors determining the cathode attachment and its erosion rate are highly associated with the electrode material like hot cathode or cold cathode, the arc current, and the kind and pressure of the plasma gas [77].

Spot or spotless diffuse modes are mainly formed as the arc attachment on hot cathodes [78,79].

The spot mode is featured by a contraction of the arc in front of the cathode. The spot mode is typically characterized by low current and large cathode diameters, which develops the extreme local cooling at the attachment. The diameter of the attachment is about a few tenths of millimeters. On the other hand, the diffuse mode can be formed by higher current or smaller cathode diameters. The current density of this mode is approximately 10^6 A/m^2. The arc is stable and covers a wide area of the cathode surface. The surface average temperature is higher than that in the spot mode without the local melting, which less damages the cathode [80].

1.4.2 Anode Region

1.4.2.1 Characteristics of Anode Region

The electric current from plasma to the anode is mainly flowed by the electrons [81,82]. The anode region shows a sharp gradient in temperature where the temperature decreases from the arc column temperatures (8,000–15,000 K) to the anode surface temperatures of several hundred degrees with a drop of electron density.

In the case of the high-intensity arcs more than 50A, a relatively dark layer is seen with a thickness of about 1 mm from the anode surface which is called the anode boundary layer [11]. From the edge of the anode boundary layer to the anode surface, there are primary three zones as follows.

At the edge of the anode boundary layer, the axial heat flux to the cold anode disturbs the plasma energy balance. Then, at the above edge of the anode boundary layer, deviation from thermal equilibrium occurs because of the different temperatures between the electrons and heavy particles as shown in **Fig. 1.8** [11]. Finally, an electrical sheath occurs in the layer close to the anode surface, in which the plasma doesn't maintain quasi-neutrality.

1.4.2.2 Anode Attachment

The shape of the anode arc attachment affects the anode lifetime. The anode attachment is classified into diffuse and constricted modes [11,83,84]. An experimental setup with a rod-shaped cathode located perpendicular to a flat anode was used to investigate the anode attachment [75,85]. The diffuse mode generally occurs in the cathode jet which is attributed to Lorentz force [86]. As the arc contracts, the bent current lines produce an axial component of the magnetic force, which results in a strong plasma flow toward the anode.

The effect of the cathode jet decrease with an increase in the distance between the electrodes. Then, the arc contracts due to the cooling of the arc periphery near the cold anode surface. This results in constricted anode attachment mode forming one or several spots with generating an anode jet.

Hartmann and Heberlein presented the effect of an external gas flow on the anode attachments using DC transferred arc [87]. The result showed that additional axial gas flow from a surrounding coaxial nozzle pushes the plasma toward the anode, which finally reduces the thickness of the anode boundary layer, and the diffuse mode is preferred.

1.4.3 Arc Fluctuation Phenomena between Electrodes

As discussed in the previous section 1.3, DC non-transferred arc has been broadly applied to many industrial fields such as spraying, coatings, synthesis of material, and further waste treatment. Here, one of the major aims for plasma processes above is to achieve better reproducibility [88]. Therefore, a better understanding of the dynamics of the arc inside the plasma torches is required. This is because the arc movement between the electrodes influences plasma consistency, process quality, and electrode lifetime [89]. Therefore, many practical experiments including numerical simulations have been extensively examined [90–94].

The arc dynamics are caused by the balance between the drag force and the electromagnetic (or Lorentz) force. The drag force results from the interaction of the gas flow pushing the arc to downstream and the Lorentz force is a result of the local curvature and thickness of the arc [90]. The change of the voltage drops with time provides information on the arc dynamics inside the torch since the arc length depends linearly on the voltage drop. This fact offered three distinct modes in the operation of the torch [90,95,96]: steady, takeover, and restrike. These modes are indicated in **Fig. 1.9** [96]. These modes are as follows:

(a) Steady mode: The mode occurs when the drag force and Lorentz force are balanced where the voltage fluctuation is approximately flat during the arc movement. This makes the arc stay at the almost same spot on the anode, which causes overheating and substantial erosion of the anode.

(b) Takeover mode: This mode shows random fluctuations. These fluctuations are characterized by a change of the shape in the arc radial section and gradual movement of the anode attachment position. The fluctuation of the mode shows the order of 20–50% of the average arc voltage.

(c) Restrike mode: This mode has the largest voltage fluctuations and shows a sawtooth shape. The arc attachment moves downstream until the arc reattachment occurs upstream on the anode surface near the cathode. The fluctuation is in a range of 40–100% of the average arc voltage with frequencies of up to 7 kHz in accordance with the conditions in operation [97].

The arc mode can be changeable according to the thickness of the anode boundary layer. The restrike mode is favored at higher gas flow rates, at lower currents, or with gases having higher thermal conductivity such as H_2 and He. The anode erosion can be reduced in the restrike mode due to the rapid fluctuation. However, the large fluctuation may influence the process consistency due to the power variation in the torch.

1.4.4 Arc Temperature

The DC arc is characterized by a high plasma temperature and a high gas velocity of about 100–1,000 m/s at the center axis, which is allowing to vaporize various materials having even a high melting or boiling point [98,99]. Therefore, the temperature is considered an important parameter to manage the process developments in plasma spraying, plasma synthesis applications, and waste treatment [10,100].

There are many methods to measure the thermal plasma temperature. The Langmuir probe as a contact method placed to near a plasma jet is a simple and flexible diagnostic tool. However, the probe can disturb the parameter distribution of the source. Moreover, the interpretation procedure of the data obtained is difficult due to the complex and comprehensive underlying theory for high-temperature thermal plasmas [101–104]. Therefore, non-contact measurements such as spectroscopic and high-speed camera methods are widely used, and a more detailed discussion will be presented as follows.

1.4.4.1 Spectroscopic Method

The spectroscopic method is one of the most widely used assessment methods for the sake of investigation of thermal plasmas. This method has advantages for the measurement of spatially limited points and lines in plasma. From the obtained spectroscopic results, the plasma temperature can be calculated using several different methods where the atomic line intensities, intensity ratios of two or more spectral lines, or the ratios of line-to-continuum intensity are usually used [105,106].

The plasma temperature in the DC arc was calculated [75], where the Fowler-Milne method under the assumption of LTE was adopted [107,108]. This method doesn’t require the calibration of the sensitivity of the apparatus and knowledge of atomic transition probabilities. The result showed that the experimental result was in good agreement with analytical predictions: an arc

current was 20 A and the distance between electrodes was 10 mm. The highest temperature was 21,000 K near the cathode tip.

Temperature measurement of DC non-transferred arcs used for arc cutting has been reported [109,110]. Temperatures and electron densities in the arc were measured using different emission lines and several different methods for property calculation. Fluctuations in the arc intensity, arc asymmetry, and the validity of the assumptions used for property calculation were proven to affect the accurate measurements. The arc temperature in the center was about 25,000 K when using oxygen atoms and ions in an oxygen plasma with an arc current of 200 A. Also, better measurement was shown in using oxygen ions than oxygen atoms with less error.

1.4.4.2 High-Speed Visualization

The spectroscopy method has difficulty observing arcs showing periodic behavior in a short time because the spatial resolution is low, and the measurement time is long. Therefore, the arc temperature measurement method by a high-speed camera has been proposed. This method can measure a wide area with a higher temporal resolution. In particular, the two- or three-dimensional plasma temperature can be measured. In the TIG arc at an arc current of 100 A, 125 A, 150 A, and 200 A, the highest plasma temperature was 20,000 K. The validation was conducted by different attempts utilizing a spectrometer, and the results showed highly identical to the plasma temperatures measured at stationary arcs [111].

Okuma et al. measured the arc temperature using a high-speed camera in a 12-phase AC arc [112]. The arc temperature was conducted by the Boltzmann plot method using two types of argon line emissions (675.2834 nm and 794.8176 nm) filtered by the band-pass filters. The obtained excitation temperature was high with a range of 7,000–13,000 K. They also measured the arc temperature fluctuation in cathodic and anodic periods, where the temperature was 7,000–14,000

K and 7,000–9,000 K during the cathodic and anodic periods, respectively. Furthermore, the fluctuation frequency of arc and the residence time of the raw material were also investigated, in which the fluctuation frequency and the residence time were 720 Hz and 1.4 ms, respectively. From this result, a multiphase AC arc could be suitable for material processing with a high temperature of over 7,000 K at the center of the arc area.

1.5 Waste Treatment by Thermal Plasma

Thermal plasmas are applied to treat a wide range of wastes, for example, municipal solid waste (MSW), sewage sludge waste (SSW), harmful organic compounds, greenhouse gases, etc. They transfer high heat fluxes of high temperatures and reactive species, which allows the destruction of any type of waste [2]. Moreover, thermal plasmas provide distinctive advantages such as high enthalpy, high reactivity, oxidation and reduction atmosphere, and rapid quenching rate, which lead to [113–115]:

(1) High heat transfer rate

(2) Melting of materials at high temperature

(3) Low gas flow

(4) Small torch and reactor

(5) The feasibility of producing saleable byproducts

Therefore, thermal plasmas can be specialized for waste treatment. A large number of research articles published have treated contaminants of various types, and more detailed discussions will be presented as follows.

1.5.1 Solid Waste Treatment

1.5.1.1 Municipal Solid Waste

An increase in population, consumerism and industrial development has led to increased quantities of municipal solid waste (MSW) [116]. MSW is more commonly known as trash or garbage. It consists of everyday items that are used and then discarded, such as product packaging, furniture, bottles, clothing, newspapers, food scraps, paint, etc. Accumulation of MSW causes harmful emission of gases, and therefore some methods for storage require large tracts of land [2]. The World Bank reported that there are currently urban residents of 3 billion producing 1.2 kg/person/day of MSW and that number will grow to 4.3 billion urban residents producing 1.42 kg/person/day of MSW by 2025 [117]. From this perspective, thermal plasmas are widely employed to treat MSW around the world.

Byun et al. [118,119] have developed a MSW plant allowing for treating 10 tons of waste per day to observe the feasibility of the process in real-time. The volume reduction rate of MSW to slag was up to 99%. This value is higher than a MSW process using a fuel-burning melting system (90%) [120]. Qinglin et al. investigated the effect of steam injection using a pilot-scale thermal plasma gasification system for the destruction of MSW [121], indicating that the cold gas efficiency and syngas yield were improved with the increase of steam injection. And the maximum energy efficiency of the tests showed 58%.

Furthermore, DC transferred arc was applied to remove the MSW incineration residue [122]. A trace quantity of toxic heavy metals such as Pb and Cd was contained in the residue. As a result, the capacity of 25 tons per day was acquired at a power of 1,710 kW. Also, the furnace maintains a reducing atmosphere inside, where no NO_x is generated. After treatment, the glass-like slag could be used as materials for pavement bricks and concrete slabs due to the nontoxic.

There are also many studies to utilize syngas generated after plasma treatment. Van Oost et al. [123] gasified crushed wood as a model substance using a novel gas-water stabilized plasma torch.

They verified the influences of variable feed rate, plasma gas flow rate, and the introduction of CO_2 on the gasification process. They proved that a proper mixing between the reactants and plasma could be obtained even at low plasma flow rates, and more intense mixing was achieved at high feed rates. The effects of the presence of O_2 and CO_2 on plasma gasification were also secured from this research.

1.5.1.2 Sewage Sludge Waste

Sewage sludge waste (SSW) is from the sewage treatment plant and contains considerable amounts of heavy metals, organic toxins, as well as pathogenic microorganisms [124]. Therefore, they have negative effects on the soil, ground and surface water, animal, and human health.

The sewage sludge was gasified by thermal plasma using water steam as the plasma-forming gas and a chemical reagent [125]. The composition consisted of sewage contained approximately 60% mass organic and approximately 40% mass inorganic substances such as SiO_2, Al_2O_3, Fe_2O_3, MgO, and CaO. In this study, sewage sludge was gasified into mainly carbon monoxide of 48% and hydrogen gases of 46% at an electric power of 15 kW. Moreover, due to the high reaction temperature of up to 1,700°C and the absence of an oxygen environment, as well as the rapid cooling, dioxins and furans were not formed. Furthermore, Montouris et al. determined that plasma gasification of sewage sludge from Psittalia Island using the equilibrium gasification model and produced electricity [126]. Assuming processing of 250 tons per day of sewage sludge with a 68% moisture content, the installation has shown the possibility to supply electric power of 2.85 MW.

A microwave plasma reactor was applied to reform raw syngas derived from sewage sludge gasification. The result showed that applying plasma resulted not only in the decrease of tar content with the conversion from 70 to 100% but also in a considerable improvement in the gas composition [127].

1.5.1.3 Medical Waste

According to the World Health Organization (WHO), medical waste (MW) includes all the waste produced from hospitals, healthcare facilities, research centers, and laboratories related to medical procedures [128]. Hazardous MWs are assumed to occupy 15% of the total waste production in a hospital and that value can also be increased up to 35% [129].

A plant using 50 kW DC plasma torches has been developed for the destruction of medical waste [130]. A screw conveyor was equipped to convey the medical wastes with a maximum mass of 40 kg/h. In the chamber, the plasma jet produced from the plasma torch transfers heat to the medical wastes. Finally, they are converted to CO_2 and H_2O and melted in an O_2 environment. The temperature inside the chamber was in the range of 2,000–2,500 °C.

On the other hand, for these hazardous and non-combustible medical wastes, another method was used where the vitrification process can obtain a glassy and leach-resistant product that solidifies and stabilizes toxic substances [131,132]. The medical wastes were treated using thermal plasma by the Institute of Nuclear Energy Research (INER) in Taiwan [133]. The feedstock contained a high ratio of noncombustible substances such as stainless steel and glass. A DC non-transferred arc torch was used with a power of 100 kW over 10,000 °C. Ar gas was used as the plasma-forming gas for ignition and then the air was injected during the treatment. The vitrification was conducted for 15 min at 1,550 °C. As a result, two macroscopic components were obtained: vitrified glassy slag and ellipsoidal metal nugget.

1.5.2 Gaseous Waste Treatment

1.5.2.1 Perfluorocarbons

Perfluorocarbons (PFCs) such as CF_4, C_2F_6, SF_6, and NF_3 have been widely used for plasma

etching and plasma cleaning deposition chambers [134]. About one million tons of PFCs were used in the world in 1996. However, PFCs are long-lived compounds and have persistence in the atmosphere. Moreover, they are considered infrared absorbers and significant contributors to global warming [135,136]. Consequently, at the Conference of the Parties (COP-3) in Kyoto, Japan, in December 1997, PFCs were adopted as greenhouse gases by 159 nations. If PFCs are discharged without appropriate treatment, they will be surely restricted by the Kyoto agreement as a source of greenhouse gas disposal [137].

CF_4 decomposition by DC arc at 6–9 kW was conducted to find the optimum conditions according to parameters such as flow rate, input power, and addition gases. [138]. The result showed that CF_4 decomposition was inversely proportional to the flow rate of CF_4, and the decomposition rate was higher at a flow rate of 15 L/min Ar than that of 10 L/min. However, plasma input power has an effect only a little on the decomposition. Moreover, the CF_4 decomposition rate was over 95% by using additional O_2 and H_2 gases by preventing the reformation of CF_4. Finally, the optimum flow rate ratio for reacting gases was suggested.

Another study of nitrogen trifluoride (NF_3) decomposition by DC arc was reported by Ko et al. in 2013 [139]. The highest destruction and removal efficiency (DRE) of NF_3 was achieved with 97% at a gas flow rate of 100 L/min with low electric power of 2 kW. They also confirmed that additive gases have a significant effect on the thermal decomposition of NF_3 using the FT-IR measurement, where H_2 addition converted NF_3 to HF.

Moreover, a microwave plasma torch was introduced for abatement of NF_3 and SF_6 at atmospheric pressure [140]. The decomposition rate of 99.1% in NF_3 was accomplished without an additive gas at the total flow rate of 50.1 L/min with a power of 1.4 kW. At the same power, the removal rate was 90.1% at the total flow rate of 40.6 L/min in the case of SF_6.

1.5.2.2 Hydrofluorocarbons

Hydrofluorocarbons (HFCs) are sorts of fluorinated compounds and have been identified as greenhouse gas due to their large global warming potential (GWP) and further long atmospheric lifetimes. Even though HFCs do not affect the ozone layer, most HFCs have considerable high global warming potentials (GWPs): the GWP of HFC-134a ($C_2H_2F_4$) is 1410 times with respect to CO_2 on a 100-year time horizon [141]. Synthetic greenhouse gases including HFC-134a have been regulated through an international agreement, the Kyoto Protocol due to their detrimental effects on the earth's radiative forcing. In addition, the European Union has recently adopted Mobile Air Conditioning (MAC) for motor vehicles to lower the level of HFC-134a [142].

Microwave plasma was introduced for the pyrolysis of HFC-134a at atmospheric pressure [143]. The HFC-134a at a flow rate of 50–212 L/min was introduced to the plasma. The total degree of removal in HFC-134a was up to 84% with the selectivity of 100% towards H_2, F_2, and C_2 at electrical powers of 0.6–3 kW, which can be used for industrial applications.

DC water plasma torch using 100%-water for generation of plasma was presented for HFC-134a destruction without additional chemicals [144]. The distinctive water plasma resulted in a portable light-weight system that does not require gas supply equipment, as well as the high energy efficiency because of no additional water-cooling system. The decomposition rate was 99.9% at a maximum feed rate of 160 g/h with 1 kW of arc power. CO, CO_2, and H_2 in the effluent gas and HF were formed after decomposition.

Among HFCs, HFC-23 (CHF_3) is mostly formed as a byproduct during the manufacturing process of HCFC-22 ($CHClF_2$), and they have been used as a refrigerant [145]. However, HFC-23 has a high GWPs of 11,700 times compared to CO_2 [146]. For this reason, regulation of the HFC-23 discharge into the air is essential. Commercial thermal decomposition methods such as conventional combustion and thermal plasma have been applied [147]. Choi et al. simulated the characteristic

of thermal flow inside a DC arc torch for the destruction of HFC-23 [148]. As a result, a high decomposition rate of over 99.5% was accomplished over 1,500 K where the arc current of 50 A was set for the decomposition temperature of HFC-23.

1.5.2.3 Chlorofluorocarbons

CCl_4, $CFCl_3$, and CF_2Cl_2 are included in chlorofluorocarbons (CFCs). A hydrogen atom is replaced with fluorine or another halogen element in a basic hydrocarbon compound [144]. They were widely used as refrigerants, propellants, and foaming agents for the manufacturing of plastics, insulating material, and cleaning solvents. However, the use of CFCs has been prohibited by the Montreal Protocol in 1987 as ozone-depleting substances (ODSs).

Jasinski et al. proposed microwave discharge for the decomposition of CFC-22 ($CHClF_2$) under the electrical power of 100 W at atmospheric pressure [149]. Their results showed that the decomposition efficiency reached almost 100%. Also, the energy cost of the decomposition of 1 mole, i.e., 86.5 g/h of $CHClF_2$ ranged from 0.4–2.0 kWh, which cost is 10–1,000 times lower than that of other plasma methods [150,151].

Foglein et al. have investigated the $CFCl_3$ decomposition using RF plasma [152]. The experiment was conducted with Ar and the mixture of Ar and O_2 at about 2 kW. The addition of O_2 in the argon-atmosphere reduced the formation of polyaromatic hydrocarbons (PAHs), which finally produced the main products of CFCs, CO_2, and Cl_2 and oxygen-contained aliphatic and aromatic compounds with depression of soot formation.

Furthermore, the decomposition of dichlorodifluoromethane (CCl_2F_2) has been studied by Sekiguchi et al. using the DC arc [153]. The results showed that CCl_2F_2 can be completely decomposed by the thermal plasma. Moreover, the addition of excess H_2 was effective in the reduction of Cl_2.

1.5.2.4 Methane

Greenhouse gases (GHGs) such as carbon dioxide (CO_2) and methane (CH_4) have altered Earth's climate by absorbing energy in the lower atmosphere and reemission [154]. Although anthropogenic emissions of CO_2 extremely contribute to GHG-induced warming, several other gases, such as methane (CH_4), hydrofluorocarbons (HFCs), sulfur hexafluoride (SF_6), and perfluorocarbons (PFCs), also have affected climate for decades to millennia after appearance. Their concentration will be increased, and further atmosphere will be warmer because most anthropogenic emissions of these non-CO_2 GHGs are connected to society's essential demands for energy and food [155,156]. In particular, the global warming potential (GWP) of CH_4 is 20 times that of CO_2, and CH_4 is the most abundant hydrocarbon among non-CO_2 GHG. Therefore, a proper treatment method is needed and urgent.

Pyrolysis of CH_4 via DC thermal steam plasma was applied [157]. The flow rates of CH_4 were 100 slm, 200 slm, 300 slm, and 500 slm with H_2O steam at 28 g/min, and the torch power was fixed at 52 kW. The highest conversion of CH_4 was 88% at 100 slm CH_4. The main effluent gas was H_2 and the solid was fine with a content of 99% carbon powder. The result was in good agreement with the equilibrium calculations.

Rutberg et al. reported on the production of hydrogen and hydrogen-rich gases from methane and various fuels using DC arc technology [158]. Hydrogen-rich gas over 40% of the effluent gas was generated in compact plasma reformers. This system has been demonstrated for hydrogen production with low CO content (~1.5%) with power densities of ~30 kW (H_2 HHV)/L of the reactor, or ~ 10 m^3/h H_2 per liter of the reactor.

1.5.3 Liquid Waste Treatment

1.5.3.1 Volatile Organic Compounds

Volatile organic compounds (VOCs) such as acetone, formaldehyde, benzene, toluene, and xylene are harmful to humans and the environment [159]. These are a big group of pollutants. They are rapidly evaporated and enter the atmosphere due to high volatility. On the basis of the molecular structure and concentration, some side effects such as the creation of photochemical smog, secondary aerosols, and tropospheric ozone can be induced [160]. They also influence global warming and the destruction of the ozone layer.

Acetone is a representative VOC used for solvent and paints thinner. However, it exists in the atmosphere with a high concentration brought out from anthropogenic and natural sources. Water plasma was applied to decompose the 5 mol% acetone with an energy yield of 1.7×10^{-7} mol/J [161]. The major products in the effluent gas were H_2 (60–70%), CO_2 (5–16%), CO (6–16%), and CH_4 (0.2–0.9%). The decomposition rate was 99.8% at an arc current of 7 A generating some unwanted products such as HCOOH, HCHO, and soot. They also suggested a detailed decomposition mechanism with three reaction regions.

Liu et al. developed a DC non-transferred arc plasma jet [162]. It has the advantage to be able to produce a plasma jet remotely and inject it into a treated liquid directly. Various phenol concentrations in the range of 50–400 mg/L were treated. With an increase in the specific input energy (SIE), the degradation rate of phenol reached 100% when SIE was over 1,000 kJ/L. OH, H, and O were major reactive species formed by the dissociation of H_2O molecules in the system, and they proposed the degradation mechanism as follows: phenol → catechol and resorcinol → benzoquinone oxalic acid → $CO_2 + H_2O$.

n-hexane (C_6H_{14}) and toluene (C_7H_8) as VOC models were decomposed in RF plasma at an oscillator frequency of 27.17 MHz [163]. The electrical power was in the range of 1.6–2.1 kW with different feed rates. Mixing of O_2 with carrier gas showed a remarkable reduction of soot. On the

other hand, the soot yield increased with an increase of plate power. This is because the higher plate power resulted in higher black carbon, and further the increased surface of the solid carbon could absorb a higher amount of fragments and catalyze processes. Moreover, they found that the two compounds were decomposed through the formation of different aliphatic and aromatic compounds including PAHs.

1.5.3.2 Polychlorinated Biphenyls

Polychlorinated biphenyls (PCBs) are a group of 209 congeners composed of biphenyl with one or more chlorine atoms, and they have been extensively used for insulating and cooling electrical systems such as capacitors and transformers due to low electrical conductivity and high heat resistance [164,165]. Also, due to their strong chemical stability and long-distance migration, the ecological environment is being threatened by PCBs [166]. Furthermore, they are harmful to human health as endocrine [167].

Kim et al. introduced a DC non-transferred steam plasma at 100 kW for PCBs degradation in 2003 [168]. The waste was tangentially injected into a steam plasma flame. The high temperature and free radicals with high reactivity were generated in the reactor. Consequently, the decomposition rate of PCBs in steam plasma was above 99.9999%. However, it was inevitable to suppress the formation of toxic byproducts such as dioxin and furan. According to the results, the steam plasma torch process was more effective for converting hazardous waste to energy than the air plasma torch process.

Biphenyl ($C_{12}H_{10}$) with a similar chemical and molecular structure to PCBs was destructed by a long DC arc torch at different oxygen feeding rates [169]. The arc length of 350 mm was operated under atmospheric pressure at an arc current of 10 A with 30 L/min of Ar. The O_2 feed rates varied from 0 to 2.0 L/min. The result showed that the high decomposition efficiency of

99.83% biphenyl was achieved when sufficient oxygen existed due to enhanced oxidation. The gas byproducts of H_2, CH_4, and CO were detected. The liquid byproducts of benzene, toluene, phenylacetylene, styrene, indene, naphthalene, biphenyl, acenaphthylene, fluorine, phenanthrene, and 4,5-methylenephenanthrene were analyzed. The decomposition mechanism was proposed with the gas and liquid byproducts where C_6H_5 and C_2H_2 were major intermediates in biphenyl pyrolysis.

Westinghouse industrial plasma technology invented plasma pyrolysis reactor in the 1980s and 1990s [114]. The reactor worked with a 1 MW DC non-transferred arc torch, and the air was used as plasma gas. PCBs were destroyed at a rate of up to 720 m^3/h with a torch power of 850 kW. The decomposition rate was 99.999999% with particulate and acid emissions.

1.5.3.3 Pharmaceutical and Personal Care Products

Pharmaceuticals and personal care products (PPCPs) are therapeutic and veterinary drugs, ranging from analgesics and antibiotics to contraceptives and lipid regulators in addition to active ingredients in soaps, detergents, musk, bleaches, dyes, deodorants, shampoos, perfumes, and hair cream, and skin and dental care products [170]. Pharmaceuticals are used primarily to prevent or treat human and animal diseases, whereas personal care products are applied to improve the quality of daily life [171]. However, some PPCPs have been detected in aquatic systems worldwide due to overuse and improper disposal, and it is hard to be removed by the traditional biochemical treatment process for their resistance to biological action [172]. In this section, PPCPs treatments by other methods will mainly be discussed due to few experimental cases using thermal plasmas.

Dielectric barrier discharge (DBD) non-thermal plasma was employed to eliminate bisphenol A (BPA) [173]. BPA is an endocrine-disrupting compound used in the manufacturing of plastics

as well as PPCPs [174]. The OH and O radicals were used for the degradation of BPA by water injection. The result showed that the decomposition rate was increased at both higher discharge voltage and slower water flow rate. At the discharge voltage of 16.8 kV, a complete BPA degradation was achieved within 25 min. The decomposition intermediates of BPA were mainly eight kinds detected, where OH radical was the main reactive oxygen species for the removal of BPA.

Photocatalyst using magnetite-hematite was used for decomposition of acetaminophen which is used for an analgesic and antipyretic drug [175]. Catalytic photodegradation was carried out with 20 mg of the catalyst in 150 mL of 20 ppm acetaminophen, and the radiation source was a 450 W medium-pressure mercury-vapor lamp. The results showed that full degradation of acetaminophen was achieved after approximately 30 min. The liquid chromatography-mass spectrometry (LC-MS) analysis for the acetaminophen degradation solutions showed the presence of the main five species.

Ibuprofen (IBP) used as a nonsteroidal anti-inflammatory drug has been targeted for its resistance to conventional water treatment processes and frequent detection in water systems [176]. UV/chlorine advanced oxidation process (AOP) was applied. The method produces reactive species such as hydroxyl radicals and reactive chlorine species (RCS) like chlorine atoms (·Cl) and $\cdot Cl_2^-$. The experimental concentration of 10 μM IBP with a chlorine concentration of 10–100 μM was decomposed under the low-pressure UV lamp with 10W. A higher concentration of chlorine resulted in a higher decomposition rate of over 90% within 1,200 s. Moreover, the first-order rate constant was 3.3 times higher in this process than that in the UV/H_2O_2 AOP. Also, the contribution of RCS increased from 22 to 30% with an increasing pH from 6 to 9.

1.6 Objective of This Work

Water plasma has received much attention in respect of the waste treatment. The water molecule can provide higher plasma enthalpy and thermal conductivity than those of common plasma gases such as N_2, O_2, and Ar. Therefore, higher heat transfer to the waste material for decomposition is achieved. In particular, high temperature as well as large amount of reactive species such as ·H, ·O, and ·OH are obtained. Finally, the chemical reactions are accelerated by the radicals with production of a large amount of syngas like H_2 and CO, and suppression of byproducts.

Arc characteristics of the water plasma have not, however, been clearly verified despite the importance of the arc characteristics such as arc fluctuation and temperature. Therefore, a fundamental study on the arc characteristics in the water plasma is essential prior to applying to waste treatment.

Pharmaceuticals and personal care products (PPCPs) such as medicines, cosmetics, and detergents have been widely used for the purpose of therapeutic and beauty for both humans and veterinary. They, on the other hand, have raised significant concerns about their potential threats to the water system due to continuous discharge through excretion, bath, and sewage treatment plants. Particularly, *N, N*-diethyl-m-toluamide (DEET) and Caffeine (CAF), commonly adapted as an insect repellent and psychoactive legal drug worldwide, respectively, have been broadly detected in aquatic environments due to their extensive usage. Moreover, they are difficult to be biodegraded for biorefractory, persistence, and bioaccumulation. Thus, an effective treatment technique to decompose PPCPs is inevitable.

The purpose of this dissertation was: (i) to investigate arc fluctuation and temperature of water plasma with mist generation for application to waste treatment; (ii) to decompose DEET and CAF; (iii) to suggest the decomposition mechanism of DEET and CAF.

1.7 Contents of This Work

The flow chart of this dissertation is shown in **Fig. 1.10**. The contents of each chapter in this study are as follows.

In chapter 1, the introduction of thermal plasmas and the objective of this dissertation were presented.

In chapter 2, arc behavior and temperature distribution in water plasma with mist generation were successfully investigated. The effect of mist feeding rate on the arc was observed by high-speed cameras synchronized with an oscilloscope. The arc voltage and length increased due to the higher drag force with an increase of mist feeding rate under constant arc current. The arc fluctuation rapidly increased as the same reason above. Moreover, the fluctuations showed the restrike mode in all experimental conditions, which results from high mist feeding rate and low arc current. Moreover, the area with high temperature also increased due to the increase of the arc voltage and heat convection. Therefore, it was demonstrated that the arc fluctuation and area with a high temperature could be controlled by a flow parameter. On the basis of this results, the water plasma with a mist generation system is expected to play a crucial role in the practical application of waste treatment.

In chapter 3, the effect of arc current (6.0, 7.5, and 9.5 A) on the decomposition of 2,000 ppm DEET was investigated by water plasma. The highest decomposition rate of 94.8% was achieved at an arc current of 9.5 A with an energy yield of 0.3 g/kWh within only 10 min. The contents of H_2 and CO_2 in the effluent gas increased at a higher arc current because of a promoted oxidative environment, and so did the total organic carbon (TOC) reduction rate. The hydroxylated DEET molecule was clearly detected in all experimental conditions. Based on seventeen main intermediates, the decomposition mechanism was suggested in detail, where electronic dissociation attacking weak C–N bond and hydroxylation to the ring structure were predominant

factors at the early stage of decomposition.

In chapter 4, the decomposition of a high concentration of 20 g/L CAF was studied by water plasma according to different arc currents. At torch power of 0.8–1.1 kW, the removal efficiency of TOC and CAF increased with an increase of arc current, reaching 91.1 and 99.8% at 9.5 A, respectively. H_2, CO, CO_2, and N_2 were major effluent gaseous, of which the H_2 generation was more than 40% for all conditions. The nitrogenous compounds were measured as evidence for the reaction pathway of nitrogen and the CAF decomposition mechanism. In particular, the concentration of nitrate (NO_3^-) in the effluent liquids was the highest at 9.5 A, which results from a higher oxidation environment at a higher arc current. The detailed decomposition mechanism was proposed based on eleven intermediate products, in which it was found that electronic dissociation and hydroxylation brought about preliminary decomposition for the ring opening.

In chapter 5, the obtained results and conclusions were summarized and presented. Based on the obtained results through the study of arc characteristics and decomposition mechanism of PPCPs, water plasma is expected to be an alternative green technology for waste treatment. Furthermore, the decomposition of non-soluble organic compounds mixed with surfactant could be suggested for future work.

References

[1] M.I. Boulos, P.L. Fauchais, E. Pfender, Handbook of thermal plasmas, Springer, 2019.
[2] V.S. Sikarwar, M. Hrabovský, G. Van Oost, M. Pohořelý, M. Jeremiáš, Progress in waste utilization via thermal plasma, Progress in Energy and Combustion Science 81 (2020) 100873.
[3] F.F. Chen, Introduction to plasma physics, Springer Science & Business Media, 2012.
[4] M.I. Boulos, P. Fauchais, E. Pfender, Thermal plasmas, Springer Science & Business Media, 1994.
[5] A. Fridman, Plasma chemistry, Cambridge university press, 2008.
[6] P. Fauchais, J.M. Baronnet, State of the art of plasma chemical synthesis of homogenous and heterogenous products, Pure and Applied Chemistry 52(7) (1980) 1669–1705.
[7] M.I. Boulos, Thermal plasma processing, IEEE transactions on Plasma Science 19(6) (1991) 1078–1089.

[8] S. Samal, Thermal plasma technology: The prospective future in material processing, Journal of Cleaner Production 142 (2017) 3131–3150.

[9] M. Shigeta, Modeling and simulation of a turbulent-like thermal plasma jet for nanopowder production, IEEJ Transactions on Electrical and Electronic Engineering 14(1) (2019) 16–28.

[10] P.L. Fauchais, J.V. Heberlein, M.I. Boulos, Thermal spray fundamentals: from powder to part, Springer Science & Business Media 2014.

[11] H. Dinulescu, E. Pfender, Analysis of the anode boundary layer of high intensity arcs, Journal of Applied Physics 51(6) (1980) 3149–3157.

[12] C. Chang, E. Pfender, Nonequilibrium modeling of low-pressure argon plasma jets; Part I: Laminar flow, Plasma chemistry and plasma processing 10(3) (1990) 473–491.

[13] J. Mostaghimi, M.I. Boulos, Thermal plasma sources: how well are they adopted to process needs?, Plasma Chemistry and Plasma Processing 35(3) (2015) 421–436.

[14] X. Chen, Y. Cheng, T. Li, Y. Cheng, Characteristics and applications of plasma assisted chemical processes and reactors, Current Opinion in Chemical Engineering 17 (2017) 68–77.

[15] A.B. Murphy, The effects of metal vapour in arc welding, Journal of Physics D: Applied Physics 43(43) (2010) 434001.

[16] J. Heberlein, Generation of thermal and pseudo-thermal plasmas, Pure and applied chemistry 64(5) (1992) 629–636.

[17] Y. Tanaka, Thermally and chemically non-equilibrium modelling of Ar-N_2-H_2 inductively coupled plasmas at reduced pressure, Thin Solid Films 518(3) (2009) 936–942.

[18] B. Pateyron, M.F. Elchinger, G. Delluc, P. Fauchais, Thermodynamic and transport properties of Ar-H_2 and Ar-He plasma gases used for spraying at atmospheric pressure. I: Properties of the mixtures, Plasma Chemistry and Plasma Processing 12(4) (1992) 421–448.

[19] F.A. Kulacki, S. Acharya, Y. Chudnovsky, R.M. Cotta, R. Devireddy, V.K. Dhir, M.P. Mengüç, J. Mostaghimi, K. Vafai, Handbook of thermal science and engineering, Springer 2018.

[20] A.B. Murphy, M. Tanaka, K. Yamamoto, S. Tashiro, T. Sato, J. Lowke, Modelling of thermal plasmas for arc welding: the role of the shielding gas properties and of metal vapour, Journal of Physics D: Applied Physics 42(19) (2009) 194006.

[21] K. Kim, T. Kim, Nanofabrication by thermal plasma jets: From nanoparticles to low-dimensional nanomaterials, Journal of Applied Physics 125(7) (2019) 070901.

[22] M.G. Shin, D.W. Park, Synthesis of copper nanopowders by transferred arc and non-transferred arc plasma systems, Journal of Optoelectronics and Advanced Materials 12(March 2010) (2009) 528–534.

[23] J. Trelles, C. Chazelas, A. Vardelle, J. Heberlein, Arc plasma torch modeling, Journal of thermal spray technology 18(5) (2009) 728–752.

[24] L. Prevosto, H. Kelly, B. Mancinelli, J. Chamorro, On the gas heating mechanism for the fast

anode arc reattachment in a non-transferred arc plasma torch operating with nitrogen gas in the restrike mode, Plasma Chemistry and Plasma Processing 35(6) (2015) 1057–1070.

[25] E. Gomez, D.A. Rani, C. Cheeseman, D. Deegan, M. Wise, A. Boccaccini, Thermal plasma technology for the treatment of wastes: A critical review, Journal of hazardous materials 161(2-3) (2009) 614–626.

[26] G. Bonizzoni, E. Vassallo, Plasma physics and technology; industrial applications, Vacuum 64(3-4) (2002) 327–336.

[27] F.C.N. Hong, C.J. Yan, Synthesis and characterization of silicon oxide nanoparticles using an atmospheric DC plasma torch, Advanced powder technology 29(2) (2018) 220–229.

[28] D. Harbec, A. Tagnit-Hamou, F. Gitzhofer, Waste-glass fume synthesized using plasma spheroidization technology: reactivity in cement pastes and mortars, Construction and Building Materials 107 (2016) 272–286.

[29] L. Fulcheri, Y. Schwob, F. Fabry, G. Flamant, L. Chibante, D. Laplaze, Fullerene production in a 3-phase AC plasma process, Carbon 38(6) (2000) 797–803.

[30] D. Gold, C. Bonet, G. Chauvin, A. Mathieu, G. Geirnaert, J. Millet, A 100-kW three-phase AC plasma furnace for spheroidization of aluminum silicate particles, Plasma Chemistry and Plasma Processing 1(2) (1981) 161–178.

[31] Y. Yao, K. Yatsuda, T. Watanabe, T. Matsuura, T. Yano, Characteristics of multi-phase alternating current arc for glass in-flight melting, Plasma Chemistry and Plasma Processing 29(5) (2009) 333–346.

[32] T. Okuma, H. Maruyama, T. Hashizume, M. Tanaka, T. Watanabe, H. Nagai, T. Koiwasaki, H. Nasu, Effects of the driving frequency on temperature in a multiphase AC arc, IEEE Transactions on Plasma Science 47(1) (2018) 32–38.

[33] T. Watanabe, K. Yatsuda, Y. Yao, T. Yano, T. Matuura, Innovative in-flight glass-melting technology using thermal plasmas, Pure and Applied Chemistry 82(6) (2010) 1337–1351.

[34] T. Matsuura, K. Taniguchi, T. Watanabe, A new type of arc plasma reactor with 12-phase alternating current discharge for synthesis of carbon nanotubes, Thin Solid Films 515(9) (2007) 4240–4246.

[35] Y. Liu, M. Tanaka, S. Choi, T. Watanabe, Investigation of In-Flight Glass Melting by Controlling the High-Temperature Region of Multiphase AC Arc Plasma, International Journal of Applied Glass Science 5(4) (2014) 443–451.

[36] M. Tanaka, Y. Tsuruoka, Y. Liu, T. Matsuura, T. Watanabe, Stability analysis of multi-phase AC arc discharge for in-flight glass melting, Current Applied Physics 11(5) (2011) S35–S39.

[37] E. Bouyer, F. Gitzhofer, M.I. Boulos, Suspension plasma spraying for hydroxyapatite powder preparation by RF plasma, IEEE transactions on plasma science 25(5) (1997) 1066–1072.

[38] A. Indarto, J.W. Choi, H. Lee, H.K. Song, Decomposition of greenhouse gases by plasma,

Environmental Chemistry Letters 6(4) (2008) 215–222.

[39] M. Shih, W.J. Lee, C.H. Tsai, P.J. Tsai, C.Y. Chen, Decomposition of SF6 in an RF plasma environment, Journal of the Air & Waste Management Association 52(11) (2002) 1274–1280.

[40] X. Zhang, Z. Liu, M. Tanaka, T. Watanabe, Formation mechanism of amorphous silicon nanoparticles with additional counter-flow quenching gas by induction thermal plasma, Chemical Engineering Science 230 (2021) 116217.

[41] M. Shigeta, T. Watanabe, Two-dimensional analysis of nanoparticle formation in induction thermal plasmas with counterflow cooling, Thin Solid Films 516(13) (2008) 4415–4422.

[42] H. Sekiguchi, T. Orimo, Gasification of polyethylene using steam plasma generated by microwave discharge, Thin Solid Films 457(1) (2004) 44–47.

[43] M. Singh, A. Sengupta, K. Zeller, G. Skoptsov, R.L. Vander Wal, Effect of hydrogen concentration on graphene synthesis using microwave-driven plasma-mediated methane cracking, Carbon 143 (2019) 802–813.

[44] S. Vecten, M. Wilkinson, N. Bimbo, R. Dawson, B. Herbert, Experimental investigation of the temperature distribution in a microwave-induced plasma reactor, Fuel Processing Technology 212 (2021) 106631.

[45] C. Zhao, L. Xue, Y. Zhou, Y. Zhang, K. Huang, A microwave atmospheric plasma strategy for fast and efficient degradation of aqueous p-nitrophenol, Journal of Hazardous Materials 409 (2021) 124473.

[46] J.F. de la Fuente, A.A. Kiss, M.T. Radoiu, G.D. Stefanidis, Microwave plasma emerging technologies for chemical processes, Journal of Chemical Technology & Biotechnology 92(10) (2017) 2495–2505.

[47] D.S. Stepanov, A. Chebotarev, E.Y. Shkol'nikov, Analysis of the Operation of the Microwave Ion Source in the Electron–Cyclotron Resonance Mode for a Portable Neutron Generator, High Temperature 57(3) (2019) 316–321.

[48] N. Bundaleska, D. Tsyganov, A. Dias, E. Felizardo, J. Henriques, F. Dias, M. Abrashev, J. Kissovski, E. Tatarova, Microwave plasma enabled synthesis of free standing carbon nanostructures at atmospheric pressure conditions, Physical Chemistry Chemical Physics 20(20) (2018) 13810–13824.

[49] R. Tucker, ASM handbook, volume 5A: thermal spray technology, ASM International 57 (2013).

[50] Z. Salhi, D. Klein, P. Gougeon, C. Coddet, Development of coating by thermal plasma spraying under very low-pressure condition< 1 mbar, Vacuum 77(2) (2005) 145–150.

[51] J.E. Döring, R. Vaßen, G. Pintsuk, D. Stöver, The processing of vacuum plasma-sprayed tungsten-copper composite coatings for high heat flux components, Fusion engineering and design 66 (2003) 259–263.

[52] D. Varacalle Jr, L. Lundberg, H. Herman, G. Bancke, Titanium carbide coatings fabricated by the vacuum plasma spraying process, Surface and Coatings Technology 86 (1996) 70–74.

[53] M. Boulos, RF induction plasma spraying: State-of-the-art review, Journal of thermal spray technology 1(1) (1992) 33–40.

[54] M.I. Boulos, New frontiers in thermal plasma processing, Pure and applied chemistry 68(5) (1996) 1007–1010.

[55] W. Lucas, TIG and plasma welding: process techniques, recommended practices and applications, Woodhead Publishing1990.

[56] J. Wilden, J. Bergmann, H. Frank, Plasma transferred arc welding-modeling and experimental optimization, Journal of Thermal Spray Technology 15(4) (2006) 779–784.

[57] D. Krajcarz, Comparison metal water jet cutting with laser and plasma cutting, Procedia Engineering 69 (2014) 838–843.

[58] R. O'BRIEN, Welding processes, Welding handbook 2 1991.

[59] V.A. Nemchinsky, W. Severance, What we know and what we do not know about plasma arc cutting, Journal of physics d: applied physics 39(22) (2006) R423.

[60] Q. Zhou, H. Li, F. Liu, S. Guo, W. Guo, P. Xu, Effects of nozzle length and process parameters on highly constricted oxygen plasma cutting arc, Plasma Chemistry and Plasma Processing 28(6) (2008) 729–747.

[61] S. Samal, D.W. Park, Nano-particle synthesis of titanium oxides from ilmenite in a thermal plasma reactor, Chemical Engineering Research and Design 90(4) (2012) 548–554.

[62] M. Benmansour, M. Nikravech, D. Morvan, J. Amouroux, J. Chapelle, Diagnostic by emission spectroscopy of an argon–hydrogen RF inductive thermal plasma for purification of metallurgical grade silicon, Journal of Physics D: Applied Physics 37(21) (2004) 2966.

[63] R.W. Siegel, Synthesis and properties of nanophase materials, Materials Science and Engineering: A 168(2) (1993) 189–197.

[64] M. Shigeta, A.B. Murphy, Thermal plasmas for nanofabrication, Journal of Physics D: Applied Physics 44(17) (2011) 174025.

[65] E.H. Ko, T.H. Kim, S. Choi, D.W. Park, Synthesis of Cubic Boron Nitride Nanoparticles from Boron Oxide, Melamine and NH_3 by Non-Transferred Ar-N_2 Thermal Plasma, Journal of Nanoscience and Nanotechnology 15(11) (2015) 8515–8520.

[66] T. Yoshida, A. Kawasaki, K. Nakagawa, K. Akashi, The synthesis of ultrafine titanium nitride in an rf plasma, Journal of Materials Science 14(7) (1979) 1624–1630.

[67] D. Thompson, M. Leparoux, C. Jaeggi, J. Buha, D.Y. Pui, J. Wang, Aerosol emission monitoring in the production of silicon carbide nanoparticles by induction plasma synthesis, Journal of nanoparticle research 15(12) (2013) 1–13.

[68] M. Tanaka, T. Kageyama, H. Sone, S. Yoshida, D. Okamoto, T. Watanabe, Synthesis of lithium

metal oxide nanoparticles by induction thermal plasmas, Nanomaterials 6(4) (2016) 60.

[69] H. Sone, T. Kageyama, M. Tanaka, D. Okamoto, T. Watanabe, Induction thermal plasma synthesis of lithium oxide composite nanoparticles with a spinel structure, Japanese Journal of Applied Physics 55(7S2) (2016) 07LE04.

[70] M. Benilov, M. Cunha, Heating of refractory cathodes by high-pressure arc plasmas: I, Journal of Physics D: Applied Physics 35(14) (2002) 1736.

[71] S. Coulombe, A model for the arc attachment on the cathode of high intensity discharge (HID) lamps, General Electric report, 1998.

[72] X. Zhou, B. Ding, J.V. Heberlein, Temperature measurement and metallurgical study of cathodes in DC arcs, IEEE Transactions on Components, Packaging, and Manufacturing Technology: Part A 19(3) (1996) 320–328.

[73] E.L. Murphy, R. Good Jr, Thermionic emission, field emission, and the transition region, Physical review 102(6) (1956) 1464.

[74] M.S. Benilov, L.G. Benilova, Physics of spotless mode of current transfer to cathodes of metal vapor arcs, IEEE Transactions on Plasma Science 43(8) (2015) 2247–2252.

[75] K. Hsu, K. Etemadi, E. Pfender, Study of the free-burning high-intensity argon arc, Journal of applied physics 54(3) (1983) 1293–1301.

[76] B. Djakov, R. Holmes, Cathode spot structure and dynamics in low-current vacuum arcs, Journal of Physics D: Applied Physics 7(4) (1974) 569.

[77] V. Nemchinsky, Erosion of thermionic cathodes in welding and plasma arc cutting systems, IEEE Transactions on Plasma Science 42(1) (2013) 199–215.

[78] V. Nemchinsky, Cathode erosion rate in high-pressure arcs: influence of swirling gas flow, IEEE transactions on plasma science 30(6) (2002) 2113–2116.

[79] M. Benilov, A. Marotta, A model of the cathode region of atmospheric pressure arcs, Journal of Physics D: Applied Physics 28(9) (1995) 1869.

[80] S. Lichtenberg, D. Nandelstädt, L. Dabringhausen, M. Redwitz, J. Luhmann, J. Mentel, Observation of different modes of cathodic arc attachment to HID electrodes in a model lamp, Journal of Physics D: Applied Physics 35(14) (2002) 1648.

[81] N. Sanders, E. Pfender, Measurement of anode falls and anode heat transfer in atmospheric pressure high intensity arcs, Journal of Applied Physics 55(3) (1984) 714–722.

[82] M.F. Zhukov, I. Zasypkin, Thermal plasma torches: design, characteristics, application, Cambridge Int Science Publishing 2007.

[83] J. Heberlein, J. Gorman, The high current metal vapor arc column between separating electrodes, IEEE Transactions on plasma science 8(4) (1980) 283–288.

[84] N. Sanders, K. Etemadi, K. Hsu, E. Pfender, Studies of the anode region of a high-intensity argon arc, Journal of Applied Physics 53(6) (1982) 4136–4145.

[85] M. Tanaka, M. Ushio, Observations of the anode boundary layer in free-burning argon arcs, Journal of Physics D: Applied Physics 32(8) (1999) 906.

[86] E. Pfender, Electric arcs and arc gas heaters, Gaseous electronics 1(5) (1978) 291–298.

[87] R.M. Hartmann, J.V. Heberlein, Quantitative investigations on arc-anode attachments in transferred arcs, Journal of Physics D: Applied Physics 34(19) (2001) 2972.

[88] E. Pfender, Thermal plasma technology: Where do we stand and where are we going?, Plasma chemistry and plasma processing 19(1) (1999) 1–31.

[89] J. Trelles, J. Heberlein, Simulation results of arc behavior in different plasma spray torches, Journal of Thermal Spray Technology 15(4) (2006) 563–569.

[90] J.P. Trelles, Computational study of flow dynamics from a dc arc plasma jet, Journal of Physics D: Applied Physics 46(25) (2013) 255201.

[91] W. Pan, Z. Guo, X. Meng, H. Huang, C. Wu, Fluctuation characteristics of arc voltage and jet flow in a non-transferred dc plasma generated at reduced pressure, Plasma Sources Science and Technology 18(4) (2009) 045032.

[92] F. Mavier, V. Rat, J.F. Coudert, Influence of time-modulation of applied current on arc stability in DC pulsed plasma spray torch, IEEE Transactions on Plasma Science 45(4) (2016) 565–573.

[93] M. Shigeta, Simulating turbulent thermal plasma flows for nanopowder fabrication, Plasma Chemistry and Plasma Processing 40(3) (2020) 775–794.

[94] S. Wutzke, E. Pfender, E. Eckert, Study of electric arc behavior with superimposed flow, AIAA journal 5(4) (1967) 707–713.

[95] S. Wutzke, E. Pfender, E. Ecker, Symptomatic behavior of an electric arc with a superimposed flow, Aiaa Journal 6(8) (1968) 1474–1482.

[96] J. Trelles, E. Pfender, J. Heberlein, Modelling of the arc reattachment process in plasma torches, Journal of Physics D: Applied Physics 40(18) (2007) 5635.

[97] Z. Duan, J. Heberlein, Arc instabilities in a plasma spray torch, Journal of Thermal Spray Technology 11(1) (2002) 44–51.

[98] M. Shigeta, T. Watanabe, Growth mechanism of silicon-based functional nanoparticles fabricated by inductively coupled thermal plasmas, Journal of Physics D: Applied Physics 40(8) (2007) 2407.

[99] T. Ryu, H. Sohn, K.S. Hwang, Z.Z. Fang, Chemical vapor synthesis (CVS) of tungsten nanopowder in a thermal plasma reactor, International Journal of Refractory Metals and Hard Materials 27(1) (2009) 149–154.

[100] E. Pfender, Y. Lee, Particle dynamics and particle heat and mass transfer in thermal plasmas. Part I. The motion of a single particle without thermal effects, Plasma Chemistry and Plasma Processing 5(3) (1985) 211–237.

[101] O. Hurba, M. Hlìna, M. Hrabovský, Diagnostics of Plasma Jet Generated in Water/Argon DC Arc Torch, Plasma Physics and Technology 3(1) (2016) 5–8.

[102] E. Leveroni, E. Pfender, Electric probe diagnostics in thermal plasmas: Double probe theory and experimental results, Review of scientific instruments 60(12) (1989) 3744–3749.

[103] C. Fanara, L. Vilarinho, Electrical characterization of atmospheric pressure arc plasmas, The European Physical Journal D-Atomic, Molecular, Optical and Plasma Physics 28(2) (2004) 241–251.

[104] M. Brossa, E. Pfender, Probe measurements in thermal plasma jets, Plasma Chemistry and Plasma Processing 8(1) (1988) 75–90.

[105] H.R. Griem, Principles of plasma spectroscopy, 2005.

[106] W. Chen, J. Heberlein, E. Pfender, Diagnostics of a thermal plasma jet by optical emission spectroscopy and enthalpy probe measurements, Plasma Chemistry and Plasma Processing 14(3) (1994) 317–332.

[107] L.O. Vilarinho, A. Scotti, Proposal for a modified Fowler-Milne method to determine the temperature profile in TIG welding at low currents, Journal of the Brazilian Society of Mechanical Sciences and Engineering 26(1) (2004) 34–39.

[108] A. Murphy, Modified Fowler-Milne method for the spectroscopic measurement of temperature and composition of multielement thermal plasmas, Review of scientific instruments 65(11) (1994) 3423–3427.

[109] J. Peters, B. Bartlett, J. Lindsay, J. Heberlein, Relating spectroscopic measurements in a plasma cutting torch to cutting performance, Plasma Chemistry and Plasma Processing 28(3) (2008) 331–352.

[110] J. Peters, J. Heberlein, J. Lindsay, Spectroscopic diagnostics in a highly constricted oxygen arc, Journal of Physics D: Applied Physics 40(13) (2007) 3960.

[111] B. Bachmann, R. Kozakov, G. Gött, K. Ekkert, J.P. Bachmann, J. Marques, H. Schöpp, D. Uhrlandt, J. Schein, High-speed three-dimensional plasma temperature determination of axially symmetric free-burning arcs, Journal of Physics D: Applied Physics 46(12) (2013) 125203.

[112] T. Okuma, H. Maruyama, T. Imatsuji, T. Hashizume, H. Nagai, T. Koiwasaki, M. Tanaka, T. Watanabe, Investigation of Arc Behavior and Temperature Distribution Corresponding to Electrode and Phase Configurations in a Multiphase AC Arc, Journal of Chemical Engineering of Japan 53(9) (2020) 509–515.

[113] S. Safa, G. Soucy, Liquid and solution treatment by thermal plasma: a review, International journal of environmental science and technology 11(4) (2014) 1165–1188.

[114] A. Murphy, Plasma destruction of gaseous and liquid wastes, Annals of the New York Academy of Sciences 891(1) (1999) 106–123.

[115] J. Heberlein, A.B. Murphy, Thermal plasma waste treatment, Journal of Physics D: Applied Physics 41(5) (2008) 053001.

[116] B. Ruj, S. Ghosh, Technological aspects for thermal plasma treatment of municipal solid waste—A review, Fuel Processing Technology 126 (2014) 298–308.

[117] D. Hoornweg, P. Bhada-Tata, What a waste: a global review of solid waste management, (2012).

[118] Y. Byun, W. Namkung, M. Cho, J.W. Chung, Y.S. Kim, J.H. Lee, C.R. Lee, S.M. Hwang, Demonstration of thermal plasma gasification/vitrification for municipal solid waste treatment, Environmental science & technology 44(17) (2010) 6680–6684.

[119] Y. Byun, M. Cho, S.M. Hwang, J. Chung, Thermal plasma gasification of municipal solid waste (MSW), Gasification for Practical Applications 1 (2012) 183–210.

[120] R. Bie, S. Li, H. Wang, Characterization of PCDD/Fs and heavy metals from MSW incineration plant in Harbin, Waste Management 27(12) (2007) 1860–1869.

[121] Q. Zhang, L. Dor, D. Fenigshtein, W. Yang, W. Blasiak, Gasification of municipal solid waste in the Plasma Gasification Melting process, Applied Energy 90(1) (2012) 106–112.

[122] K. Katou, T. Asou, Y. Kurauchi, R. Sameshima, Melting municipal solid waste incineration residue by plasma melting furnace with a graphite electrode, Thin solid films 386(2) (2001) 183–188.

[123] G. Van Oost, M. Hrabovsky, V. Kopecky, M. Konrad, M. Hlina, T. Kavka, Pyrolysis/gasification of biomass for synthetic fuel production using a hybrid gas-water stabilized plasma torch, Vacuum 83(1) (2008) 209–212.

[124] J.E. Hall, Recent developments in sludge disposal and use, Cemistry and Chem Ind 6 (1993) 188–191.

[125] J. Balgaranova, Plasma chemical gasification of sewage sludge, Waste management & research 21(1) (2003) 38–41.

[126] A. Mountouris, E. Voutsas, D. Tassios, Plasma gasification of sewage sludge: Process development and energy optimization, Energy conversion and management 49(8) (2008) 2264–2271.

[127] W. Kordylewski, J. Michalski, M. Ociepa, M. Wnukowski, A microwave plasma potential in producer gas cleaning-preliminary results with a gas derived from a sewage sludge, Transactions of the Institute of Fluid-Flow Machinery (2017).

[128] X. Cai, C. Du, Thermal plasma treatment of medical waste, Plasma Chemistry and Plasma Processing 41(1) (2021) 1–46.

[129] Z.M. Shareefdeen, Medical waste management and control, Journal of Environmental Protection 3(12) (2012) 1625.

[130] J. Fiedler, E. Lietz, D. Bendix, D. Hebecker, Experimental and numerical investigations of

a plasma reactor for the thermal destruction of medical waste using a model substance, Journal of Physics D: Applied Physics 37(7) (2004) 1031.

[131] P. Colombo, G. Brusatin, E. Bernardo, G. Scarinci, Inertization and reuse of waste materials by vitrification and fabrication of glass-based products, Current Opinion in Solid State and Materials Science 7(3) (2003) 225–239.

[132] C. Ferreira, A. Ribeiro, L. Ottosen, Possible applications for municipal solid waste fly ash, Journal of hazardous materials 96(2-3) (2003) 201–216.

[133] J. Chu, I. Hwang, C. Tzeng, Y. Kuo, Y. Yu, Characterization of vitrified slag from mixed medical waste surrogates treated by a thermal plasma system, Journal of Hazardous Materials 58(1-3) (1998) 179–194.

[134] K. Koike, T. Fukuda, S. Fujikawa, M. Saeda, Study of CF_4, C_2F_6, SF_6 and NF_3 decomposition characteristics and etching performance in plasma state, Japanese journal of applied physics 36(9R) (1997) 5724.

[135] A. Ravishankara, S. Solomon, A.A. Turnipseed, R. Warren, Atmospheric lifetimes of long-lived halogenated species, Science 259(5092) (1993) 194–199.

[136] F. Breitbarth, D. Berg, K. Dumke, H.J. Tiller, Investigation of the low-pressure plasma-chemical conversion of fluorocarbon waste gases, Plasma chemistry and plasma processing 17(1) (1997) 39–57.

[137] K. Protocol, Climate Change Conference, Kyoto, Japan, Dec (1997) 1–10.

[138] J.W. Sun, D.W. Park, CF_4 decomposition by thermal plasma processing, Korean Journal of Chemical Engineering 20(3) (2003) 476–481.

[139] J.H. Ko, S. Choi, H.W. Park, D.W. Park, Decomposition of nitrogen trifluoride using low power arc plasma, Plasma Science and Technology 15(9) (2013) 923.

[140] Y.C. Hong, H.S. Uhm, B.J. Chun, S.K. Lee, S.K. Hwang, D.S. Kim, Microwave plasma torch abatement of NF_3 and SF_6, Physics of plasmas 13(3) (2006) 033508.

[141] G. Restrepo, M. Weckert, R. Brüggemann, S. Gerstmann, H. Frank, Ranking of refrigerants, Environmental science & technology 42(8) (2008) 2925–2930.

[142] S.K. Kundu, E.M. Kennedy, J.C. Mackie, C.I. Holdsworth, T.S. Molloy, V.V. Gaikwad, B.Z. Dlugogorski, Effect of methane on the conversion of HFC-134a in a dielectric barrier discharge non-equilibrium plasma reactor, Chemical Engineering Journal 284 (2016) 412–421.

[143] M. Jasiński, M. Dors, J. Mizeraczyk, Destruction of Freon HFC-134a using a nozzleless microwave plasma source, Plasma Chemistry and Plasma Processing 29(5) (2009) 363–372.

[144] T. Watanabe, T. Tsuru, Water plasma generation under atmospheric pressure for HFC destruction, Thin Solid Films 516(13) (2008) 4391–4396.

[145] G. Angelino, C. Invernizzi, Experimental investigation on the thermal stability of some new zero ODP refrigerants, International Journal of Refrigeration 26(1) (2003) 51–58.

[146] A. McCulloch, A. Lindley, Global emissions of HFC-23 estimated to year 2015, Atmospheric Environment 41(7) (2007) 1560–1566.

[147] W. Han, E.M. Kennedy, S.K. Kundu, J.C. Mackie, A.A. Adesina, B.Z. Dlugogorski, Experimental and chemical kinetic study of the pyrolysis of trifluoroethane and the reaction of trifluoromethane with methane, Journal of Fluorine Chemistry 131(7) (2010) 751–760.

[148] S. Choi, K.Y. Cho, J.M. Woo, J.C. Lim, J.K. Lee, Numerical analysis on a thermal plasma reactor for HFC-23 treatment, Current Applied Physics 11(5) (2011) S94–S98.

[149] M. Jasiński, P. Szczucki, M. Dors, J. Mizeraczyk, M. Lubański, Z. Zakrzewski, Decomposition of fluorohydrocarbons in atmospheric-pressure flowing air using coaxial-line-based microwave torch plasma, Czechoslovak Journal of Physics 50(3) (2000) 285–288.

[150] J. Skalny, V. Sobek, P. Lukac, Negative Corona Induced Decomposition of CClF, NATO ASI SERIES GECOLOGICAL SCIENCES 34 (1993) 151–156.

[151] T. Oda, T. Takahashi, R. Yamashita, Non-thermal plasma processing for VOCs decomposition and NOx removal in flue gas, Journal of Advanced Oxidation Technologies 2(2) (1997) 337–345.

[152] K.A. Főglein, J. Szépvölgyi, P.T. Szabó, E. Mészáros, E. Pekker-Jakab, I.Z. Babievskaya, I. Mohai, Z. Károly, Comparative study on decomposition of $CFCl_3$ in thermal and cold plasma, Plasma chemistry and plasma processing 25(3) (2005) 275–288.

[153] H. Sekiguchi, T. Honda, A. Kanzawa, Thermal plasma decomposition of chlorofluorocarbons, Plasma chemistry and plasma processing 13(3) (1993) 463–478.

[154] S.A. Montzka, E.J. Dlugokencky, J.H. Butler, Non-CO_2 greenhouse gases and climate change, Nature 476(7358) (2011) 43–50.

[155] G.J. Velders, D.W. Fahey, J.S. Daniel, M. McFarland, S.O. Andersen, The large contribution of projected HFC emissions to future climate forcing, Proceedings of the National Academy of Sciences 106(27) (2009) 10949–10954.

[156] D.P. van Vuuren, J. Weyant, F. de la Chesnaye, Multi-gas scenarios to stabilize radiative forcing, Energy Economics 28(1) (2006) 102–120.

[157] A. Mašláni, M. Hrabovský, P. Křenek, M. Hlina, S. Raman, V.S. Sikarwar, M. Jeremiáš, Pyrolysis of methane via thermal steam plasma for the production of hydrogen and carbon black, International Journal of Hydrogen Energy 46(2) (2021) 1605–1614.

[158] L. Bromberg, D. Cohn, A. Rabinovich, N. Alexeev, Plasma catalytic reforming of methane, International Journal of Hydrogen Energy 24(12) (1999) 1131–1137.

[159] A.M. Vandenbroucke, R. Morent, N. De Geyter, C. Leys, Non-thermal plasmas for non-

catalytic and catalytic VOC abatement, Journal of hazardous materials 195 (2011) 30-54.

[160] J.R. Odum, T. Jungkamp, R.J. Griffin, H. Forstner, R.C. Flagan, J.H. Seinfeld, Aromatics, reformulated gasoline, and atmospheric organic aerosol formation, Environmental Science & Technology 31(7) (1997) 1890–1897.

[161] T. Watanabe, Acetone decomposition by water plasmas at atmospheric pressure, Chemical engineering science 69(1) (2012) 296–303.

[162] J.L. Liu, H.W. Park, A. Hamdan, M.S. Cha, In-liquid arc plasma jet and its application to phenol degradation, Journal of Physics D: Applied Physics 51(11) (2018) 114005.

[163] K.A. Föglein, I. Babievskaya, P.T. Szabó, J. Szépvölygi, Recent studies on the decomposition of n-hexane and toluene in RF thermal plasma, Plasma chemistry and plasma processing 23(2) (2003) 233–243.

[164] G. Pompa, F. Caloni, M. Fracchiolla, Dioxin and PCB contamination of fish and shellfish: assessment of human exposure. Review of the international situation, Veterinary Research Communications 27(1) (2003) 159–167.

[165] K.N. Dimou, T.L. Su, R.I. Hires, R. Miskewitz, Distribution of polychlorinated biphenyls in the Newark Bay Estuary, Journal of hazardous materials 136(1) (2006) 103–110.

[166] Q. Huang, C. Fang, Degradation of 3, 3′, 4, 4′-tetrachlorobiphenyl (PCB77) by dielectric barrier discharge (DBD) non-thermal plasma: degradation mechanism and toxicity evaluation, Science of The Total Environment 739 (2020) 139926.

[167] E. Diamanti-Kandarakis, J.P. Bourguignon, L.C. Giudice, R. Hauser, G.S. Prins, A.M. Soto, R.T. Zoeller, A.C. Gore, Endocrine-disrupting chemicals: an Endocrine Society scientific statement, Endocrine reviews 30(4) (2009) 293–342.

[168] S.W. Kim, H.S. Park, H.J. Kim, 100 kW steam plasma process for treatment of PCBs (polychlorinated biphenyls) waste, Vacuum 70(1) (2003) 59–66.

[169] T. Li, T. Watanabe, K. Ochi, K. Otsuki, Liquid waste decomposition by long DC arc under atmospheric pressure, Chemical engineering journal 231 (2013) 155–162.

[170] P.H. Roberts, K.V. Thomas, The occurrence of selected pharmaceuticals in wastewater effluent and surface waters of the lower Tyne catchment, Science of the Total Environment 356(1-3) (2006) 143–153.

[171] A.B. Boxall, M.A. Rudd, B.W. Brooks, D.J. Caldwell, K. Choi, S. Hickmann, E. Innes, K. Ostapyk, J.P. Staveley, T. Verslycke, Pharmaceuticals and personal care products in the environment: what are the big questions?, Environmental health perspectives 120(9) (2012) 1221–1229.

[172] K.S. Kim, C.S. Yang, Y. Mok, Degradation of veterinary antibiotics by dielectric barrier discharge plasma, Chemical engineering journal 219 (2013) 19–27.

[173] J. Yang, D. Zeng, M. Hassan, Z. Ma, L. Dong, Y. Xie, Y. He, Efficient degradation of

Bisphenol A by dielectric barrier discharge non-thermal plasma: Performance, degradation pathways and mechanistic consideration, Chemosphere 286 (2022) 131627.

[174] Y. Lv, S. Lu, Y. Dai, C. Rui, Y. Wang, Y. Zhou, Y. Li, Q. Pang, R. Fan, Higher dermal exposure of cashiers to BPA and its association with DNA oxidative damage, Environment international 98 (2017) 69–74.

[175] T.A. Fernandes, S.G. Mendo, L.P. Ferreira, N.R. Neng, M.C. Oliveira, A. Gil, M.D. Carvalho, O.C. Monteiro, J.M. Nogueira, M.J. Calhorda, Photocatalytic degradation of acetaminophen and caffeine using magnetite–hematite combined nanoparticles: kinetics and mechanisms, Environmental Science and Pollution Research 28(14) (2021) 17228–17243.

[176] G. Ruggeri, G. Ghigo, V. Maurino, C. Minero, D. Vione, Photochemical transformation of ibuprofen into harmful 4-isobutylacetophenone: pathways, kinetics, and significance for surface waters, Water research 47(16) (2013) 6109–6121.

Table 1.1. Summary for characteristics of thermal plasma and non-thermal plasma [7,14].

Plasma type	Pressure	Temperature (T)	Electron density (n_e)	Application
Thermal plasma	> 10 kPa	$T_h \fallingdotseq T_e \sim 10^4$ K (Equilibrium)	10^{21}–10^{26} m^{-3}	Material Processing Waste treatment Cutting and Welding
Non-thermal plasma	< 10 kPa	$T_h \ll T_e \sim 10^{4–5}$ K (Non-equilibrium)	< 10^{19} m^{-3}	Air Pollution Control Surface Treatment Etching and coating

Table 1.2. Ionization and dissociation energies for the various plasma gases [10].

Species	Ar	He	H	N	O	H_2	N_2	O_2
Ionization energy (eV)	15.755	24.481	13.659	14.534	13.614	15.426	15.58	12.06
Dissociation Energy (eV)	-	-	-	-	-	4.588	9.756	5.08

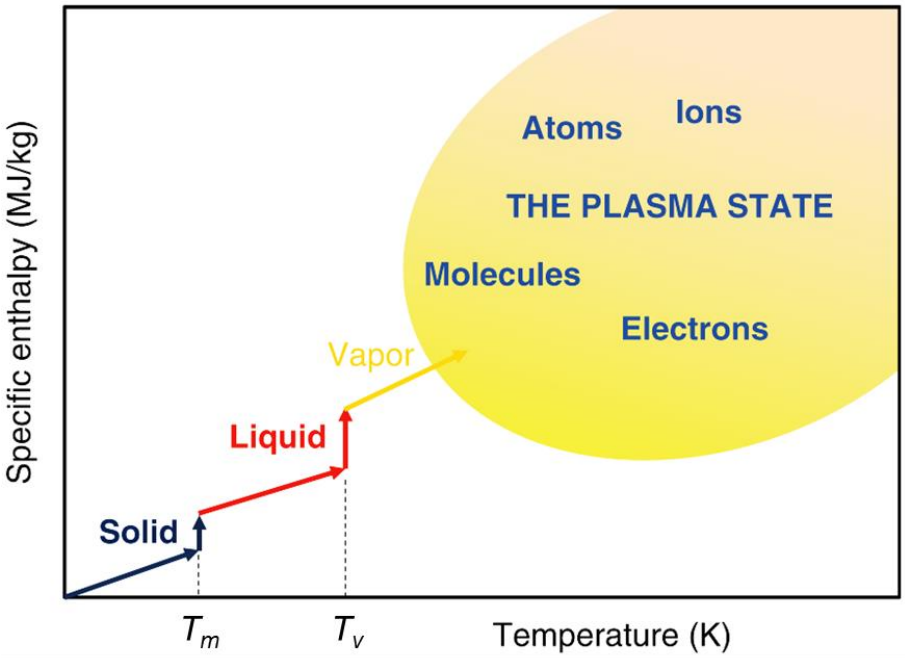

Fig. 1.1. Four states of matter with respect to the temperature [1].

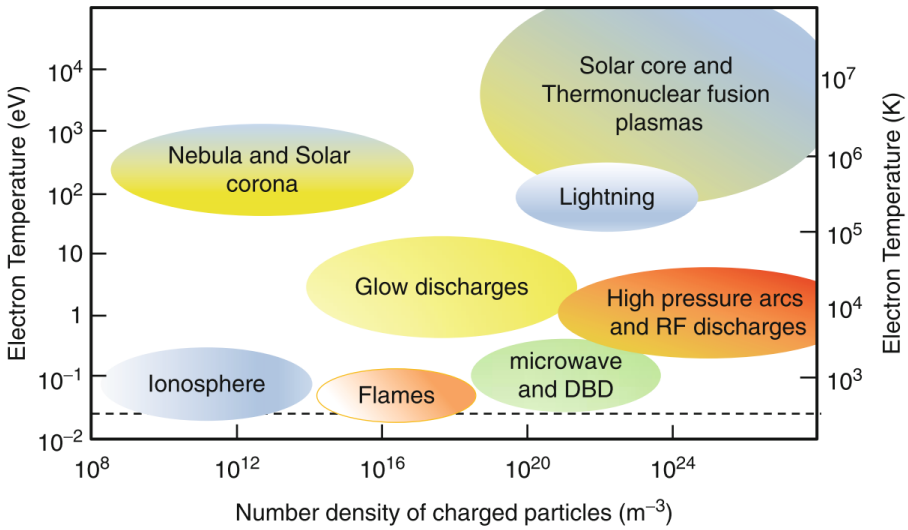

Fig. 1.2. Categories of plasmas [1].

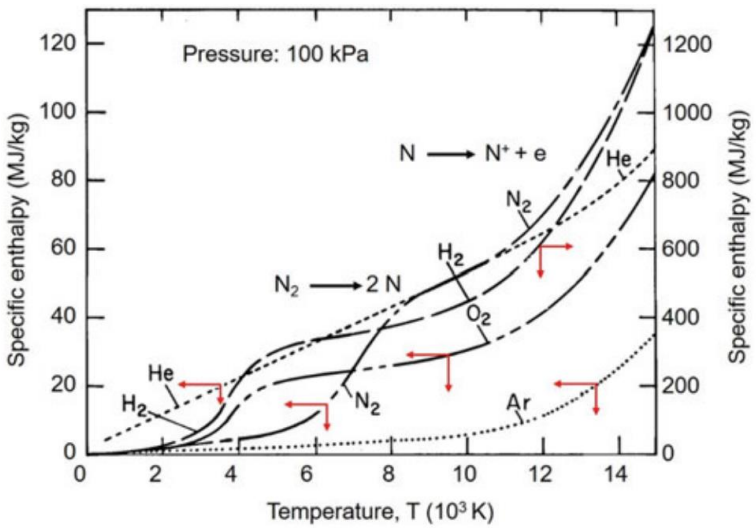

Fig. 1.3. Specific enthalpy of Ar, He, N_2, H_2, and O_2 according to temperature [10].

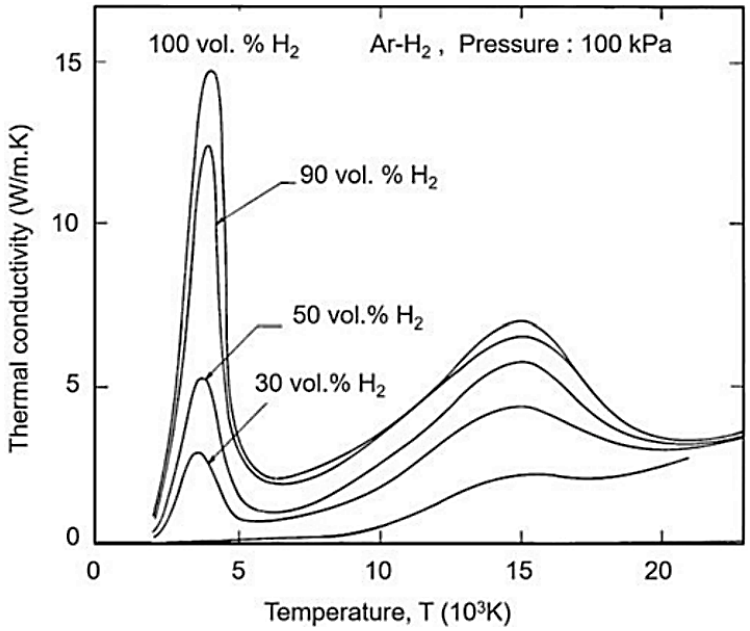

Fig. 1.4. Thermal conductivity of Ar-H_2 mixture with respect to the temperature [10].

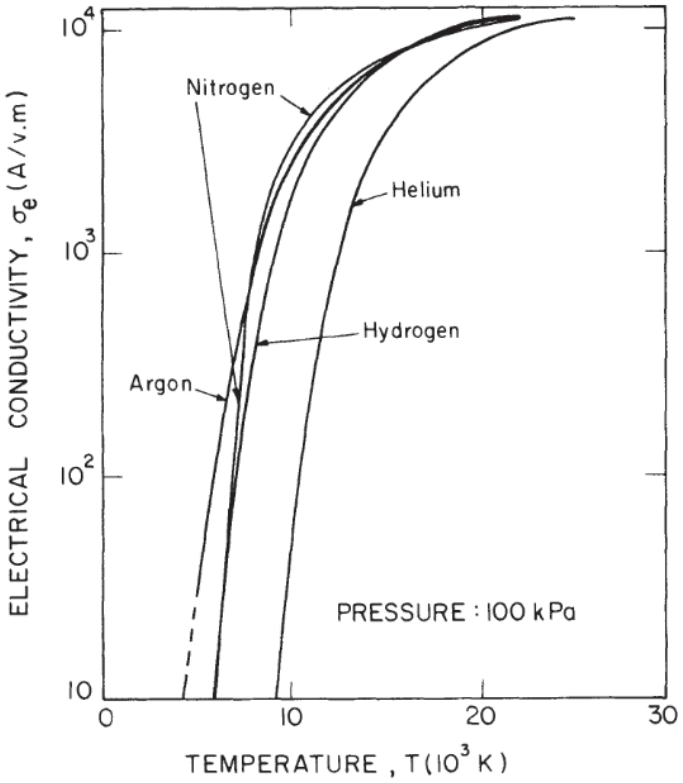

Fig. 1.5. Electrical conductivity of various plasma gases as a function of temperature [4].

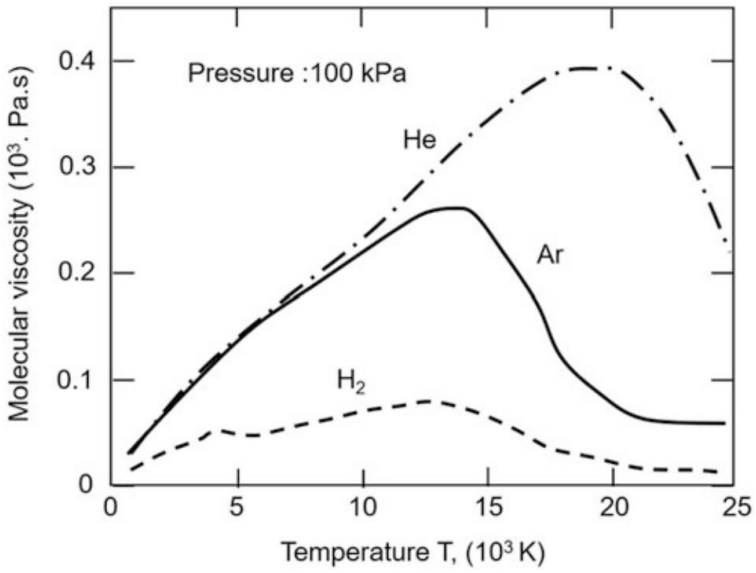

Fig. 1.6. Molecular viscosity of various plasma gases as a function of temperature [10].

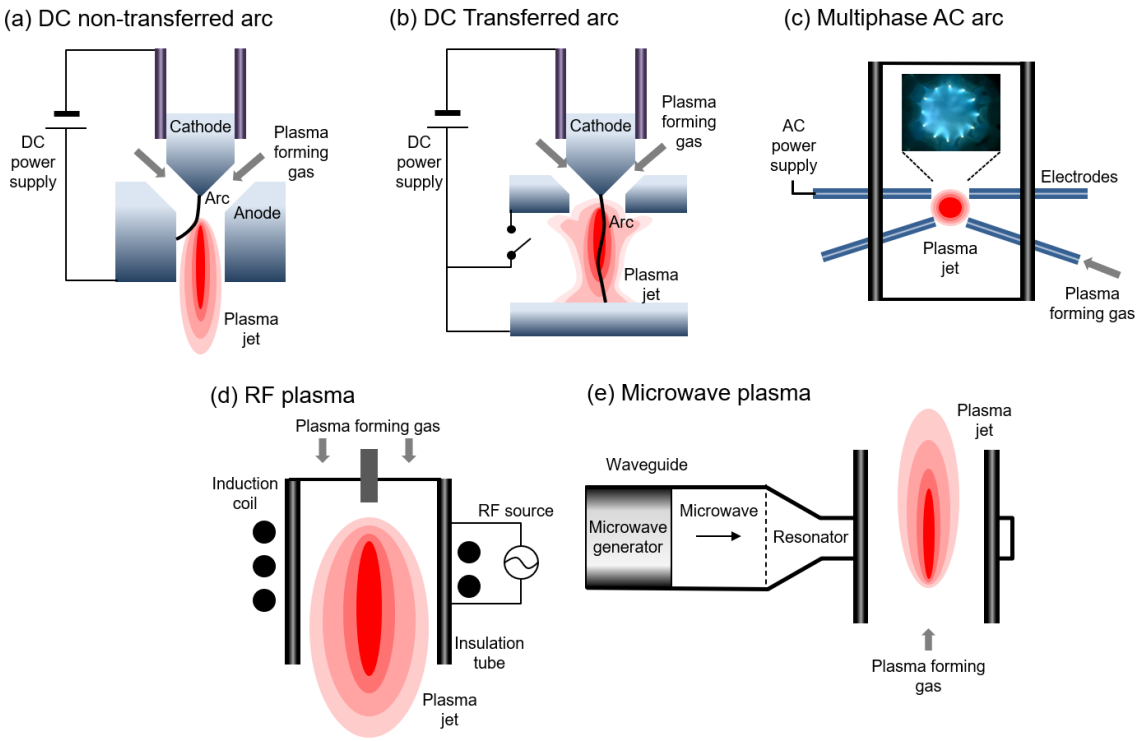

Fig. 1.7. Illustration of various thermal plasma torches.

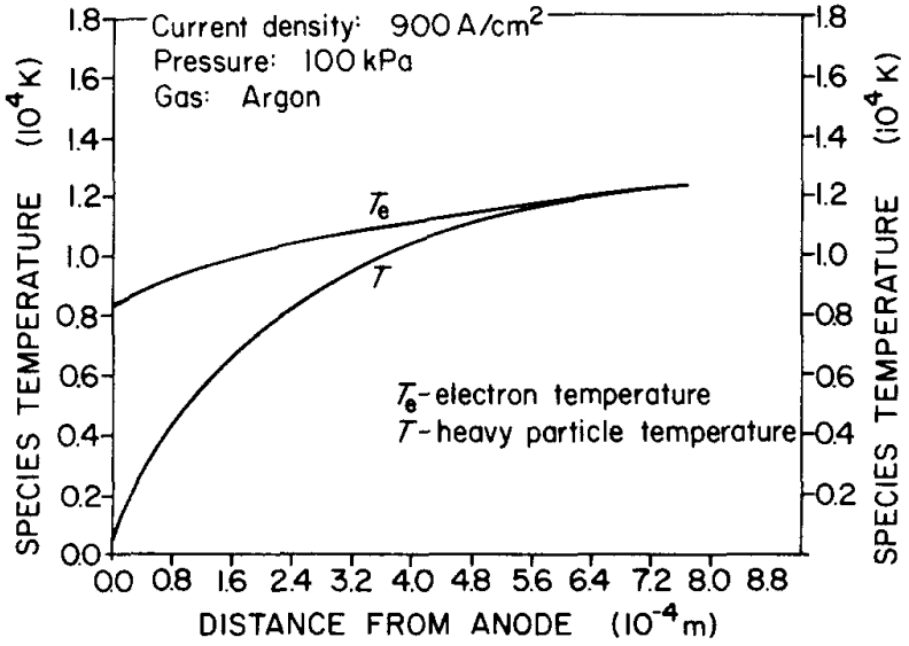

Fig. 1.8. The deviation between electron and heavy particle temperature within the anode boundary layer [11].

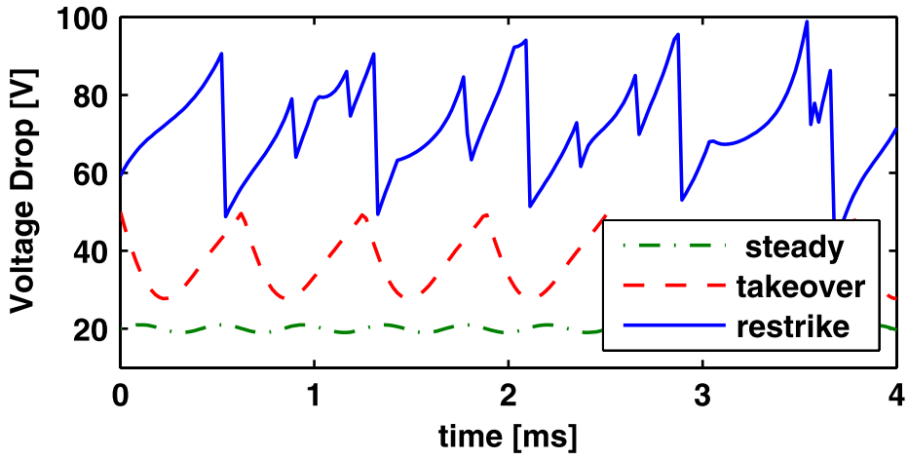

Fig. 1.9. Three fluctuation modes of arc voltage in an DC arc torch [96].

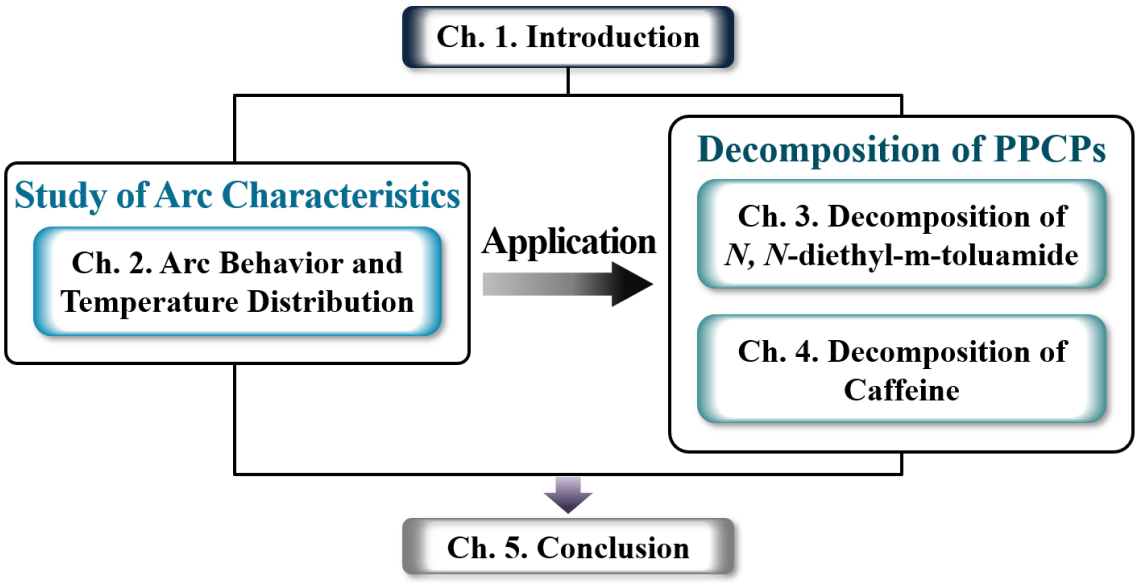

Fig. 1.10. Flow chart of the study.

2. Arc Behavior and Temperature Distribution in Water Plasma

2.1 Introduction

Thermal plasma is produced at high pressure (>10 kPa) using direct (DC) or alternating current (AC), radio frequency (RF), or microwave sources with temperatures around 2,000–20,000 K [1,2]. Due to unique advantages including high enthalpy with elevated temperature, oxidation or reduction atmospheres, and rapid quenching capability (10^5–10^6 K/s), thermal plasmas accelerate the kinetics of chemical reactions.

Water plasma as a sort of thermal plasma has attracted the most attention as a green technology for the treatment of organic wastes. This is due to a large amount of H, O, and OH radicals in the water plasma [3]. As shown in **Fig. 2.1** from the equilibrium composition of H_2O, large quantities of H_2, O_2, and OH are generated at approximately 3500 K with the dissociation of H_2O. Over 7500 K, H_2O is completely dissociated to H and O radicals and finally large amounts of electrons, H^+ and O^+ ions are generated. These radicals accelerate the chemical reaction, suppress byproduct formation, and a large amount of syngas like H_2 and CO can be produced. Also, the water molecule offers higher plasma enthalpy and thermal conductivity than those of commonly used plasma gases such as N_2 and Ar as shown in **Fig. 2.2** [4]. Therefore, the water plasma is considered as an innovative processing for the purpose of waste treatment [5–7].

However, a study of fundamental arc characteristics such as arc fluctuation and temperature in the water plasma is not clarified despite significantly affecting on the arc stability, process consistency, electrode power, and further heat transfer [8,9]. Even though H_2O steam was used in thermal plasma, they have only taken advantages of the characteristics of H_2O for the

decomposition and gasification of organic compounds [7,10]. The arc fluctuation, on the other hand, was studied by water plasma [11]. However, the study also mainly focused on the decomposition of D-glucose. Also, only temperature of plasma jet from the nozzle was largely investigated without arc temperature [12,13]. A study on the fundamental arc characteristics of the water plasma is therefore inevitable.

An inventive mist generation system was first applied to investigate the arc characteristics in this study. The plasma gas in the water mist form generated by the ultrasonic generator provides a stable feeding system, which results in a low density and high plasma enthalpy. The mist can also act as a function for electrode cooling compared to other processes [7,10]. Further descriptions for the mist generation can be found in section 2.2.1.

In this chapter, the investigation of arc fluctuation and temperature were verified in water plasma with an inventive stable mist feed system for better practical application in waste treatment. The effect of mist feeding rate on the arc characteristics is discussed using a high-speed camera and band-pass filters.

2.2 Experimental

2.2.1 Experimental Setup

A schematic diagram of the water plasma system with mist generation is presented in **Fig. 2.3**. The plasma torch is a DC non-transfer arc generator of coaxial design with a cathode of hafnium embedded into a copper rod (o.d.: 7 mm, height: 27 mm) and a nozzle-type copper anode (nozzle exit diameter: 1.8 mm). The diameter of hafnium in the cathode was 1.0 mm. The use of hafnium as a cathode material can prevent erosion and exhibit a longer operating time in an oxidative atmosphere.

An ultrasonic generator (o.d.: 20 mm) at the bottom of the torch consists of a piezoceramic and generates an ultrasonic wave at a frequency of 2.5 MHz which affects the surface of the solution. Therefore, water mist as a plasma gas can be generated by atomizing the solution. Herein, the amount of mist can be controlled by a power supply (Ultrasonic Humidifier, SIS Corp.) attached to the ultrasonic generator, which can change the amplitude of the ultrasonic wave by rotating a regulator on the power supply. Hence, the mist feeding rate was controlled in this work.

The generated water mist flows directly into the discharge area. Thereafter, the water plasma is generated at the discharge region by heating and ionization of the mist. Simultaneously, the anode is cooled by the mist, whereby the torch can be operated without carrier gas or air injection, a cooling control system, and pressure control devices. Therefore, this system presented not only can be used as a portable lightweight system without an additional gas supply system but also offers a higher energy efficiency than 90%. In addition, H, O, and OH radicals generated in the water plasma play a major role in suppressing byproduct formation.

The experimental condition for plasma generation is indicated in **Table 2.1**. An ethanol solution as a model substance of water-soluble organic compounds was introduced into the torch after adjusting the solution concentration to 5.0 mol% ethanol-water solution (purity: 99.8%, guaranteed reagent, Wako Pure Chemical Industries, Ltd.) with distilled water. The concentration of generated mist is the same as that of the solution. The regulator on the power supply for controlling the mist feeding rate was set at the position of the maximum, half, and minimum, respectively. The distance between electrodes was adjusted to 2.0 mm in order to generate a steady-state plasma. Then, the plasma was discharged using a DC power supply. The current was fixed at 6.0 A and the mean arc voltage was in the range of 130 to 200 V. Each run was operated for 10–30 min after reaching a steady-state operation condition. All experiments were performed at room temperature under atmospheric pressure.

2.2.2 Observation of Arc Fluctuation

2.2.2.1 High-Speed Camera Measurement with an Oscilloscope

A schematic diagram for observation of arc fluctuation is illustrated in **Fig. 2.4**. The arc fluctuation at the anode nozzle exit was visualized using two high-speed cameras (FASTCAM SA-5, Photron Ltd. and Phantom Miro LAB110, Vision Research Inc.). The two high-speed cameras were installed on the top and side of the torch and recorded at speeds of 4.2×10^5 fps and 2.2×10^5 fps with a shutter speed of 1 μs, respectively. Moreover, in order to clarify the relationship between the arc fluctuation and arc voltage, the arc voltage was measured by an oscilloscope (Scope Corder DL850, Yokogawa Corp.) synchronized with the high-speed cameras at a sampling rate of 10 MHz.

The obtained high-speed images were analyzed to reveal the temporal and spatial characteristics of arc and plasma. The captured images of the plasma arc were transformed into binary images in black and white by the appropriate threshold value to estimate the luminance area of the plasma arc.

2.2.2.2 Fast Fourier Transform Calculation

Fourier transform is widely used to analyze waves in the frequency domain. The fast Fourier transform (FFT) is used to figure out the frequency domain spectrum [14]. In this study, FFT is applied to the voltage waveform to analyze the frequency spectrum due to a periodic saw-tooth fluctuation of arc in water plasma.

2.2.2.3 Arc Area Existence Probability Calculation

Arc fluctuation shows periodic behavior due to the electrical breakdown between the arc and the nozzle wall as it reaches a certain potential difference. Therefore, in order to evaluate the

spatial characteristics of the arc, the existence probability was calculated. By superimposing 1000 images taken from a high-speed camera during the arc shunting about 150 times, the existence probability was calculated.

2.2.3 Temperature Measurement

2.2.3.1 High-Speed Camera Measurement with Band-Pass Filters

An observation system and temperature measurement method are presented in **Fig. 2.5**. A high-speed camera (Phantom V2512, Vision Research) with band-pass filters was used to observe the fluctuated temperature distribution on a millisecond time scale. Emission from thermal plasma basically consists of line spectra due to electronic transitions in the plasma, and continuous spectra due to radiation from the electrode and hot walls. In order to measure the temperature, only the line spectra should be extracted. Therefore, an optical system (MSI-2, Photron Ltd.) including the band-pass filters was combined with the high-speed camera. The emissions from the arc are split into two light paths by a splitter. After that, two-dimensional emission intensity distributions at each wavelength are observed on the charge-coupled device (CCD) by the band-pass filters which transmit different wavelengths. The typical frame rate and shutter speeds were 3.8×10^5 fps and 5 μs, respectively.

The wavelengths of H_α (656.3 nm) and H_β (486.1 nm) in hydrogen atom line spectrums were measured by spectroscopic measurements for temperature measurement as shown in **Fig. 2.6**. Other emissions overlapped with the above wavelengths were not detected. Therefore, the band-pass filters with transmission wavelengths of 656±5 nm and 486±5 nm were selected to measure the emission intensity in H_α and H_β, respectively. Subsequently, the sensitivity of the whole system including the camera, filters, lenses, and mirrors was calibrated for both wavelengths on the basis

of a tungsten lamp. The synchronized images from different wavelengths were observed. An oscilloscope was used to synchronize the arc phase and temperature distribution at a sampling rate of 10 MHz.

2.2.3.2 Boltzmann Plot Method

The temperature measurement was conducted on the basis of the Boltzmann plot method. The Boltzmann plot method is a simple and widely used method for spectroscopic measurement, especially for measuring the electron temperature of plasma by using the relative intensities of two or more lines spectra having a relatively large energy difference. To practically apply the Boltzmann plot method for the measurement of electron temperature, the excitation level needs to be reached under LTE condition. The basic principle of the Boltzmann plot method is described below [15,16] and the definition of symbols is shown in **Table 2.2**.

$$I_{pq} = \frac{A_{pq} g_p S}{\lambda} \cdot \frac{hcn}{4\pi U} exp\left(-\frac{E_p}{k_B T}\right) \tag{2.1}$$

From Eq. (2.1), the ratio of emission intensities at different wavelengths can be expressed as follows:

$$\frac{I_{pq}}{I_{p'q'}} = \frac{A_{pq} g_p \lambda_{p'q'}}{A_{p'q'} g_{p'q'} \lambda_{pq}} exp\left(-\frac{E_p - E_{p'}}{k_B T}\right) \tag{2.2}$$

The intensity ratio can be expressed as a function of excitation temperature as follows:

$$ln\left(\frac{I_{pq} A_{p'q'} g_{p'q'} \lambda_{pq}}{I_{p'q'} A_{pq} g_p \lambda_{p'q'}}\right) = -\frac{1}{T} \cdot \left(\frac{E_{p'} - E_p}{k_B}\right) \tag{2.3}$$

The temperature can be calculated from the slope of the by plotting the term of energy and the term of intensity ratio in the horizontal axis and in the vertical axis, respectively. In this study, the line emissions of H_α (656.3 nm) and H_β (486.1 nm) from water dissociation were used for temperature measurement.

2.3 Experimental Results and Discussion

2.3.1 Effect of Mist Feeding Rate on Arc fluctuation

Figures 2.7, **2.8**, and **2.9** show the synchronized waveform of arc voltage and high-speed snapshots at the mist feeding rates of 45 mg/s, 50 mg/s, and 60 mg/s, respectively. The saw-tooth waveform owing to the restrike phenomenon was clearly observed at all mist feeding rates in **Figs 2.7 (a)**, **2.8 (a)**, and **2.9 (a)**. The restrike phenomenon is fundamentally attributed to the high mist feeding rate and low current [17]. In particular, the arc voltage increased with an increase of the mist feeding rate. This is because a higher arc voltage is necessary to decompose more ethanol solution at a higher mist feeding rate, corresponding to more energy for decomposition.

Figures 2.7 (b), **2.8 (b)**, and **2.9 (b)** show the high-speed snapshots and arc behaviors at different mist feeding rates. A dotted line in each figure represents an anode nozzle exit. Arc length from the nozzle exit increased with increasing the mist feeding rate. This is because a large volume of mist forms drag force on the arc and pushes it downstream [18], following a high pressure inside the torch. Therefore, a larger mist feeding rate leads to a further increase in the arc length, which is in agreement with numerical simulation [19].

The arc was not observed at all from side views at a mist feeding rate of 45 mg/s. This is due to the lower flow rate. In contrast, increased arc length appeared distinctly at mist feeding rates of 50 mg/s and 60 mg/s because of the relatively large mist feeding rates.

Meanwhile, the arc was not observed from the side view at 19 μs and 18 μs in the mist feeding rates of 50 mg/s and 60 mg/s, respectively. This is related to the arc reattachment in the restrike phenomenon. The arc reattachment process is well known as the formation of a new anode attachment closer to the cathode through a new current path by the breakdown of the arc according to periodic large voltage drops [20]. Previous experimental findings also reported a similar result [8].

The experimental image of the waveform of arc voltage, together with a schematic representation of the arc reattachment phenomenon, is shown in **Fig. 2.10**. The arc is dragged by mist flow at 6 μs, then, the length of the arc is more increases with an increase of arc voltage at 10 μs. If the arc voltage exceeds the breakdown voltage at 15 μs, a new arc attachment forms somewhere upstream with the lowest arc voltage at 19 μs. Once a new attachment is formed, the arc moves to downstream again by the incoming mist, starting an arc reattachment cycle.

FFT analysis was also conducted to clarify the fluctuation frequency of arc voltage at different mist feeding rates. The result is presented in **Fig. 2.11**. The frequencies at 33.6 kHz, 36.6 kHz, and 40.2 kHz were found at the mist feeding rates of 45 mg/s, 50 mg/s, and 60 mg/s, respectively. The increase of the mist feeding rate resulted in an increase of the frequency. This results from the stronger drag force at the larger mist feeding rates as discussed in the previous section.

The arc fluctuation in DC arc plasma depends on the balance between the drag force by the gas flow and Lorentz force caused by the interaction of the current and the self-induced magnetic field [21,22] as follows:

$$-(3\mu_o I^2/16\pi R_c)\left[1-\frac{7r_o^2}{18R_c^2}\right]cos\theta dL + C_D r_o \rho v^2 dL = 0 \qquad (2.4)$$

where μ_o is the magnetic permeability constant (1.26×10^{-6} Hy/m), I is the current (A), R_c is the radius of curvature of the anode column (mm), r_o is the radius of the anode column (mm), L is the arc length (m), C_D is the drag coefficient, ρ is the gas density (kg/m), and v is the axial component of the superimposed flow (m/s). The Lorentz force which is represented as the net magnetic body force and the drag force are indicated on the left and right terms in Eq. (2.4), respectively. r_o, R_c, and C_D are constant due to negligible change in the calculation. Therefore, the value of v increases significantly with the increase of feed rate. In this study, the value of the gas flow rate significantly increases with the increase of the mist feeding rate, which indicates that the drag force induced increases. Consequently, the fluctuation frequency increased with the increase of the mist feeding rate.

To study further characteristics of arc fluctuation, the arc existence probability was measured. Counter maps of the arc existence probabilities at different feed rates are shown in **Fig. 2.12**. The dotted line in each figure represents the anode nozzle exit. The existence probability was defined as the ratio of the time during which the arc existed to the total observation time. Therefore, the value of unity means that the arc always exists, and that of zero means it does not exist at all. The red color in the counter maps of the existence probability indicates that the arc always exists. As a result, at the same time as the feed rate increased, the existence probability in both axial and radial directions was evidently increased and so does arc length. The evidence suggests that the mist feeding rate plays a crucial role in controlling the arc area and length.

2.3.2 Effect of Mist Feeding Rate on Arc Temperature

Figures 2.13, **2.14**, and **2.15** present synchronized waveforms of arc voltage, high-speed snapshots, and excitation temperature distributions estimated by the Boltzmann plot method at the mist feeding rates of 40 mg/s, 50 mg/s, and 60 mg/s, respectively. The synchronized waveforms of the arc voltage are shown in **Figs 2.13 (a)**, **2.14 (a)**, and **2.15 (a)**. **Figures 2.13 (b)**, **2.14 (b)**, and **2.15 (b)** show the high-speed snapshots and arc temperature distributions at different mist feeding rates. High-temperature regions on the arc correspond to a bright area in the high-speed snapshots. The arc temperature has a range of approximately 4,000–10,000 K.

The highest temperature was observed in the center of the arc, and the temperature decreased along the radial direction from the center in all cases. It is explained by the swirl motion of the plasma gas, which stabilizes the arc generating the centrifugal force within the nozzle. On the contrary, the arc periphery is affected by the mixture of cold and hot gases, that is, the temperature near the arc periphery became lower than the center of the arc [23]. Meanwhile, the arc was not observed at mist feeding rates of 50 mg/s and 60 mg/s (29 μs and 22 μs, respectively), which is

attributed to the arc anode reattachment as discussed in the section 2.3.1.

The arc area according to the temperature was investigated when most stretched to confirm the effect of the mist feeding rate. **Figure 2.16** shows the arc area with temperatures of higher than 6,000 K and 9,000 K at the mist feeding rates of 40 mg/s, 50 mg/s, and 60 mg/s, respectively. The arc area with temperatures higher than 6,000 K and 9,000 K increased with the increase of the mist feeding rate. The reason is as follows: the arc is more contracted, and the arc length increases along with the arc voltage, which can maintain a long arc, and thus more energy can be retained at the nozzle exit.

In addition, this result is in good agreement with an earlier report about the relationship between the distribution of arc potential and heat flows along the channel, which showed that the arc potential monotonically rises as well as the intensity of heat transfer to the wall by convection [23]. Therefore, despite the increase of decomposition energy at the higher mist feeding rate, the increased input power exceeded the decomposition energy by the increase of the arc voltage, and the area with the high temperature increased. Consequently, it is demonstrated that the arc area with the high temperature can be controlled by different mist feeding rates.

2.4 Conclusion

Arc discharge characteristics, arc fluctuation and temperature distribution, were successfully investigated in water plasma. In particular, the mist was supplied by a mist generator as a plasma gas without any cooling or carrier gas devices, which could provide a stable feeding. The effect of mist feeding rate on the plasma fluctuation and temperature distribution was studied using high-speed cameras synchronized with an oscilloscope. The main concluding remarks are summarized as follows: As the mist feeding rate increased, the arc voltage and length increased. This was due to the stronger drag force. On the other hand, the arc was not observed from a side

view at a lower mist feeding rate of 45 mg/s with lower arc voltage. This results from the low mist feeding rate. The arc fluctuation was in a restrike mode by low arc current and high feed rate in this study, by which the arc reattachment process could also be observed.

The arc temperature distribution was visualized by a high-speed video camera and band-pass filters based on the Boltzmann plot method. The temperatures higher than 6,000 K and 9,000 K area were increased. This is due to the increase of the arc voltage as well as heat convection. It was feasible to control the arc fluctuation and area with a high temperature through a flow parameter. Based on the study, the water plasma with a mist generation system could play a potentially crucial role in the practical application of waste treatment.

References

[1] A.B. Murphy, D. Uhrlandt, Foundations of High-Pressure Thermal Plasmas, Plasma Sources Science and Technology 27(6) (2018) 063001.

[2] J. Heberlein, A.B. Murphy, Thermal plasma waste treatment, Journal of Physics D: Applied Physics 41(5) (2008) 053001.

[3] H. Nishioka, H. Saito, T. Watanabe, Decomposition mechanism of organic compounds by DC water plasmas at atmospheric pressure, Thin Solid Films 518(3) (2009) 924–928.

[4] L.A. Sphaier, J. Su, R.M. Cotta, F.A. Kulacki, Handbook of thermal science and engineering, Springer, 2017.

[5] A. Tamošiūnas, P. Valatkevičius, V. Grigaitienė, V. Valinčius, N. Striūgas, A cleaner production of synthesis gas from glycerol using thermal water steam plasma, Journal of Cleaner Production 130 (2016) 187–194.

[6] T. Watanabe, Narengerile, Decomposition of Glycerine by Water Plasmas at Atmospheric Pressure, Plasma Science and Technology 15(4) (2013) 357–361.

[7] M. Hrabovsky, M. Hlina, V. Kopecky, A. Maslani, O. Zivny, P. Krenek, A. Serov, O. Hurba, Steam Plasma Treatment of Organic Substances for Hydrogen and Syngas Production, Plasma Chemistry and Plasma Processing 37(3) (2017) 739–762.

[8] Z. Duan, J. Heberlein, Arc instabilities in a plasma spray torch, Journal of Thermal Spray Technology 11(1) (2002) 44–51.

[9] J.L. Dorier, M. Gindrat, C. Hollenstein, A. Salito, M. Loch, G. Barbezat, Time-resolved imaging of anodic arc root behavior during fluctuations of a DC plasma spraying torch, IEEE

Transactions on plasma science 29(3) (2001) 494–501.

[10] A. Tamošiunas, D. Gimžauskait, M. Aikas, R. Uscila, M. Praspaliauskas, J. Eimontas, Gasification of Waste Cooking Oil to Syngas by Thermal Arc Plasma, Energies 12(13) (2019) 2612.

[11] Y. Ozeki, T. Matsuo, M. Tanaka, T. Watanabe, Characteristics of water thermal plasma for biomass utilization system, Journal of Fluid Science and Technology 12(3) (2017) JFST0022.

[12] O. Hurba, M. Hlìna, M. Hrabovský, Diagnostics of Plasma Jet Generated in Water/Argon DC Arc Torch, Plasma Physics and Technology 3(1) (2016) 5–8.

[13] A. Mašláni, V. Sember, M. Hrabovský, Spectroscopic determination of temperatures in plasmas generated by arc torches, Spectrochimica Acta Part B: Atomic Spectroscopy 133 (2017) 14–20.

[14] Q. Xiong, S. Ji, L. Zhu, L. Zhong, Y. Liu, A Novel DC Arc Fault Detection Method Based on Electromagnetic Radiation Signal, IEEE Transactions on Plasma Science 45(3) (2017) 472–478.

[15] H.R. Griem, Principles of plasma spectroscopy, 2005.

[16] N. Ohno, M.A. Razzak, H. Ukai, S. Takamura, Y. Uesugi, Validity of Electron Temperature Measurement by Using Boltzmann Plot Method in Radio Frequency Inductive Discharge in the Atmospheric Pressure Range, Plasma and Fusion Research 1 (2006) 028.

[17] J. Coudert, M. Planche, P. Fauchais, Characterization of dc plasma torch voltage fluctuations, Plasma Chemistry and Plasma Processing 16(1) (1995) S211–S227.

[18] J.P. Trelles, C. Chazelas, A. Vardelle, J.V.R. Heberlein, Arc Plasma Torch Modeling, Journal of Thermal Spray Technology 18(5-6) (2009) 728–752.

[19] Z. Guo, S. Yin, H. Liao, S. Gu, Three-dimensional simulation of an argon-hydrogen DC non-transferred arc plasma torch, International Journal of Heat and Mass Transfer 80 (2015) 644–652.

[20] E. Moreau, C. Chazelas, G. Mariaux, A. Vardelle, Modeling the Restrike Mode Operation of a DC Plasma Spray Torch, Journal of Thermal Spray Technology 15(4) (2006) 524–530.

[21] F. Liang, M. Tanaka, S. Choi, T. Watanabe, Formation of different arc-anode attachment modes and their effect on temperature fluctuation for carbon nanomaterial production in DC arc discharge, Carbon 117 (2017) 100–111.

[22] M. Tanaka, H. Soeda, T. Watanabe, T. Koga, Plasma jet characteristics in long DC arc with ring-shaped anode, J. Fluid Sci. Tech. 13(4) (2018) JFST0027–JFST0027.

[23] M.F. Zhukov, I. Zasypkin, Thermal plasma torches: design, characteristics, application, Cambridge International Science Publishing, 2007.

Table 2.1. Experimental conditions for the investigation of arc characteristics.

Pressure [kPa]	101.3 (Atmosphere Pressure)
Temperature [℃]	25
Arc Current [A]	6.0
Mean Arc Voltage [V]	130–200
Plasma Supporting Gas	Water, Ethanol
Ethanol Solution Concentration [mol%]	5.0

Table 2.2. Nomenclature of emission-intensity equation.

I_{pq}	Emission intensity (p to q level) [-]
A_{pq}	Transition probability (p to q level) [s^{-1}]
g_p	Statistical weight [-]
S	Radiant sensitivity for CCD [mA/W]
λ	Wavelength [m]
h	Planck's constant [J・s]
c	Light speed [m/s]
n	Number density [m^{-3}]
U	Partition function [-]
E_p	Excitation energy [eV]
k_B	Boltzmann constant [eV/K]
T	Excitation temperature [K]

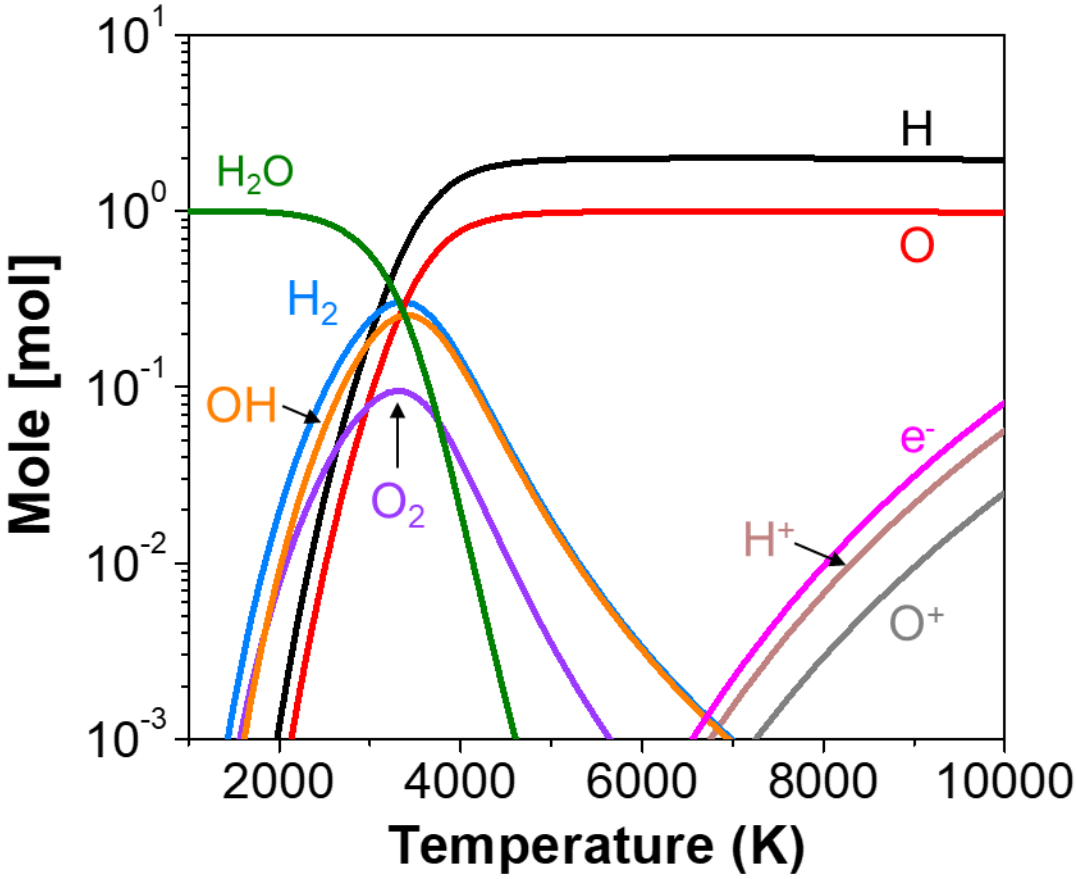

Fig. 2.1. Equilibrium composition of 1.0 mol water.

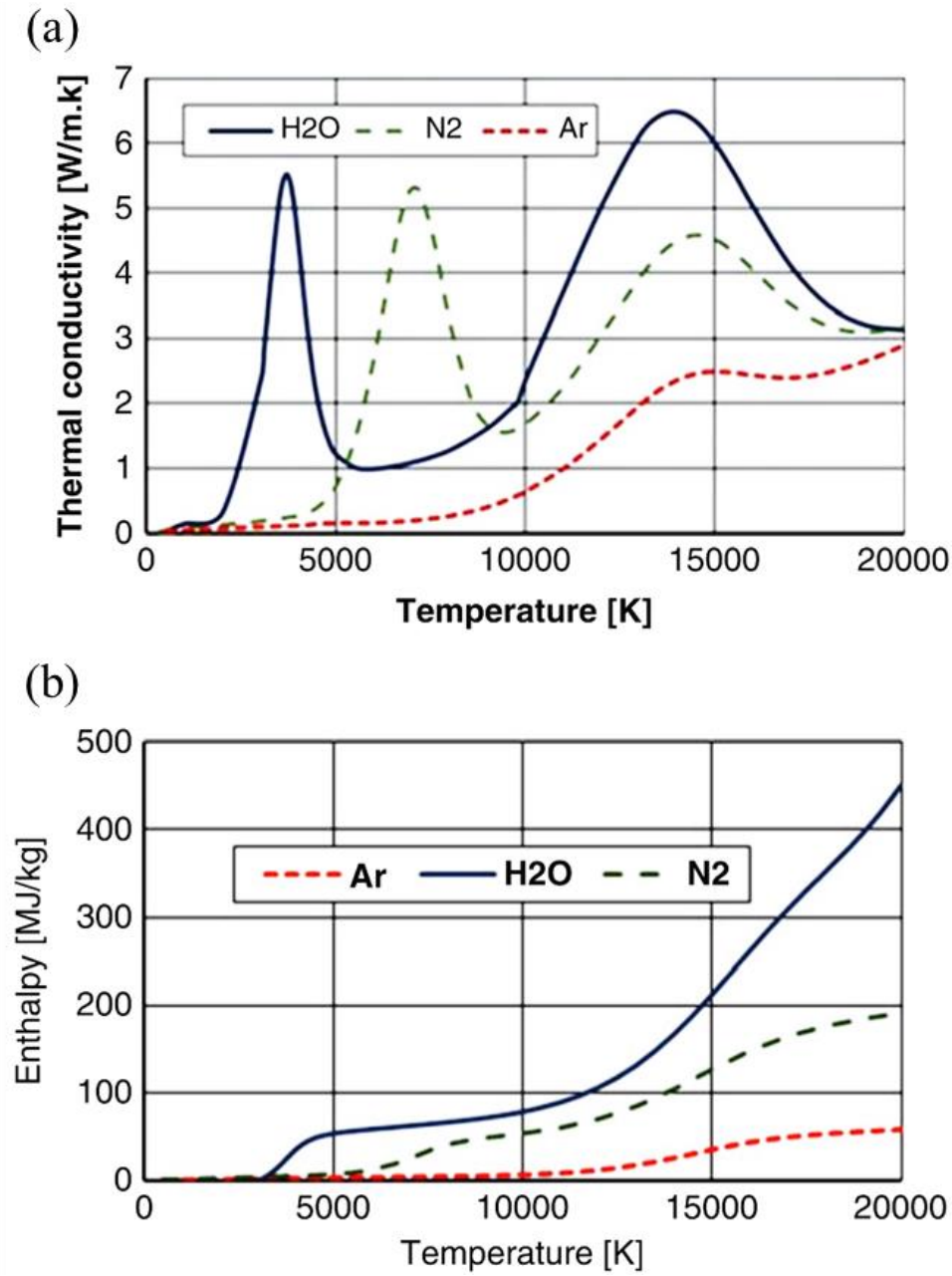

Fig. 2.2. Dependence of (a) thermal conductivity and (b) plasma enthalpy on plasma temperature for different plasma gases [4].

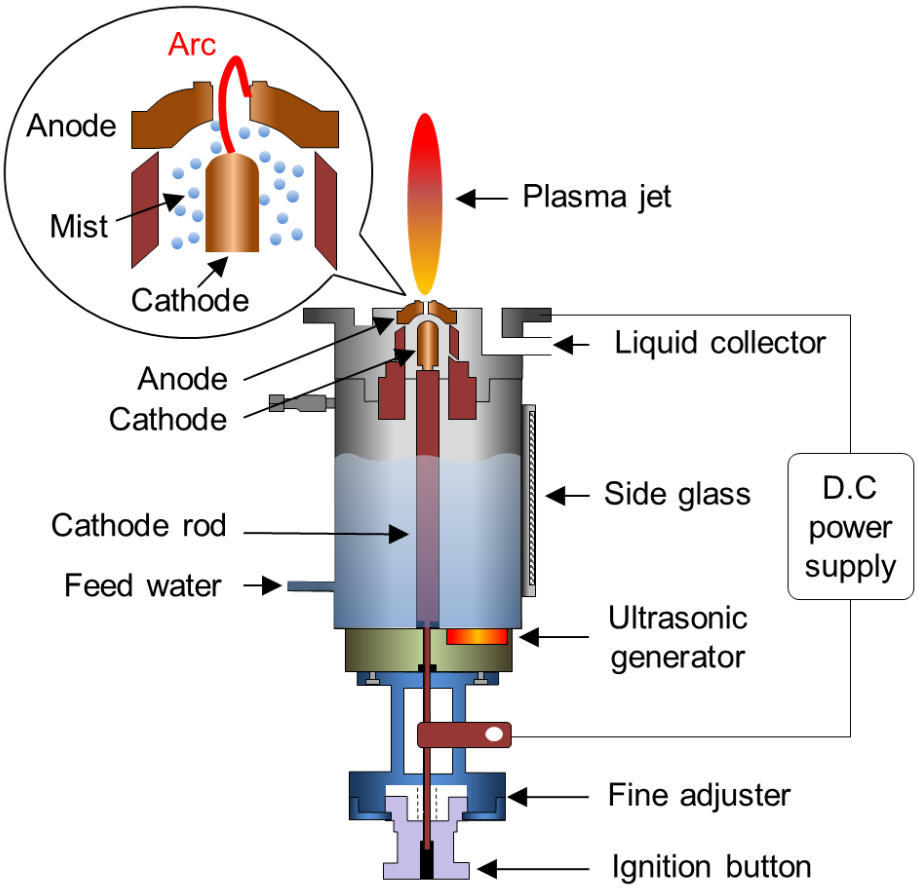

Fig. 2.3. Schematic diagram of water plasma system with mist generation.

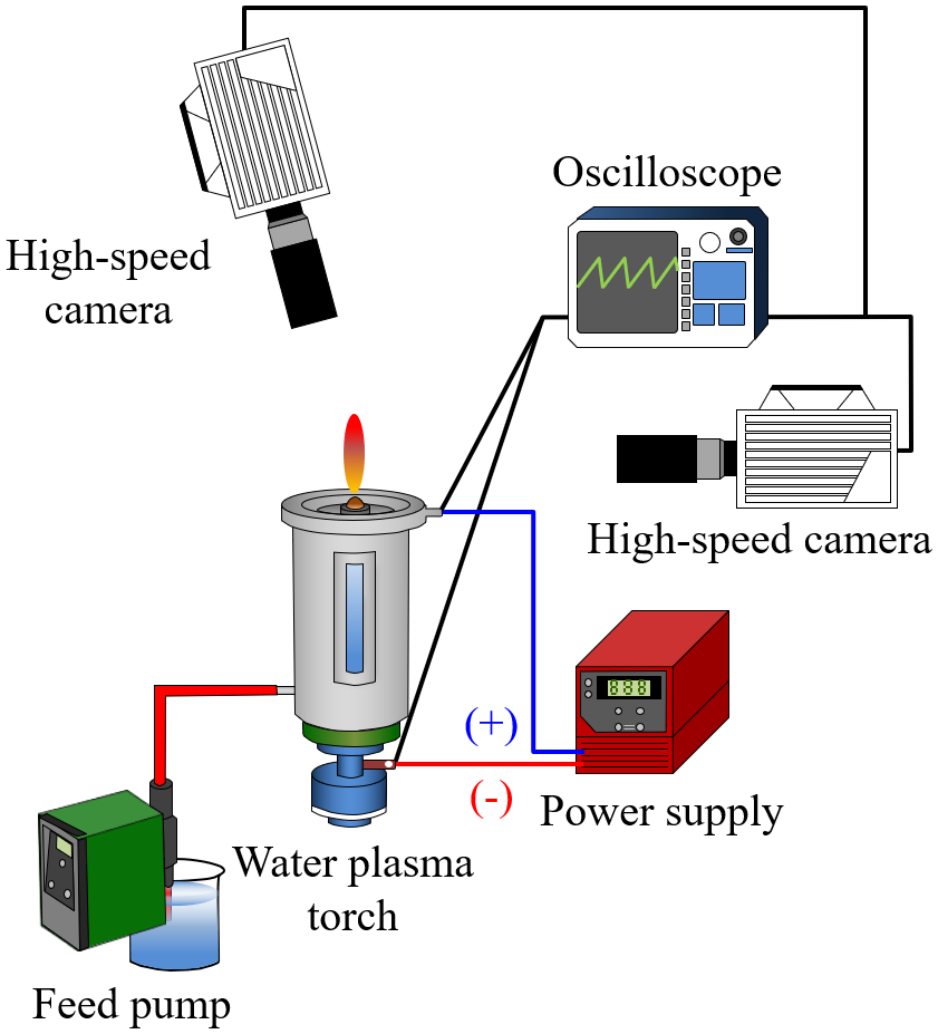

Fig. 2.4. Illustration for observation of arc fluctuation.

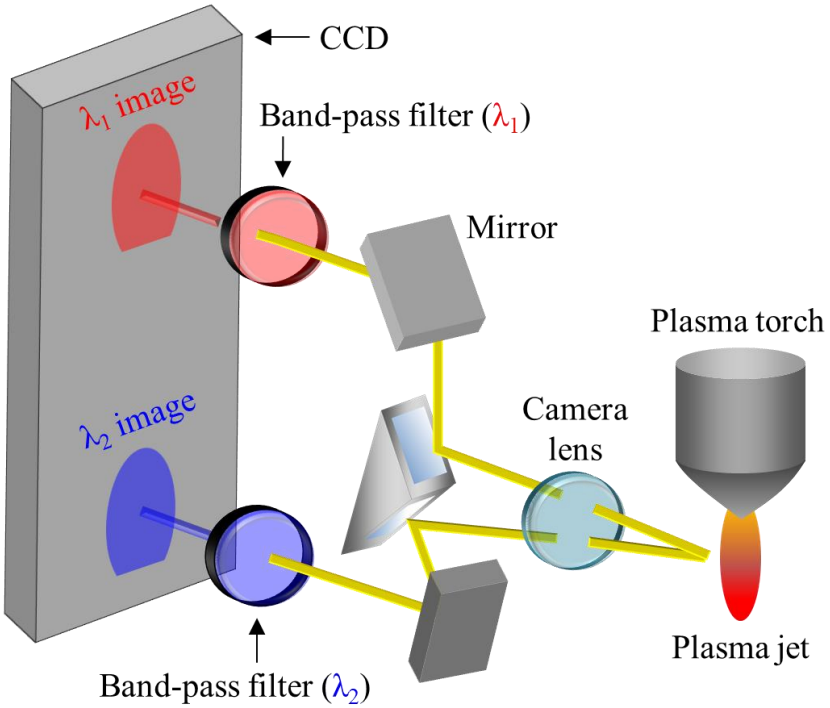

Fig. 2.5. Schematic diagram of observation system with a high-speed camera and band-pass filters.

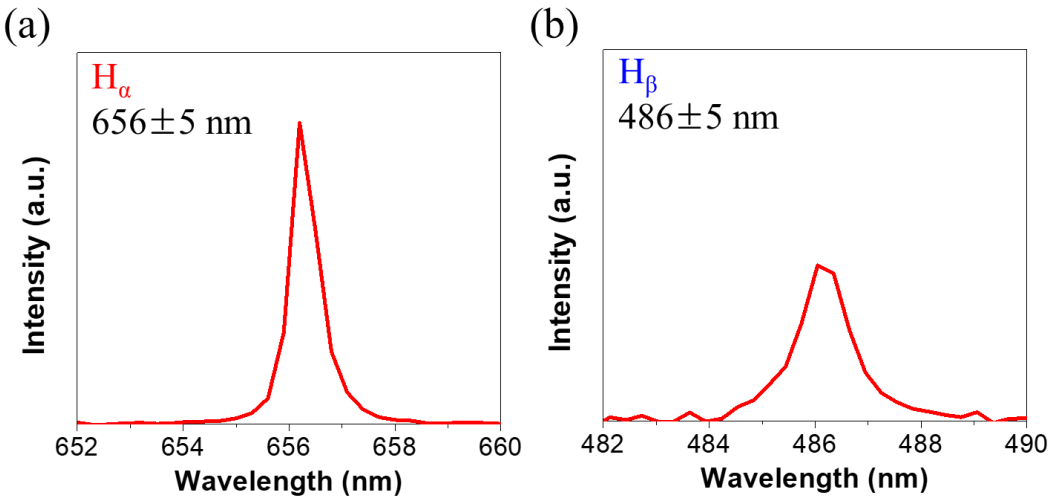

Fig. 2.6. Wavelengths of (a) H_α (656.3 nm) and (b) H_β (486.1 nm) in hydrogen atom line spectrums.

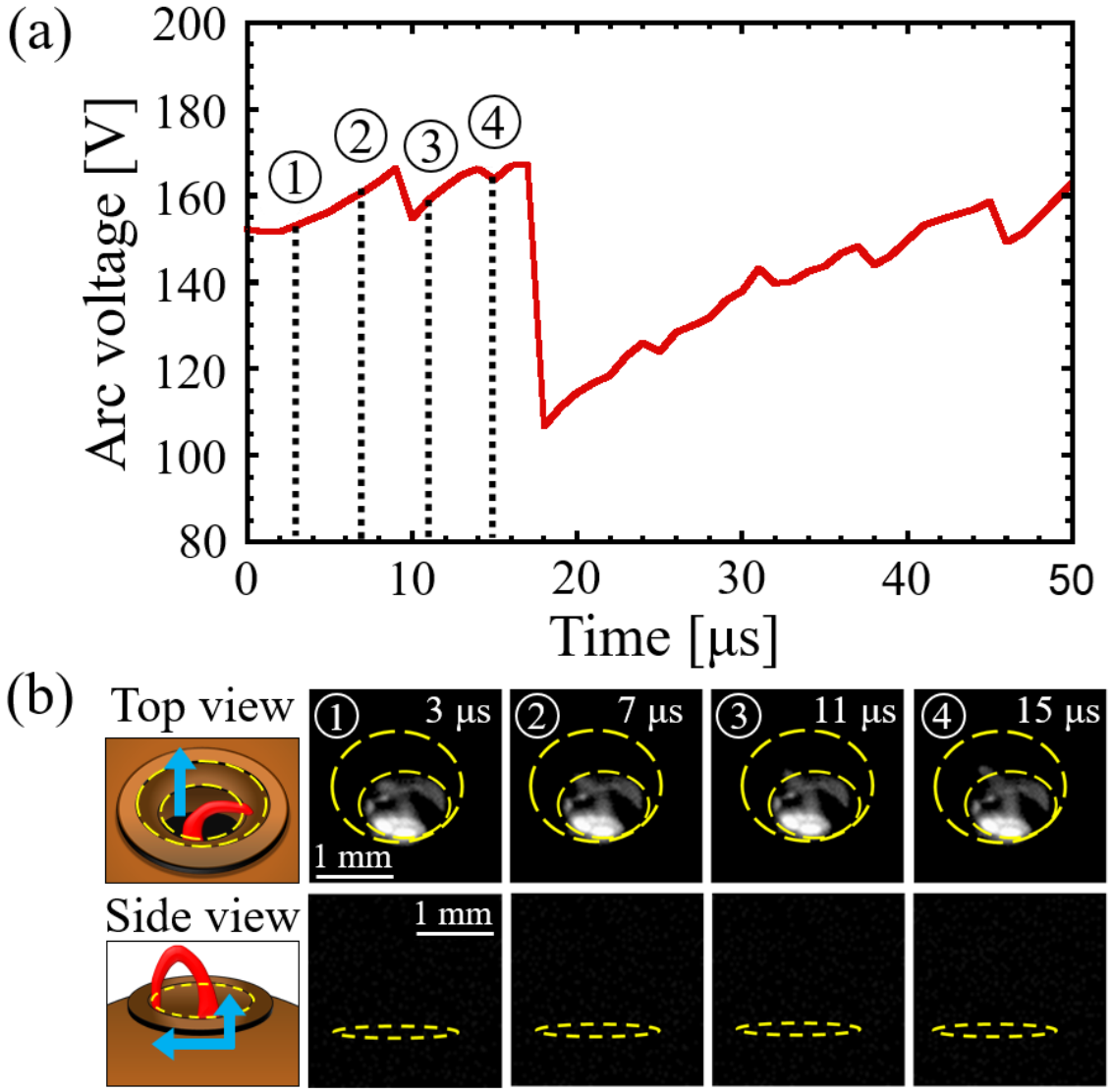

Fig. 2.7. (a) Synchronized waveform of arc voltage and (b) high-speed snapshots at mist feeding rate of 45 mg/s.

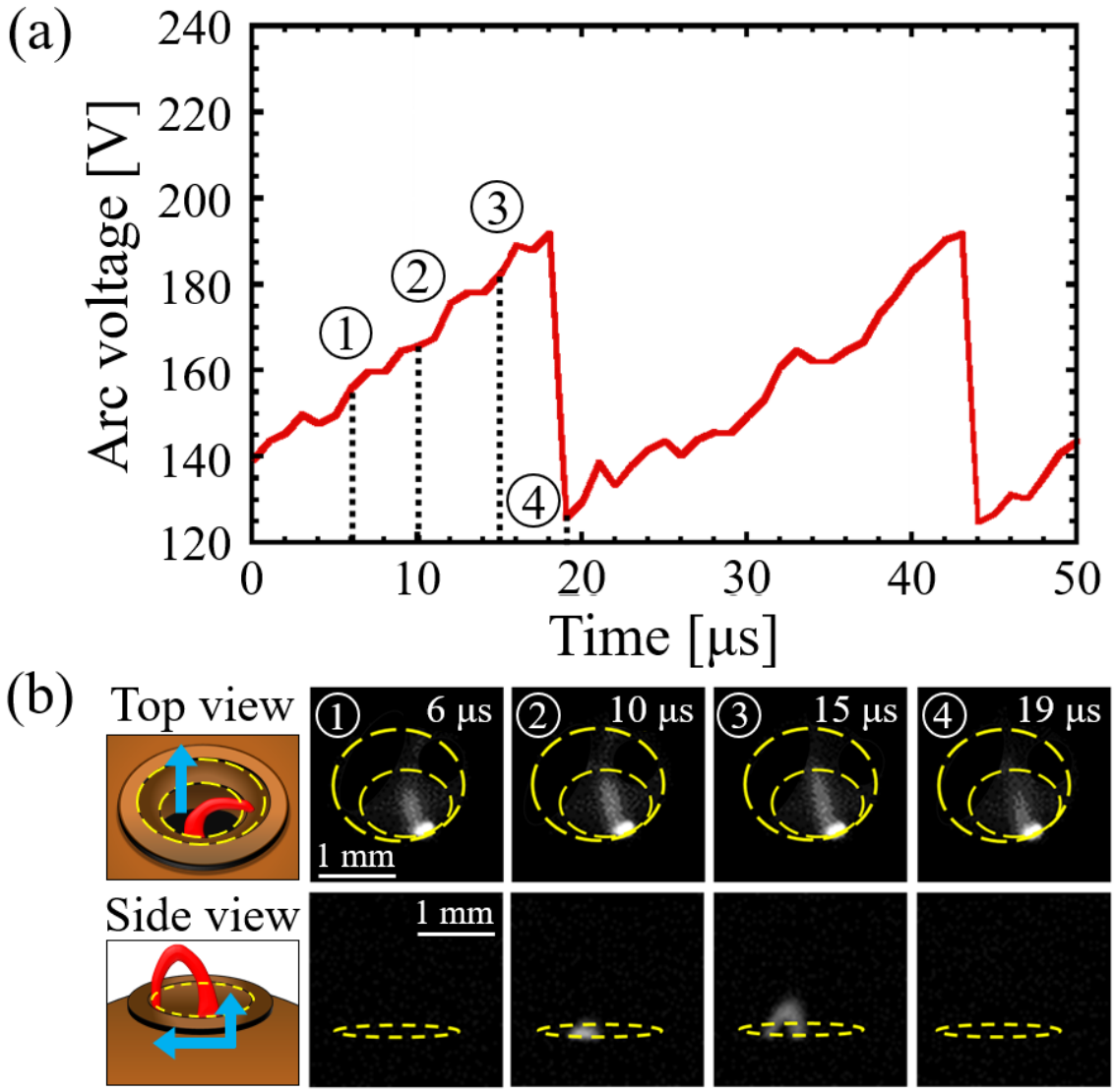

Fig. 2.8. (a) Synchronized waveform of arc voltage and (b) high-speed snapshots at mist feeding rate of 50 mg/s.

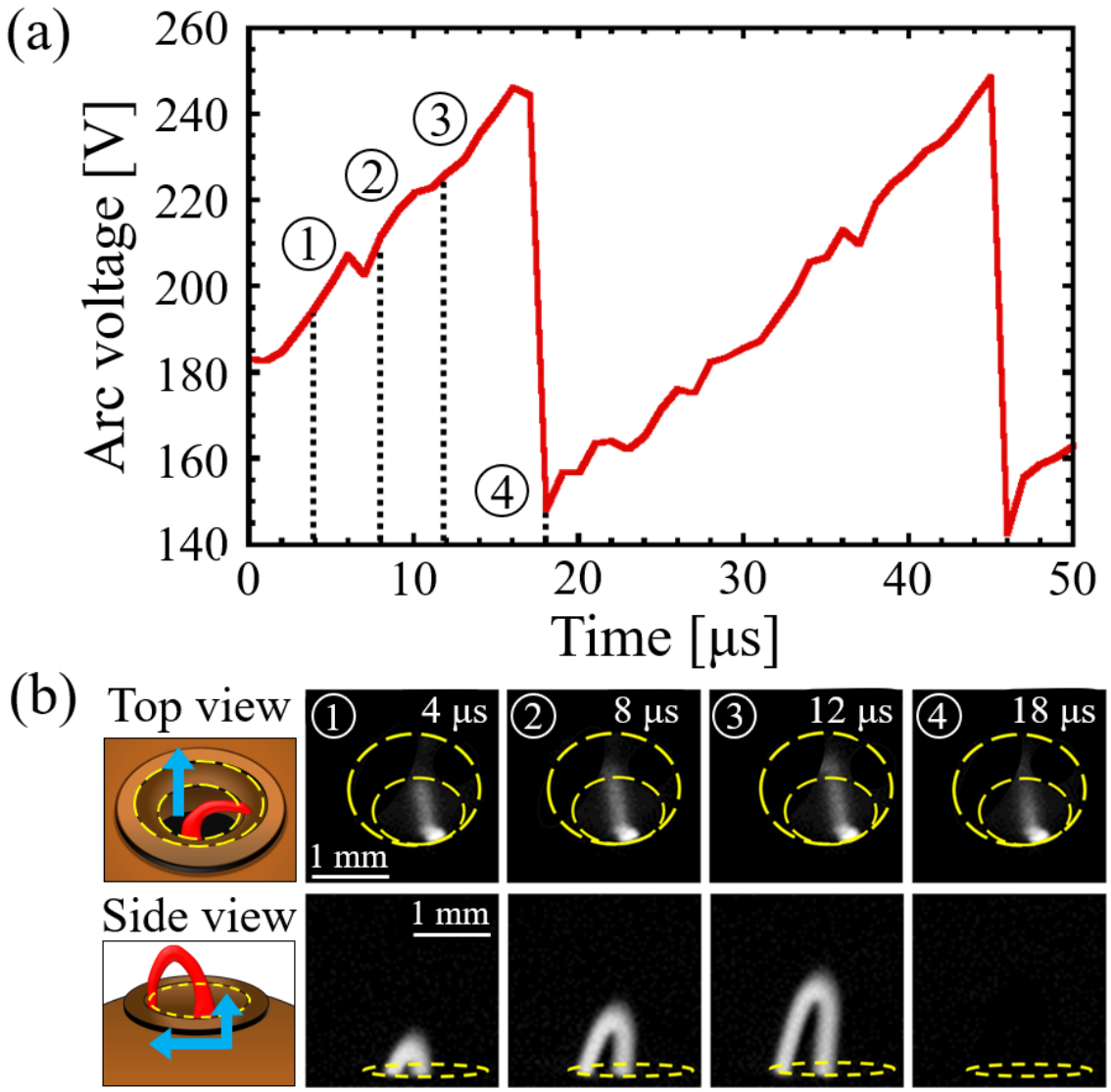

Fig. 2.9. (a) Synchronized waveform of arc voltage and (b) high-speed snapshots at mist feeding rate of 60 mg/s.

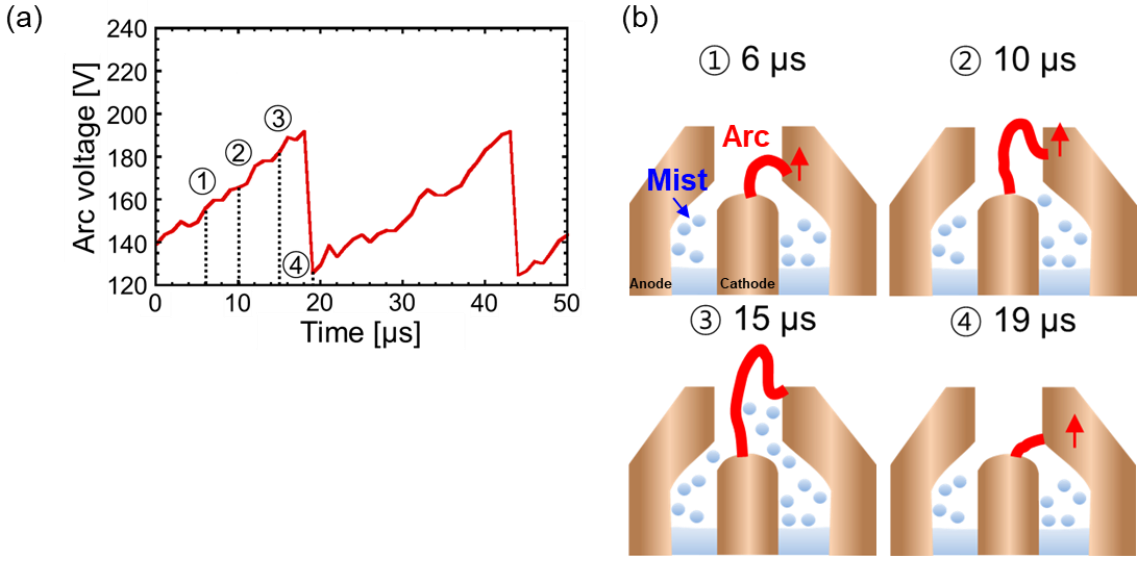

Fig. 2.10. (a) Waveform of arc voltage at mist feeding rate of 50 mg/s and (b) schematic representation of the arc reattachment.

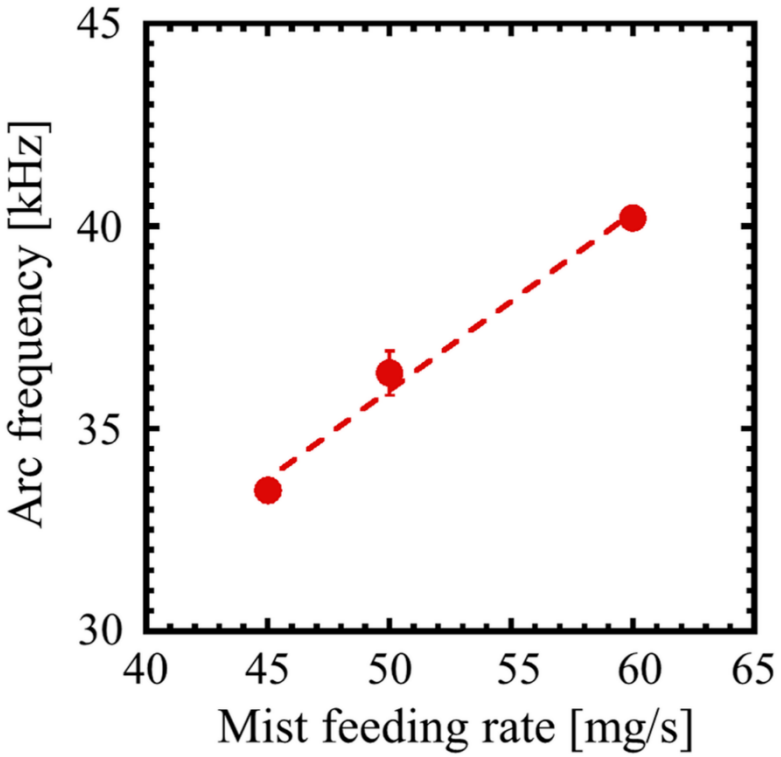

Fig. 2.11. Effect of mist feeding rate on the frequency of plasma arc fluctuation.

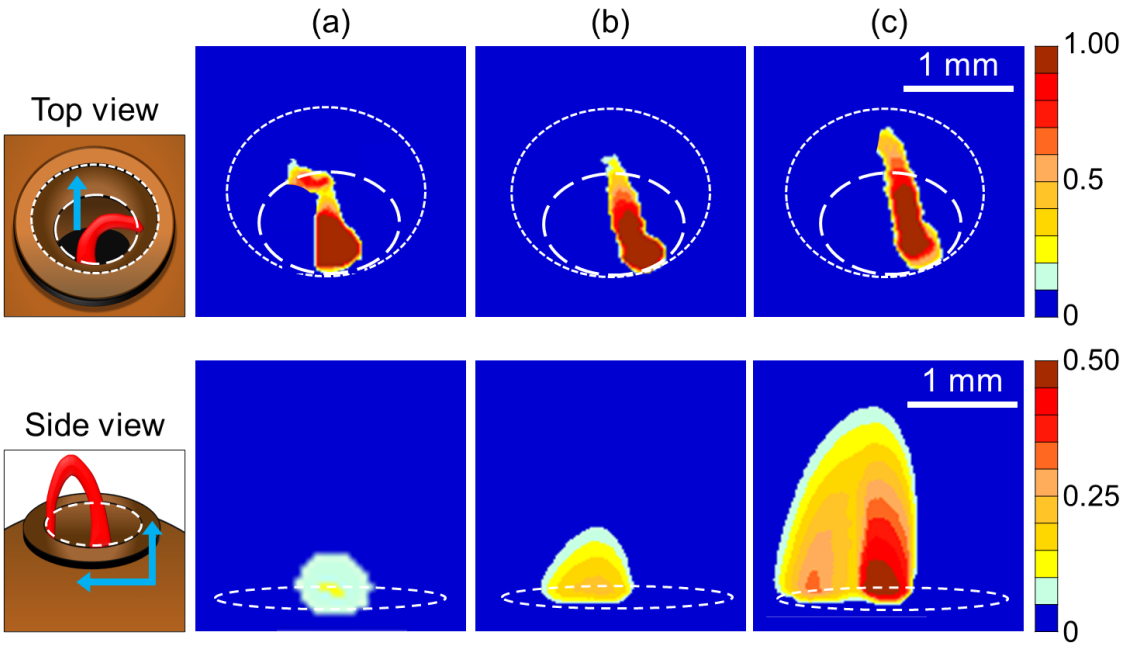

Fig. 2.12. Counter maps of arc existence probabilities at different feed rates of (a) 40 mg/s, (b) 50 mg/s, and (c) 60 mg/s, respectively.

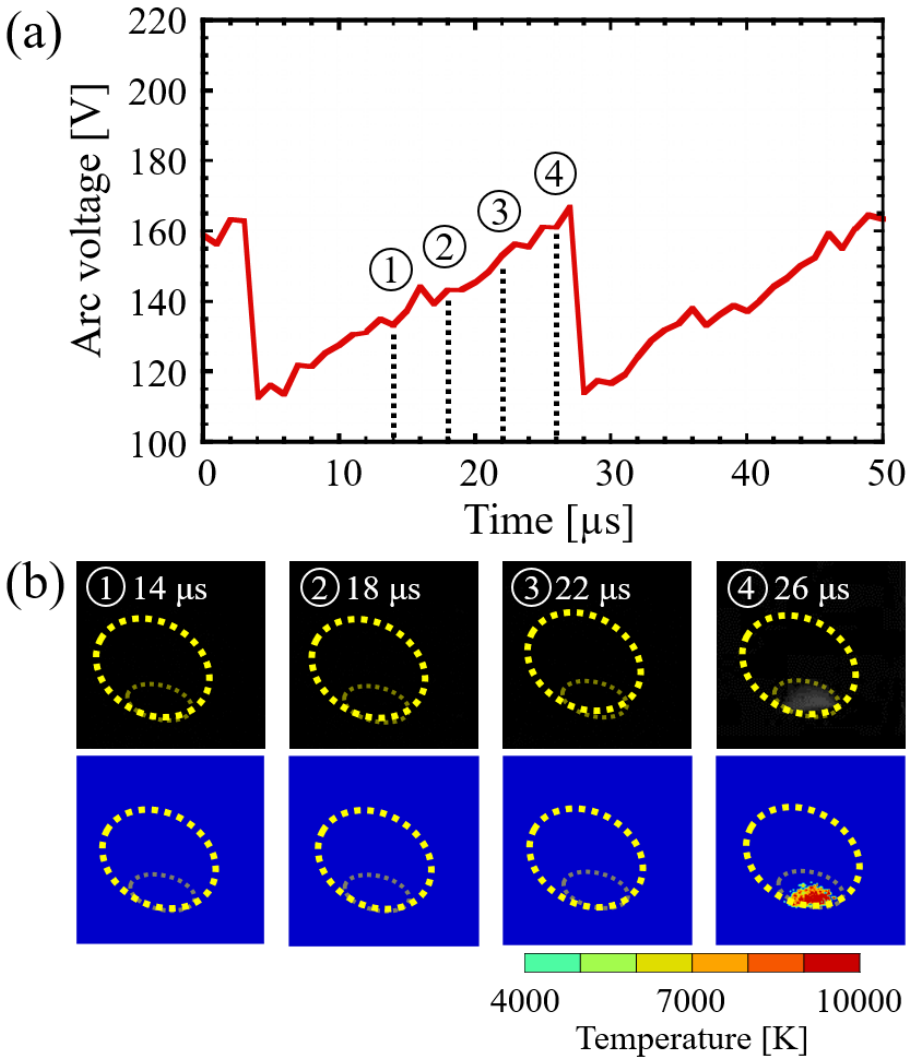

Fig. 2.13. (a) Synchronized waveform of arc voltage and (b) temperature distributions at mist feeding rates of 40 mg/s.

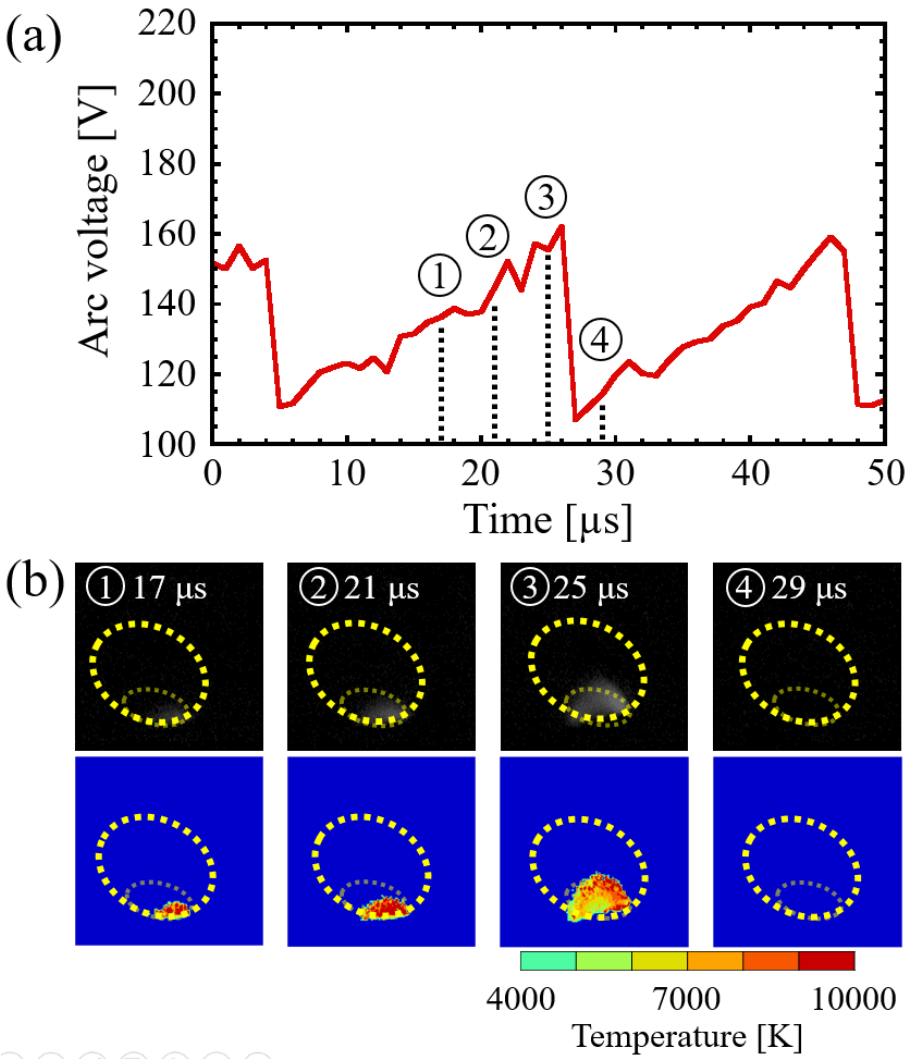

Fig. 2.14. (a) Synchronized waveform of arc voltage and (b) temperature distributions at mist feeding rates of 50 mg/s.

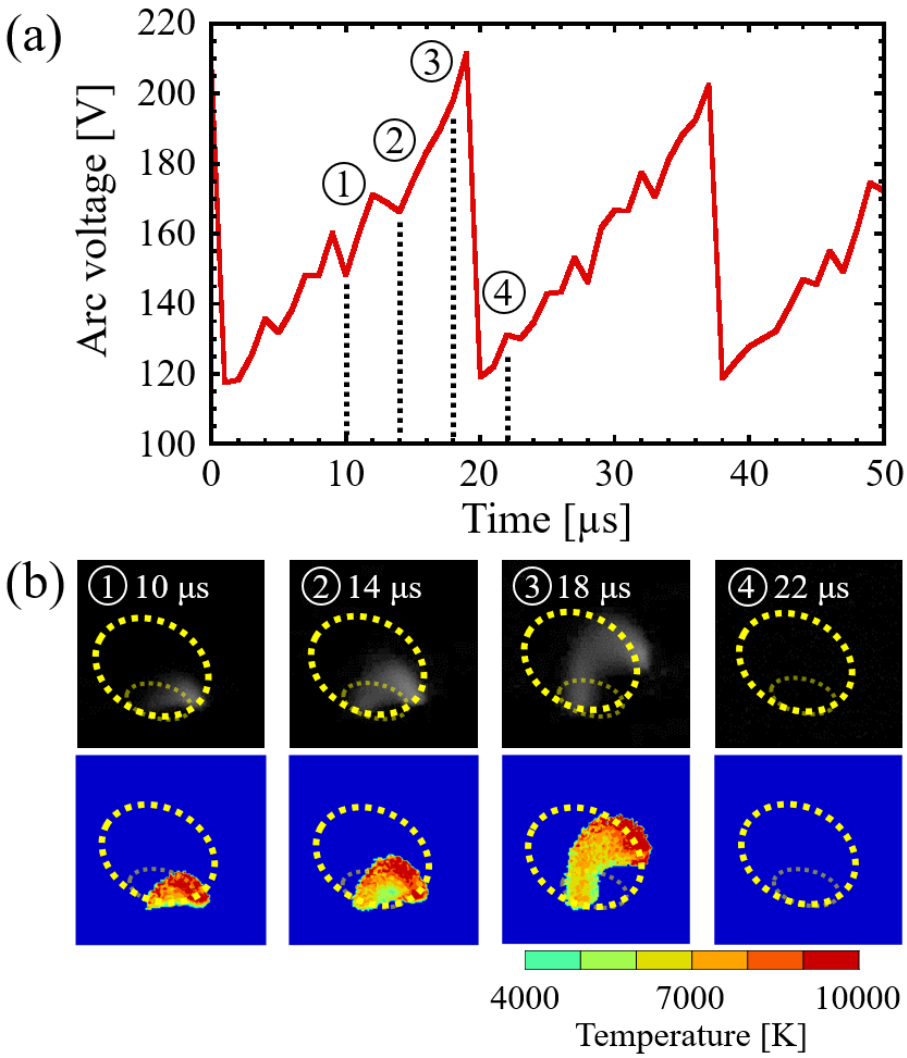

Fig. 2.15. (a) Synchronized waveform of arc voltage and (b) temperature distributions at mist feeding rates of 60 mg/s.

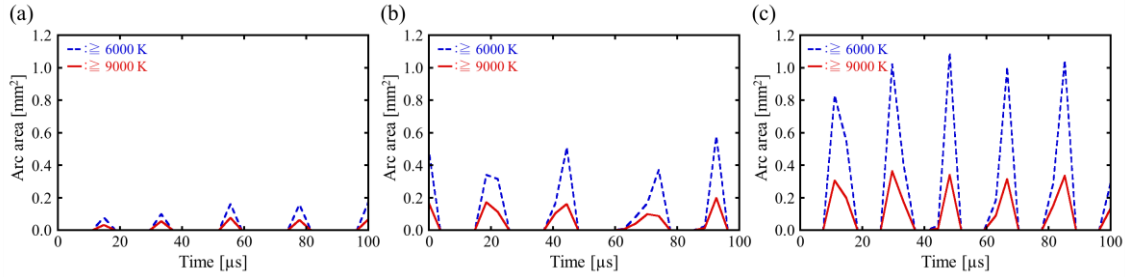

Fig. 2.16. Arc area with higher temperature than 6,000 K and 9,000 K at different mist feeding rates of (a) 40 mg/s, (b) 50 mg/s, and (c) 60 mg/s, respectively.

3. Decomposition of *N, N*-diethyl-m-toluamide by Water Plasma

3.1 Introduction

Pharmaceuticals and personal care products (PPCPs) have drawn considerable attention for therapeutic and beauty in day-to-day life, including in a broad range of medicines, cosmetics, and detergents for both humans and veterinary [1]. However, they have been widely detected in rivers, groundwater, urban areas, and even in drinking water around the world due to extensive use and continuous discharge into the aquatic system through bathing, excretion, and sewage treatment plants [2]. Therefore, PPCPs have been considered as emerging contaminants (ECs) [3].

N, N-diethyl-m-toluamide, commonly known as DEET, has been broadly adopted as a primary insect repellent among PPCPs for more than a half-century, protecting humans and animals from mosquitoes and other blood-sucking insects [4]. The physicochemical properties of DEET are shown in **Table 3.1**. Due to its effectiveness and low cost, it has been extensively employed by means of sprays, balms, and gels, which is however followed by unintentionally washing off and excretion into the waterway via sewage effluent [5]. Therefore, it became one of the organic chemical contaminants polluting the marine environment around the world.

DEET was one of the highest detected PPCPs in South Florida's surface, USA, and Taiwan waters [6,7]. Furthermore, DEET has many adverse effects such as carcinogenic properties, seizures, skin irritation, and hypotension for human health [8]. In particular, it is hardly biodegraded for biorefractory, persistence, and ecotoxicological effects [9]. For this reason, DEET has been decomposed by some methods such as dielectric barrier discharge (DBD) plasma-ozonation [10] and advanced oxidation processes (AOPs) [11,12]. However, the ozone in DBD

plasma played a minor role in the plasma [13], and the AOPs have some disadvantages of high operation cost, low energy yield, and low degradation rate, respectively. Hence, an improved water treatment technique for the decomposition of DEET is very essential.

Water thermal plasma has received much attention in a view of the treatment of organic wastes. The water molecule offers higher plasma enthalpy and thermal conductivity than those of commonly used plasma gases such as N_2, O_2, and Ar as discussed in section 2.1. This is thus followed by higher heat transfer to the waste material for decomposition. Moreover, a large number of reactive radicals, such as ·H, ·O, and ·OH, as well as high temperatures were provided [14]. In particular, the radicals accelerate the chemical reactions, produce a large amount of syngas like H_2 and CO, and suppress byproduct formation.

In this study, the decomposition of DEET was investigated using DC water plasma with mist generation at atmosphere pressure under different three arc currents. The aims of this research were: (i) to analyze effluent gas and liquid quantitatively and qualitatively; (ii) to verify radical species from the water plasma; (iii) to identify intermediate products using the ESI-MS analytical method; (iv) finally to propose decomposition mechanism of DEET.

3.2 Thermodynamic Consideration

3.2.1 Method

Thermodynamic consideration has been attracting much attention in waste treatment and biomass gasification processes to better understand and design the decomposition process and the optimization of decomposition conditions [15,16]. There are two methods for modeling thermodynamic equilibrium: one is the stoichiometric method based on stoichiometric reactions, and the other one is the non-stoichiometric method based on the minimization of the total Gibbs

free energy in the system.

The non-stoichiometric thermodynamic equilibrium model has been widely applied in thermal plasma waste treatment process because thermal plasma is regarded as the plasma that is in or close to local thermodynamic equilibrium (LTE) [17]. In order to forecast and design the DEET decomposition process, thermodynamic equilibrium in various decomposition systems was calculated using FACT (Centre for Research in Computational Thermochemistry, Canada). FACT is a computer program, linked to a database, for finding the chemical equilibrium in gas mixtures by minimizing the Gibbs free energy. The calculations were performed using a software FactSage 7.2 (ThermFact Inc., Canada) in this study.

3.2.2 Result of Thermodynamic Calculation

Thermodynamic analysis for a mixture of DEET and water plasma was calculated to determine equilibrium compositions within the temperature range of 500–10,000 K with atmosphere pressure conditions. The equilibrium compositions of 2000 ppm DEET are presented in **Fig. 3.1**.

The DEET conversion was 100%, indicating that the possible products determined are molecules more thermodynamically stable than DEET, i.e., they show lower values of the Gibbs free energy. An increase in H_2, CO, H, O, and OH concentrations and a decrease of H_2O were shown with a gradual increase in temperature from 1700 K. As the temperature increased further over 3200 K, H_2O was fully dissociated into H and O atoms which suppress undesirable byproduct formation. Solid carbon was not included in the calculation. Instead, CO and CO_2 were formed by the reaction of carbon atoms in the DEET molecule with O radicals due to the oxidative environment. Moreover, N_2 gas was produced by fracture of the C–N bond.

3.3 Experimental

3.3.1 Experimental Setup

The water plasma system equipped with mist generator is shown in **Fig. 3.2**. The water plasma torch is a non-transferable DC arc type. The anode and cathode were coaxially designed, where the gap between electrodes was fixed to 2.0 mm for generating a steady-state plasma. The hafnium with 1.0 mm in diameter can prevent erosion of the cathode in an oxidative atmosphere. An ultrasonic generator embedded on the bottom of the torch generates an ultrasonic wave transmitted to the solution surface at a frequency of 2.5 MHz, by which an immediate mist is formed. Further descriptions of the torch can be found in section 2.2.1.

After arc ignition, the generated mist is directly supplied to the discharge area and subsequently heated and dissociated. Then, water plasma is discharged. Then, the mist is evaporated by the high heat flux of the arc discharge, and the produced hot gases can be rapidly quenched in the reaction tube and separated into the gaseous, liquid, and solid phases.

Experimental conditions for the decomposition of 2000 ppm DEET are shown in **Table 3.2**. The concentration of DEET solution was fixed at 2000 ppm in the whole experiment, and the volume of DEET solution was adjusted at 55 mL by a feed pump during all experiments. The power of the mist regulator was set at the one position of the maximum for mist generation. The torch was operated at an arc current of 6.0, 7.5, and 9.5 A corresponding to the discharge voltage from 146 to 178 V with an exit centerline plasma velocity from 5.6×10^2 to 7.6×10^2 m/s. Each run was operated for 10 min at room temperature and atmospheric pressure. Each experiment was performed at least three times for reproducibility.

3.3.2 Analytical Methods

3.3.2.1 Effluent Gas Analysis

The effluent gas during decomposition of 2000 ppm DEET was analyzed quantitatively and qualitatively. The quantitative analysis for the effluent gas was conducted by gas chromatography with a thermal conductivity detector (GC-TCD, GC- 14B, Shimadzu, Japan) and a Shincarbson ST 50/80 (6 m × 3.0 mm) packed column (Shinwa Chemical Industries Ltd, Japan). Individual gases (H_2, N_2, CO, and CO_2) with high purity (99.9%) purchased from GL sciences were used as standards. Pure Ar gas (> 99.999%) was used as the carrier gas. The measurement condition is shown in **Table 3.3**.

Hydrocarbon products were qualitatively identified using a quadrupole mass spectrometer (QMS, Ametek, Dycor Proline, USA) in combination with a Faraday detector. The measurement condition for QMS analysis is presented in **Table 3.4**. The effluent gases were directly introduced into the inlet hole of the QMS from the reaction tube where the gases were separated according to their mass/charge (*m/z*) ratio by electron impact ionization (EI). The ionization energy of 70 eV was applied for EI.

3.3.2.2 Effluent Liquid Analysis

The effluent liquid was analyzed by UV-visible (UV-Vis) spectrophotometer. The measurement condition is shown in **Table 3.5**. The UV-Vis absorption spectra for effluent liquid were monitored over wavelengths of 190–900 nm by UV-Vis spectrophotometer (V-550, Jasco, Japan). Each sample of 2.5 mL was prepared in a quartz tube and the absorbance changes were measured at 286 nm, which was performed following the establishment of standard curves using 500, 1000, 1500, 2000, 3000, and 4000 ppm DEET solutions as shown in **Fig. 3.3**.

The amount of carbon in the effluent liquid was tested with a total organic carbon analyzer (TOC-V CSN, Shimadzu, Japan) with a non-dispersive infrared (NDIR) detector. The detailed measurement condition is shown in **Table 3.6**.

Mass balance was calculated to obtain the generation rate of gas, liquid, and solid phases at different arc currents as follows:

$$F\ [\mathrm{mg/s}] = \frac{(M_0 + M_1) - (M_2 + M_3)}{t} = G_s + G_l + G_g \tag{3.1}$$

where F is the feed rate of the DEET solution (mg/s), M_0 and M_1 are the masses of raw 2000 ppm DEET solution before treatment in the beaker and torch (mg), respectively. M_2 and M_3 are the masses of remained liquid in the beaker and torch after treatment (mg), respectively. t is operation time (s). G_s, G_l, and G_g denote mass generating rates for solid, liquid, and gas as products (mg/s), respectively. Here, G_g was measured by a soap film flowmeter.

Furthermore, carbon balance was calculated based on GC results for the generated gas and TOC data for the liquid effluent to trace carbon from the feeding liquid to the products. The carbon balance can be expressed with the mass fraction of carbon (x_i) as follows:

$$Fx_f\ [\mathrm{mg/s}] = G_s x_s + G_l x_l + G_g x_g \tag{3.2}$$

where x_f is the carbon mass fraction of the feeding liquid. x_s, x_l, and x_g are the carbon mass fractions of the generating solid, liquid, and gas, respectively. x_f is determined by the concentration of the DEET solution, and x_l and x_g can be calculated from the measured TOC and GC data. Herein, x_s = 1 was used with the assumption of pure solid carbon product for carbon mass fraction in solid due to a negligible low amount.

Measurement of G_s and G_l is difficult because some solid carbon and liquid remaining on the cooling reaction tube could not be sampled completely after the decomposition experiment. Therefore, G_s and G_l were deduced from Eq. (3.2) as follows:

$$G_l\ [\mathrm{mg/s}] = \frac{F(1 - x_f) - G(1 - x_g)}{1 - x_l} \tag{3.3}$$

$$G_s\ [\mathrm{mg/s}] = F - G_g - \frac{F\left(1 - x_f\right) - G\left(1 - x_g\right)}{1 - x_l} \tag{3.4}$$

As a result, the generation rate and carbon balance were calculated by the above equations

and experimental results.

3.3.2.3 Decomposition Rate, Mineralization, and Energy Yield

The DEET decomposition and TOC reduction rates were calculated from analysis results as discussed in the previous section, respectively, as follows:

$$\text{DEET decomposition rate [\%]} = \frac{I_o - I}{I_o} \times 100 \tag{3.5}$$

where I_o and I are the measured peak intensities of DEET for the initial 2000 ppm DEET solution and for the effluent liquid, respectively.

$$\text{TOC reduction rate [\%]} = \frac{T_o - T}{T_o} \times 100 \tag{3.6}$$

where T_o and T are the TOC values for the initial 2000 ppm DEET solution and for the effluent liquid (ppm), respectively.

Furthermore, the energy yield for the water thermal plasma torch explained as the amount of DEET degraded per kWh of energy consumed was estimated as follows:

$$\text{Energy yield [g/kWh]} = \frac{(C_o - C) \times V}{P \times t \times 10^3} \tag{3.7}$$

where C_o and C are the initial and final concentration of the DEET (mg/L), V is the treated solution volume (L), P is the electrical power (kW), t is the reaction time (h) and the value of 1000 refers to the conversion factors from mg to g of the DEET concentration.

3.3.2.4 Intermediate Products Analysis

Intermediate products (IPs) generated during the decomposition of 2000 ppm DEET were determined via a high-resolution quadrupole time of flight mass spectrometer (QTOF, micrOTOF-Q III, Bruker, USA). The molecules in the liquid effluent were ionized by the electrospray ionization (ESI) method. This is called “soft” ionization due to it produces minimum fragments in the ionization process [18]. The *m/z* was scanned in a range of *m/z* 50–1000 in positive mode.

Measurement condition of QTOF is shown in **Table 3.7**. The solvent consisted of methanol and ultrapure water (50/50, v/v). Samples were injected at a flow rate of 1.0 mL/min by a syringe pump after adjusting the concentration of 10 ppm with a solvent. Electrospray conditions were the following: capillary, 4500 V; collision energy, 30 eV; nebulizer, 3 bar; N_2 drying gas, 8 L/min; dry gas temperature, 200℃. In addition, the calibration was performed using 5mM sodium formate (HCOONa) before analysis of effluent liquid as shown in **Fig. 3.4**.

3.3.2.5 Spectroscopic Diagnosis and Temperature Measurement

The spectroscopic diagnosis was conducted for the investigation of reactive species and temperature measurement as introduced in section 1.4.2.1. The reactive species from water thermal plasma discharge were determined using an optical emission spectrometer (OES, iHR550, HORIBA Jobin Yvon, Japan) as illustrated in **Fig. 3.5**. Also, the measurement condition of the optical emission spectrometer for detection of reactive species is shown in **Table 3.8**.

The emission spectra of plasma were collected to a charge-coupled device (CCD) through an optical fiber. The measurement point was kept at a point on the inner side of the nozzle exit. The excitation temperatures were calculated by the Boltzmann plot through H_α and H_β atom lines because the 2000 ppm DEET solution almost consists of water.

3.4 Results

3.4.1 Effect of Arc Current on *N, N*-diethyl-m-toluamide Decomposition

The generation rates in liquid, gas, and solid according to different arc currents are shown in **Fig. 3.6**, where the solid generation rate was calculated via mass balance and solid was estimated as 100% carbon [19]. The liquid and gas generation rates including the feed rate increased with

an increase of arc current. This results from an increase of total input energy, which is followed by larger Joule heating at a higher arc current. Here, Joule heating is defined as thermal energy generated when an electrical current travels through a resistive material. In this system, the current passes through the cathode rod in this system and the cathode rod is in contact with the solution. Therefore, the solution can be heated and evaporated in the plasma torch, thus accelerating the evaporation and dissociation of water molecules at a higher arc current. Finally, an enhanced radical reaction occurs, which increases the generation of effluent liquid and gas as well as the feed rate.

In contrast, the solid carbon generation showed a reduction, where mean generation solid rates were 42.3, 42.1, and 39.6 μg/s at the arc current of 6.0 A, 7.5 A, and 9.5 A, respectively. This is elucidated by higher gas generation through the reaction of promoted O radicals with carbon atoms from DEET molecules at a higher arc current.

3.4.2 Analysis of Effluent Gas

The mass spectra from QMS analysis were obtained from the effluent gas at various arc currents as shown in **Fig. 3.7**. H_2, C, CH_4, H_2O, N_2 or CO, and CO_2 were identified in all cases as indicated by 2 (H_2^+), 12 (C^+), 16 (CH_4^+), 18 (H_2O^+), 28 (N_2^+ or CO^+), and 44 (CO_2^+), respectively. Moreover, the peaks of 14 (CH_2^+), 29 (HCO^+), 30 (NO^+), and 45 ($HCOO^+$) corresponding to the CH_4, HCHO, NO, and HCOOH were identified as incomplete decomposed intermediates, where HCHO and HCOOH are considered as byproducts from the DEET decomposition [20]. The intensities of H_2 and CO_2 gradually increased, while incomplete decomposed intermediates decreased according to the increase of arc current. This is due to a stronger oxidation atmosphere at a higher arc current.

The quantitative effluent gas composition according to different arc currents is shown in **Fig. 3.8**. H_2 (45.3–55.5%), CO_2 (11.2–12.7%), CO (14.0–15.5%), and N_2 (17.8–27.9%) were obtained

as major gas products. Note that remarkable agreement between measured and equilibrium gas compositions was qualitatively achieved as final products as discussed in section 3.2.2, suggesting that the water plasma provides the environment close to thermodynamic equilibrium. The mole fractions of H_2 and CO_2 gradually increased as arc current increased, whereas those of CO and N_2 showed a decreasing tendency. This result is attributed to higher evaporation and dissociation of water molecules by larger Joule heating at an increased arc current as discussed in the previous section. Furthermore, the influence of the Joule heating is assumed to be larger under the condition of fixed solution volume during experiments in this study.

3.4.3 Analysis of Effluent Liquid

The effect of arc current on the carbon balance is depicted in **Fig. 3.9**. The carbon balance is a proportion of carbon amount for each phase (gas, liquid, and solid) to the total carbon amount in 2000 ppm DEET solution in unit time [19]. Carbon accounting for 35.3–38.1% of the 2000 ppm DEET solution was converted to the solid phase. The amounts of carbon decreased in both solid and liquid phases with the increase of arc current, indicating that a larger amount of DEET was decomposed. In contrast, carbon amounts increased in gas phases: CO and CO_2 gases. This is because of the large formation of O radicals from water molecules. This result is in accord with the TOC value which is discussed in the following paragraph.

UV–vis absorption spectra for 2000 ppm DEET solution and effluent liquid were monitored in **Fig. 3.10**. Compared to the 2000 ppm DEET solution, the peak of DEET at 286 nm was dramatically decreased after decomposition. Moreover, the intensity of the peak decreased with an increase of arc current, which indicates that a higher decomposition of DEET was achieved at a higher arc current. Note that the red-shifted peak at near 350 nm was detected in all three conditions. Recently, Homlok et al. [21] reported that radicals such as ·H and ·OH react with the

aromatic ring at the 300–340 nm range of wavelength. It has also been found that such a red-shifted peak appears when ·OH was an addition to the aromatic ring in the DEET molecule [22]. ·OH is also well known as an initial attack on the aromatic ring [23]. It is therefore expected that the peak near 350 nm is the hydroxylated intermediate compound formed during the DEET decomposition. Interestingly, the change tendency of this absorbance at 350 nm was similar to that of DEET at 286 nm with different currents, demonstrating that the decomposition of DEET further proceeded toward the next decomposition stage at a higher arc current.

The TOC reduction, DEET decomposition rate, and energy yield at various arc currents are presented in **Fig. 3.11**. To calculate energy yield, the mean arc voltage was also measured using an oscilloscope as shown in **Fig. 3.12**. The TOC reduction rate increased from 69.7% to 91.4% with the increase of arc current owing to the promoted formation of CO and CO_2 gases. The DEET decomposition rate shows as high as 86.7–94.8%. The highest decomposition rate was shown at the arc current of 9.5 A. This is attributed to high input energy as well as higher temperature, which then promotes more active chemical reactions by radicals. Consequently, this result evidently demonstrates that arc current may have a considerable impact on organic waste treatment.

3.4.4 Identification of Intermediate Products

Intermediate products (IPs) in the effluent liquid after decomposition were identified as shown in **Fig. 3.13**. The DEET molecule was not detected in all cases after decomposition compared to the 2000 ppm DEET solution, indicating that a high degree of decomposition was achieved as stated in the previous section. The ESI-MS spectra were mainly dominated by two main peaks, that is, *m/z* $[M + H]^+ = 128$ and *m/z* $[M + H]^+ = 227$, where the intensities were noticeably

changed according to the arc currents. It is demonstrated that the DEET was further decomposed to smaller IPs at a higher arc current.

3.4.5 Investigation of Reactive Species

Spectroscopic measurement was conducted to investigate not only excited species but also the decomposition mechanism as presented in **Fig. 3.14**. Excited species such as C (247.9 nm), OH (306.4 nm), Cu (318.5 nm), CH (388.8 nm), H_δ (408.2 nm), H_γ (434.0 nm), H_β (486.1 nm), and O (777.9 and 845 nm) were distinctly observed at nozzle exit during the decomposition of 2000 ppm DEET solution. The emission peaks of H, OH, and O was caused by the electron collision with H_2O molecules as well as the thermal dissociation of H_2O molecules in the plasma [24]. In particular, the emission intensities of H, OH, and O increased by the increase in arc current, proving that higher oxidative and/or reductive environments were achieved due to higher plasma temperatures. The peak of Cu was attributed to vaporization and erosion of the anode and cathode materials.

3.5 Discussion

3.5.1 Plasma Temperature Measurement

The plasma temperature was measured using the intensities of H_α and H_β atom lines by the Boltzmann plot method. The spectroscopic measurement result is shown in **Fig. 3.15**. Furthermore, as evidence for the DEET decomposition mechanism, the plasma temperature according to the arc currents was calculated as shown in **Fig. 3.16**. In the water plasma, three regions largely exist in sequence according to the temperature gradient from the cathode: (a) arc region, (b) plasma flame region, and (c) downstream region [25]. Herein, the plasma temperature measured in our study is expected to be highly close to that in the arc region. This is because the

measurement point is at a point on the inner side of the anode exit where anode arc attachment occurs as shown in **Fig. 3.5**.

The result showed that the plasma temperature increased with an increase of arc current in a range of 6700–8700 K. Therefore, we can conclude that the higher arc current in the water plasma undoubtedly has a decisive impact on facilitating the formation of larger reactive species and a higher decomposition rate. Based on the plasma temperature, the decomposition mechanism is deliberated in the next section. Meanwhile, the excitation temperature was lower than that of pure water because of decomposition energy for DEET. Despite being slightly decreased, the temperature is sufficiently high to decompose organic compounds [26].

3.5.2 Decomposition Mechanism of *N, N*-diethyl-m-toluamide

The ESI-MS result on the detected intermediates gives the identification of the possible 17 IPs from DEET molecule with different values of *m/z* summarized in **Table 3.9**. The proposed IPs include some molecules provided in the literature where ·OH or ·O was the main reactive source for DEET decomposition [20,22,27,28]. Taking into consideration the identified IPs formed through complicated chemical reactions along the three regions in the water plasma, a tentative decomposition mechanism is proposed in **Fig. 3.17** and discussed below.

Two of the IPs: IP 1-A, IP 1-B, and IP 2 may be formed through the arc region and plasma flame region, where electron dissociation and radical reaction are the main reactions. First, C–N bond fragmentation via electron impact occurs in the arc region due to high electron energy density in the arc column [29] and low bond energy, resulting in the loss of one ethyl group ($–CH_2CH_3$) bonded to the nitrogen atom. Subsequently, hydroxylation preferentially occurs for IP 1-A because ·OH has a high electrophilic characteristic and is one of the most powerful oxidizing radicals [30], which is followed by a reaction with ·O and ·H. However, the occurrence location of the hydroxylation on

the aromatic rings could not be decided for our analytical limitation. IP 3 and IP 4 are also generated from O oxidation and simultaneous dealkylation. On the other hand, IP 1-B as an isomer of IP 1-A would be produced with a ring-opening reaction by continuous ·OH attack. The 5 C in the DEET structure shown in **Table 3.1** has the largest negative charge (−0.78) which acts as the electron donation [21]. In addition, 5 C is the point with a relatively lower average local ionization energy (9.47 eV) compared to other bonds [31], by which the feeblish site can be predictable. Therefore, it is deduced that the ring opening potentially occurs by electrophilic ·OH.

IP 5 is derived from the hydroxylation of IP 1, which also has two isomers. IP 5-A is attributed to hydroxylation and further ring opening from IP 1-B. In the same way, IP 5-B including IP 8 can be generated from IP 1-A by hydroxylation and dealkylation. Herein, it should be noted that IP 1 and IP 5 were apparently an inverse proportionality as main intermediate products at different arc currents as mentioned in **Fig. 3.13.** The evidence suggests that ·OH reacted more actively with DEET molecules with an increase of arc current, which is followed by smaller molecules. Consequently, electron dissociation and hydroxylation are mainly responsible reactions, and hence IP 1 and IP 5 are believed to be key intermediates at the early stage of the DEET decomposition.

For the further reaction, IP 6 can be formed through the removal of the amine group due to the feeblish C–N bond, followed by oxygenation. IP 7 corresponding to pyruvic acid could be produced by the elimination of methyl group and additional hydroxylation as a short-chain saturated carboxylic acid product. In addition, IP 9 corresponding to *N, N*-diethyl-formamide could be formed from both IP 5-B and IP 8 through the elimination of the aliphatic chain. Since there are also lots of H radicals in the water plasma at the same time, the O atom in the C—O bond in IP 7 could react with H radical for dehydration and form IP 10. Consecutive dealkylation and hydroxylation of the IP 10 would lead to HCOOH and HCHO (namely, formic acid and

formaldehyde) mentioned in **Fig. 3.7**. Also, the dealkylation of IP 9 by H radical reaction could give IP 11. Finally, these molecules would go through further oxidation up to the final products (H_2O, H_2, N_2, CO_2, CO) in the downstream region.

The bonding between the aromatic ring and the methyl group would be easily attacked by radicals due to the relatively weak bond [10]. Therefore, the methyl was first hydroxylated into the alcohol group and subsequent oxidation led to IP 12. IP 13 could be also produced through more oxidation of the alcohol to the aldehyde group. Subsequently, IP 14 would be formed with evolution to aldehyde and loss of the diethylamine group. The detached diethylamine product may be further oxidized for the generation of N_2 gas. Thereafter, with the reduction of the aldehyde group by ·H in IP 14 for dehydration and H_2 generation, IP 14 also could result in the formation of IP 4. Then, these would be oxidized to form gases in the downstream region.

Recalling to **Fig. 3.13**, a fragment ion (*m/z* $[M]^+$ = 119) from the protonated DEET molecule was observed, which was from the loss of the diethylamine group. This may be attributed to the influence of energetic collisions at the collision cell in this work [32–34]. Therefore, some fragment ions could be also observed such as IP 15, IP 16, and IP 17 as shown in **Table 3.9**, which are particularly the same as products in the electron ionization mass spectrum of DEET [35].

3.6 Comparison of Experimental Results with Other Works

Table 3.10 shows some different processes for the treatment of DEET for the purpose of comparing performance assessment. Water plasma shows a higher percentage of degradation even at higher initial concentration and in shorter reaction time than other processes. Water plasma also has a higher energy yield without other additive chemicals. This result is ascribed to a one-step decomposition process and direct generation of radicals from the DEET solution.

3.7 Conclusion

The decomposition of a high concentration of *N, N*-diethyl-m-toluamide (DEET) was successfully achieved by water thermal plasma with mist generation at atmosphere pressure and a detailed decomposition mechanism of DEET was explained. The main remarks are drawn as follows.

The relationship between operational arc currents and DEET decomposition was discussed in detail. Major effluent gases were H_2, CO_2, CO, and N_2 and the contents of H_2 and CO_2 increased at a higher arc current due to an enhanced oxidative environment. The highest TOC reduction rate of 91.4% and decomposition rate of 94.8% were obtained at an arc current of 9.5 A with an energy yield of 0.3 g/ kWh within 10 min treatment.

A possible decomposition pathway was deduced based on the identification of intermediate products by optical emission spectroscopy (OES), UV–Visible (UV–Vis) spectroscopy, and quadrupole time of flight mass spectrometer (QTOF-MS). The H, O, and OH as reactive species generated by the dissociation of water molecules were verified, and the hydroxylated DEET was clearly observed in the UV–vis spectra. The ESI-MS results showed that seventeen main intermediates were identified, and the plasma temperatures were estimated at over 8000 K. Based on the intermediates and plasma temperature, the decomposition mechanism was proposed in detail. Electronic dissociation and hydroxylation were predominant factors for the ring opening at the early stage of decomposition. Afterward, O and H radicals were mainly proceeded for dealkylation and dehydration, respectively.

Based on our results, the water plasma with mist generation system could be a practical application for harmful wastewater treatment as well as syngas production.

References

[1] M. Chauhan, V.K. Saini, S. Suthar, Removal of pharmaceuticals and personal care products (PPCPs) from water by adsorption on aluminum pillared clay, Journal of Porous Materials (2019) 1–11.

[2] P. Westerhoff, Y. Yoon, S. Snyder, E. Wert, Fate of endocrine-disruptor, pharmaceutical, and personal care product chemicals during simulated drinking water treatment processes, Environmental Science & Technology 39(17) (2005) 6649–6663.

[3] L. Cizmas, V.K. Sharma, C.M. Gray, T.J. McDonald, Pharmaceuticals and personal care products in waters: occurrence, toxicity, and risk, Environmental Chemistry Letters 13(4) (2015) 381–394.

[4] M.K. Kajla, G.A. Barrett-Wilt, S.M. Paskewitz, Bacteria: A novel source for potent mosquito feeding-deterrents, Science Advances 5(1) (2019) eaau6141.

[5] P. Kain, S.M. Boyle, S.K. Tharadra, T. Guda, C. Pham, A. Dahanukar, A. Ray, Odour receptors and neurons for DEET and new insect repellents, Nature 502(7472) (2013) 507–512.

[6] C.-W. Pai, D. Leong, C.-Y. Chen, G.-S. Wang, Occurrences of pharmaceuticals and personal care products in the drinking water of Taiwan and their removal in conventional water treatment processes, Chemosphere 256 (2020) 127002.

[7] B. Ng, N. Quinete, S. Maldonado, K. Lugo, J. Purrinos, H. Briceño, P. Gardinali, Understanding the occurrence and distribution of emerging pollutants and endocrine disruptors in sensitive coastal South Florida Ecosystems, Science of The Total Environment 757 (2021) 143720.

[8] T. Osimitz, J. Murphy, L. Fell, B. Page, Adverse events associated with the use of insect repellents containing *N, N*-diethyl-m-toluamide (DEET), Regulatory Toxicology and Pharmacology 56(1) (2010) 93–99.

[9] S. Dey, F. Bano, A. Malik, Pharmaceuticals and personal care product (PPCP) contamination—a global discharge inventory, Pharmaceuticals and Personal Care Products: Waste Management and Treatment Technology (2019) 1–26.

[10] Z. Yu, Y. Sun, G. Zhang, C. Zhang, Degradation of DEET in aqueous solution by water falling film dielectric barrier discharge: effect of three operating modes and analysis of the mechanism and degradation pathway, Chemical Engineering Journal 317 (2017) 90–102.

[11] T. Zhu, J. Deng, M. Xu, A. Cai, C. Ye, J. Li, X. Li, Q. Li, DEET degradation in UV/monochloramine process: Kinetics, degradation pathway, toxicity and energy consumption analysis, Chemosphere 255 (2020) 126962.

[12] E. Aghdam, Y. Xiang, J. Sun, C. Shang, X. Yang, J. Fang, DBP formation from degradation of DEET and ibuprofen by UV/chlorine process and subsequent post-chlorination, Journal of Environmental Sciences 58 (2017) 146–154.

[13] M. Magureanu, C. Bradu, V. Parvulescu, Plasma processes for the treatment of water

contaminated with harmful organic compounds, Journal of Physics D: Applied Physics 51(31) (2018) 313002.

[14] T. Watanabe, H. Nishioka, Role of CH, CH_3, and OH radicals in organic compound decomposition by water plasmas, Plasma Chem. Plasma Process. 32(1) (2012) 123–140.

[15] A.B. Murphy, T. McAllister, Destruction of ozone-depleting substances in a thermal plasma reactor, Applied Physics Letters 73(4) (1998) 459–461.

[16] H.J. Huang, S. Ramaswamy, Modeling biomass gasification using thermodynamic equilibrium approach, Applied Biochemistry and Biotechnology 154(1-3) (2009) 14–25.

[17] A.B. Murphy, M. Tanaka, K. Yamamoto, S. Tashiro, T. Sato, J. Lowke, Modelling of thermal plasmas for arc welding: the role of the shielding gas properties and of metal vapour, Journal of Physics D: Applied Physics 42(19) (2009) 194006.

[18] T. Chen, Q. Yao, R.R. Nasaruddin, J. Xie, Electrospray Ionization Mass Spectrometry: A Powerful Platform for Noble-Metal Nanocluster Analysis, Angewandte Chemie International Edition 58(35) (2019) 11967–11977.

[19] S. Choi, T. Watanabe, Decomposition of water-insoluble organic waste by water plasma at atmospheric pressure, Journal of Physics: Conference Series (2012) 012003.

[20] E. Mena, A. Rey, E.M. Rodríguez, F.J. Beltrán, Reaction mechanism and kinetics of DEET visible light assisted photocatalytic ozonation with WO_3 catalyst, Applied Catalysis B: Environmental 202 (2017) 460–472.

[21] R. Homlok, V. Mile, E. Takács, G. Járvás, S. Góger, L. Wojnárovits, Comparison of hydrogen atom and hydroxyl radical reactions with simple aromatic molecules in aqueous solution, Chemical Physics 534 (2020) 110754.

[22] W. Song, W.J. Cooper, B.M. Peake, S.P. Mezyk, M.G. Nickelsen, K.E. O'Shea, Free-radical-induced oxidative and reductive degradation of *N, N′*-diethyl-m-toluamide (DEET): Kinetic studies and degradation pathway, Water Research 43(3) (2009) 635–642.

[23] M. Antonopoulou, A. Giannakas, Y. Deligiannakis, I. Konstantinou, Kinetic and mechanistic investigation of photocatalytic degradation of the *N, N*-diethyl-m-toluamide, Chemical Engineering Journal 231 (2013) 314–325.

[24] P. Bruggeman, D.C. Schram, On OH production in water containing atmospheric pressure plasmas, Plasma Sources Science and Technology 19(4) (2010).

[25] Y.M. Narengerile, T. Watanabe, Decomposition mechanism of phenol in water plasmas by DC discharge at atmospheric pressure, Chemical Engineering Journal 168(3) (2011) 985–993.

[26] Y. Ozeki, T. Matsuo, M. Tanaka, T. Watanabe, Characteristics of water thermal plasma for biomass utilization system, Journal of Fluid Science and Technology 12(3) (2017) JFST0022.

[27] C. Medana, P. Calza, F. Dal Bello, E. Raso, C. Minero, C. Baiocchi, Multiple unknown

degradants generated from the insect repellent DEET by photoinduced processes on TiO_2, Journal of Mass Spectrometry 46(1) (2011) 24–40.

[28] B. Ye, X.-Y. Zhang, T. He, W.-L. Wang, H.-J. Wu, Y. Lu, Q.-Y. Wu, H.-Y. Hu, Ammonia/chlorine synergistic oxidation process applied to the removal of *N, N*-diethyl-3-toluamide, Chemical Engineering Journal 380 (2020) 122409.

[29] S. Safa, G. Soucy, Liquid and solution treatment by thermal plasma: a review, International Journal of Environmental Science and Technology 11(4) (2013) 1165–1188.

[30] D. Cui, A.M. Mebel, L.E. Arroyo-Mora, C. Zhao, A. De Caprio, K. O'Shea, Fundamental study of the ultrasonic induced degradation of the popular antihistamine, diphenhydramine (DPH), Water Research 144 (2018) 265–273.

[31] A. Cai, J. Deng, C. Ye, T. Zhu, X. Ling, S. Shen, H. Guo, X. Li, Highly efficient removal of DEET by UV-LED irradiation in the presence of iron-containing coagulant, Chemosphere 286 (2022) 131613.

[32] G.J. Van Berkel, S.A. McLuckey, G.L. Glish, Electrochemical origin of radical cations observed in electrospray ionization mass spectra, Analytical Chemistry 64(14) (1992) 1586–1593.

[33] G.J. Van Berkel, S.A. McLuckey, G.L. Glish, Electrospray ionization of porphyrins using a quadrupole ion trap for mass analysis, Analytical Chemistry 63(11) (1991) 1098–1109.

[34] M. Schäfer, M. Drayß, A. Springer, P. Zacharias, K. Meerholz, Radical cations in electrospray mass spectrometry: formation of open-shell species, examination of the fragmentation behaviour in ESI-MSn and reaction mechanism studies by detection of transient radical cations, European Journal of Organic Chemistry 2007(31) (2007) 5162–5174.

[35] National Institute of Standards and Technology (NIST). (https://webbook.nist.gov/chemistry).

Table 3.1. Physicochemical properties of DEET.

Molecular Structure	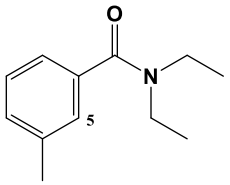
Molecular Formula	$C_{12}H_{17}NO$
Chemical Name	*N*, *N*-diethyl-m-toluamide
Molecular Weight [g/mol]	191.274
Wavelength of Maximum Absorbance [nm]	286
Melting Point [℃]	-33
Boiling Point [℃]	288–292
Specific Gravity [-]	0.999
Water Solubility at 25 ℃ [mg/L]	912

Table 3.2. Experimental conditions for the decomposition of DEET.

Pressure [kPa]	101.3 (Atmosphere Pressure)
Temperature [℃]	25
Arc Current [A]	6.0, 7.5, 9.5
Mean Arc Voltage [V]	146 –178
Plasma Supporting Gas	Water, DEET
DEET Solution Concentration [ppm]	2000

Table 3.3. Measurement conditions of gas chromatograph for effluent gas analysis.

Equipment		GC-14B (Shimadzu, Japan)
Detector		Thermal Conductivity Detector (TCD)
Column	Inner Diameter [mm]	3.0
	Length [m]	6.0
	Column	Packed Column-Shincarbon ST
Carrier Gas		Argon (99.9%)
Pressure of Carrier Gas [kPa]		700
Column Temperature [℃]		160
Injection Temperature [℃]		200
Detector Temperature [℃]		220
TCD Current [mA]		50
Injection Gas Volume [mL]		0.6

Table 3.4. Measurement conditions of quadrupole mass spectrometer for effluent gas analysis.

Equipment	DyCor ProLine (Ametek, USA)
Mass Analyzer	Quadrupole Analyzer
Detector	Faraday Detector
Inlet Heater Temperature [℃]	80
Pressure in Chamber [Torr]	5×10^{-6}
Ionization Source	Electron Impact
Ionization Energy [eV]	70

Table 3.5 Measurement conditions of UV-vis spectrometer for effluent liquid analysis.

Equipment	V-550 Spectrophotometer (Jasco, Japan)
Cuvette	Quartz Tube
Sample Volume [mL]	2.5
Detection Range [nm]	190–900
Absorbance Wavelength of DEET [nm]	286

Table 3.6. Measurement conditions of total organic carbon for effluent liquid analysis.

Equipment	TOC-L (Shimadzu, Japan)
Carrier gas	Air (99.9%)
Flow Rate of Carrier Gas [mL/min]	150
Combustion Temperature [℃]	680
Dehumidifier Temperature [℃]	0.6
Detect Method	NDIR (Non-dispersive infrared detector)
Injection Volume [μL]	150
Injection Time [-]	3

Table 3.7. Measurement conditions of quadrupole time of flight mass spectrometer for intermediate products analysis.

Equipment	micrOTOF-Q III (Bruker Daltonics, USA)
m/z scan range [-]	50–1000
Solvent (v/v)	Methanol : H_2O = 50 : 50
Sample Concentration with Solvent [ppm]	10
Flow Rate of Sample [mL/min]	1
Capillary [V]	4500
Nebulizer [bar]	3
Flow Rate of Dry Gas [L/min]	8 (N_2)
Dry Gas Temperature [°C]	200
Collision Energy [eV]	30

Table 3.8. Measurement conditions of optical emission spectrometer for detection of reactive species.

Equipment	iHR550 (Horiba Jobin Yvon, France)
Detector	Charge-Coupled Device (CCD) (1024×256)
Exposure Time [s]	0.02
Entrance Slit [mm]	0.03
Grating [gr/mm]	150
Distance between Plasma and Lens [cm]	45

Table 3.9. Intermediate products identified by QTOF-MS.

Products	Molecular Formula	Proposed Structure	Molecular ions (*m/z*) $[M + H]^+$
DEET	$C_{10}H_{17}NO$	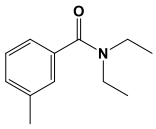	192.1392
IP 1-A	$C_{11}H_{17}NO_4$	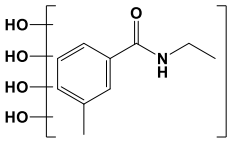	227.1252
IP 1-B	$C_{10}H_{13}NO_5$	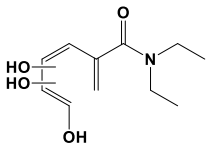	227.1252
IP 2	$C_9H_{11}NO$	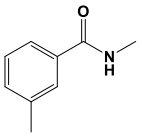	150.9773
IP 3	$C_8H_8O_2$	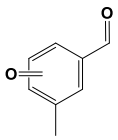	135.0037
IP 4	C_7H_8O	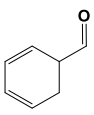	109.0979
IP 5-A	$C_7H_{13}NO$	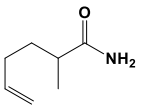	128.9541
IP 5-B	$C_7H_{13}NO$	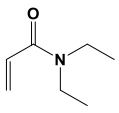	128.9541
IP 6	$C_4H_6O_2$	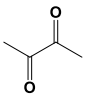	87.0455
IP 7	$C_3H_4O_3$	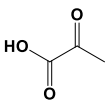	88.979

IP 8	$C_7H_{13}NO_2$	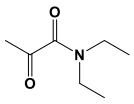	144.9273
IP 9	$C_5H_{11}NO$	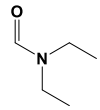	102.0915
IP 10	C_4H_4O		69.07
IP 11	C_4H_9NO	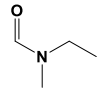	87.982
IP 12	$C_{12}H_{17}NO_3$	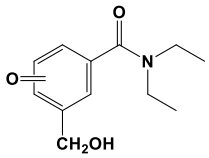	222.908
IP 13	$C_{12}H_{15}NO_4$	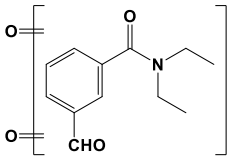	234.9174
IP 14	$C_8H_6O_3$	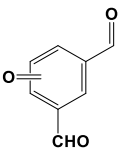	149.0222
IP 15	C_8H_7O	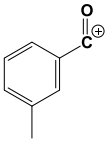	119.0598 $[M]^+$
IP 16	C_7H_7	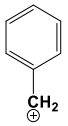	91.0547 $[M]^+$
IP 17	C_5H_5		65.0381 $[M]^+$

Table 3.10. Comparison of the performance of DEET decomposition with other processes.

Process	Initial concentration (ppm)	Tr (min)	Decomposition rate (%)	Additive chemicals	Energy yield (g/kWh)	Ref.
Water plasma	2000	10	94.8	None	0.3	This study
DBD	20	27	76.8	O_3	0.27	[10]
AOPs	0.5	60	75.4	NH_2Cl	0.0005	[11]
AOPs	0.2	20	90	Cl	0.013	[12]

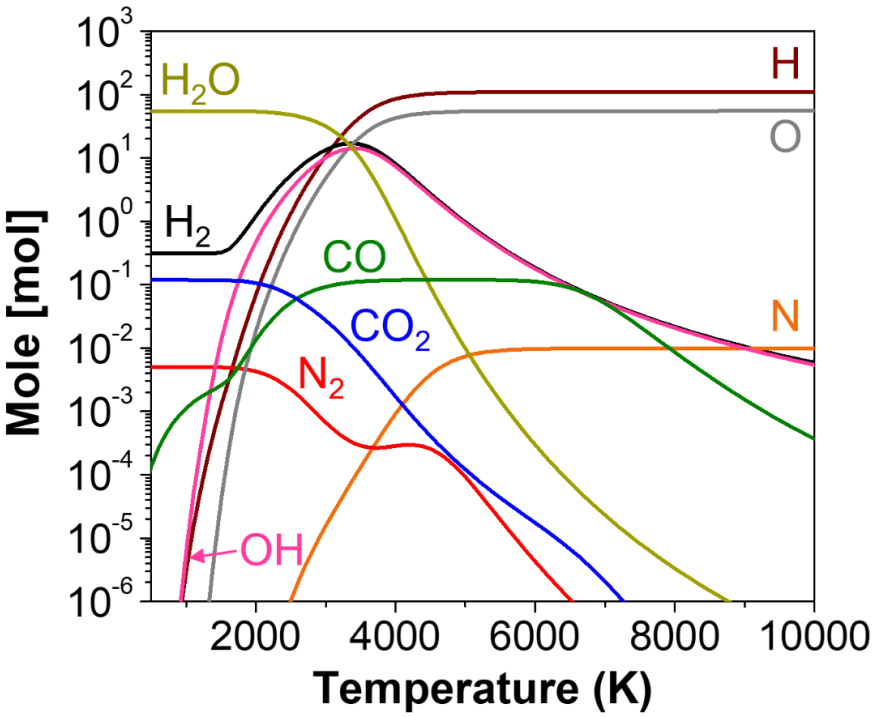

Fig. 3.1. Thermodynamic equilibrium composition of 2000 ppm DEET.

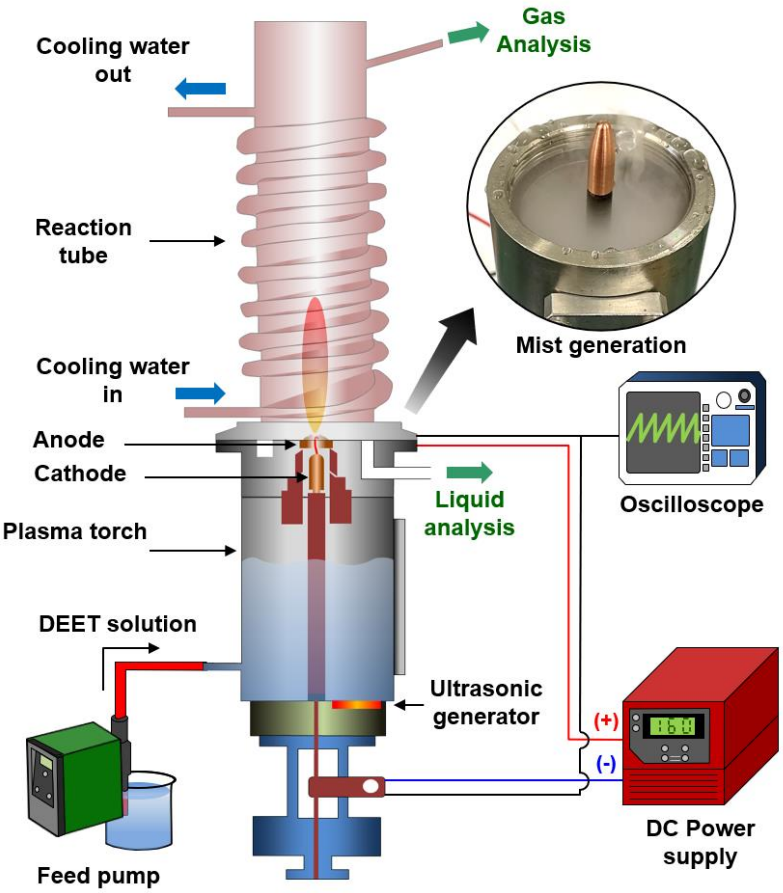

Fig. 3.2. Schematic diagram of water plasma system with mist generation for DEET decomposition.

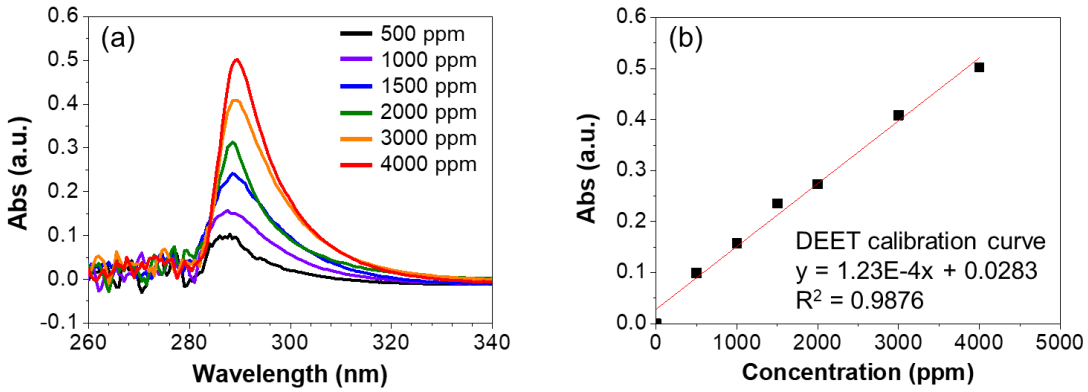

Fig. 3.3. (a) UV-vis spectra of various concentrated DEET solution and (b) the calibration curve.

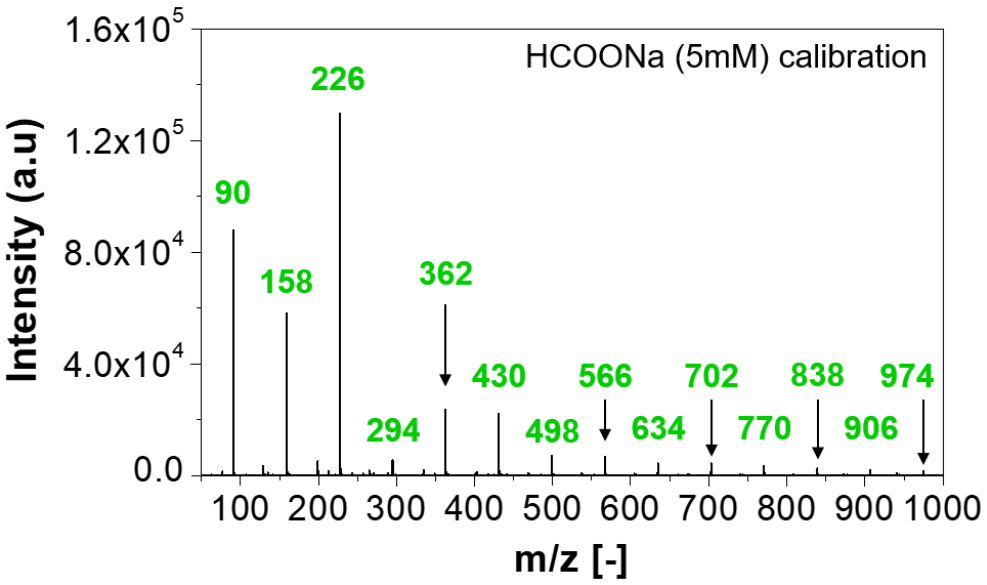

Fig. 3.4. The result of calibration of quadrupole time of flight mass spectrometer using 5mM HCOONa solution.

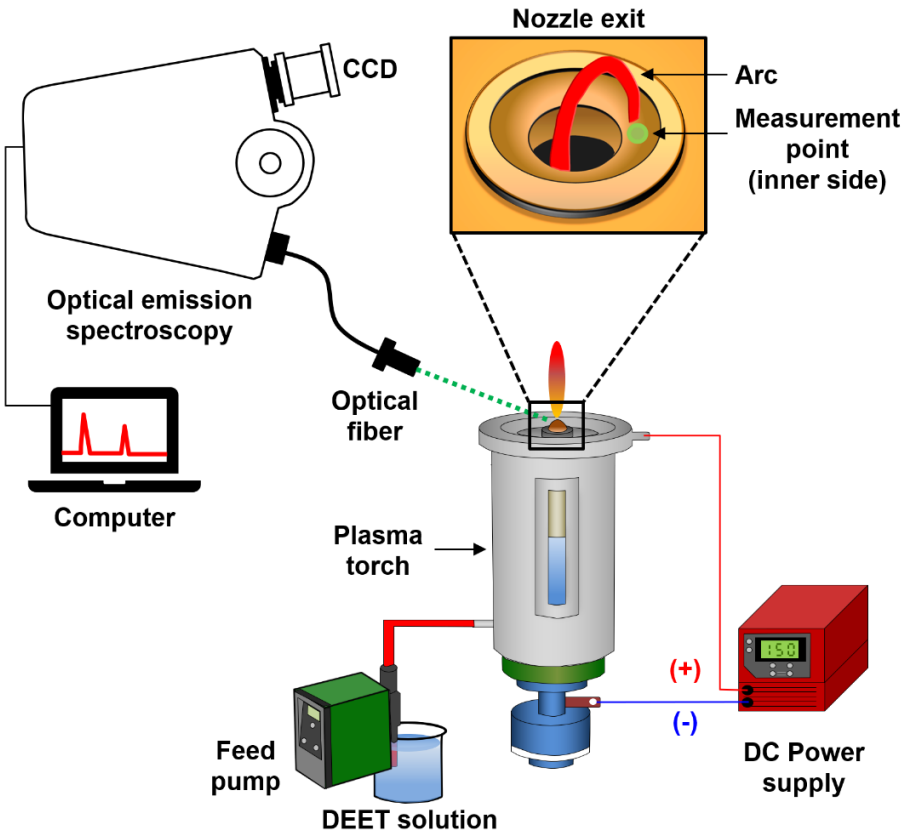

Fig. 3.5. Illustration of measurement system for optical emission spectra.

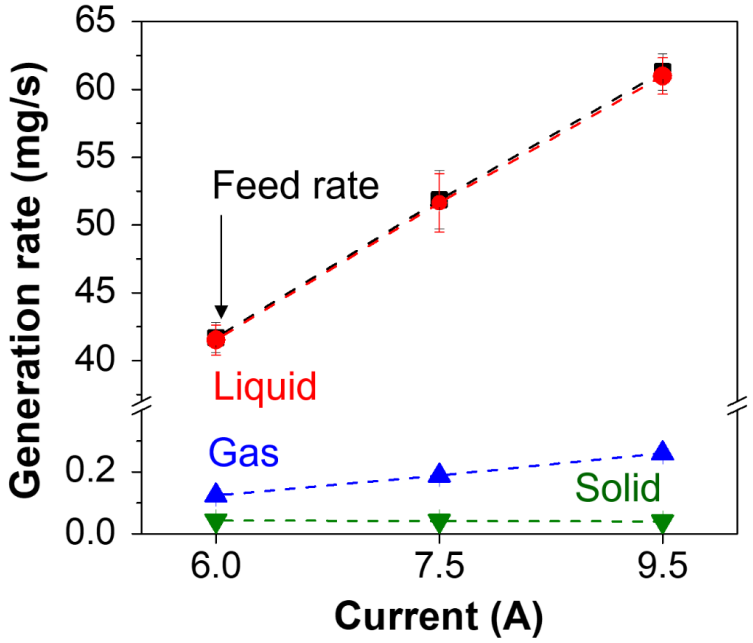

Fig. 3.6. Generation rates of liquid, gas, and solid during the decomposition of 2000 ppm DEET at different arc currents.

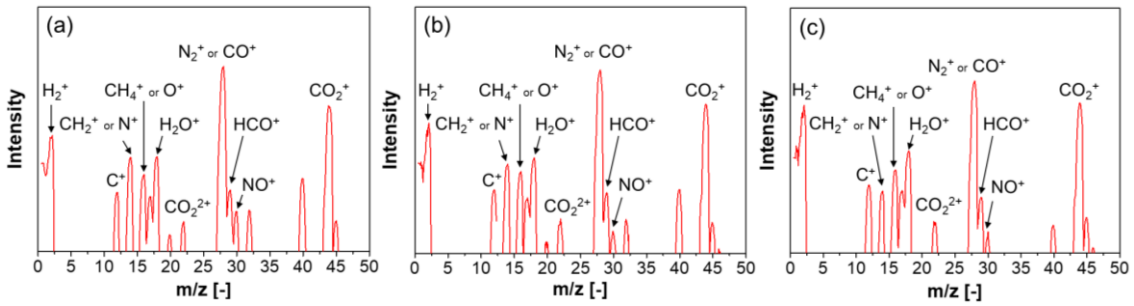

Fig. 3.7. Mass spectra of effluent gas generated during decomposition of 2000 ppm DEET at arc current of (a) 6.0 A, (b) 7.5 A, and (c) 9.5 A

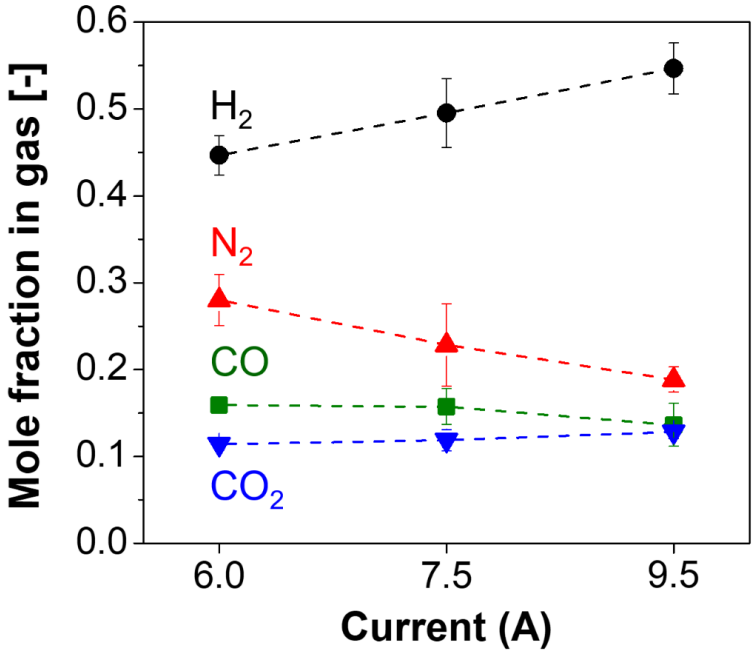

Fig. 3.8. Gas composition generated from 2000 ppm DEET decomposition at various arc currents.

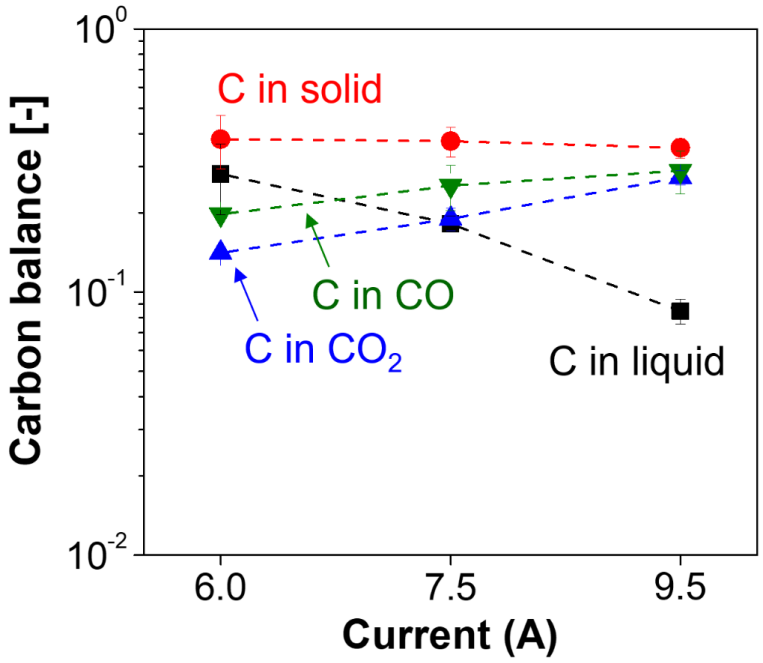

Fig. 3.9. Carbon balance calculated from each phase after decomposition of 2000 ppm DEET.

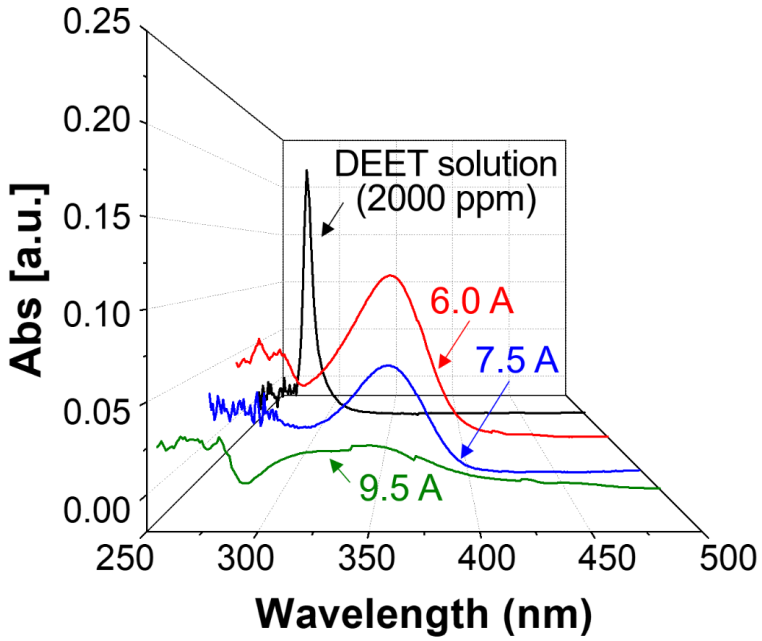

Fig. 3.10. UV–vis absorption spectra of the 2000 ppm DEET and effluent liquid at different arc currents

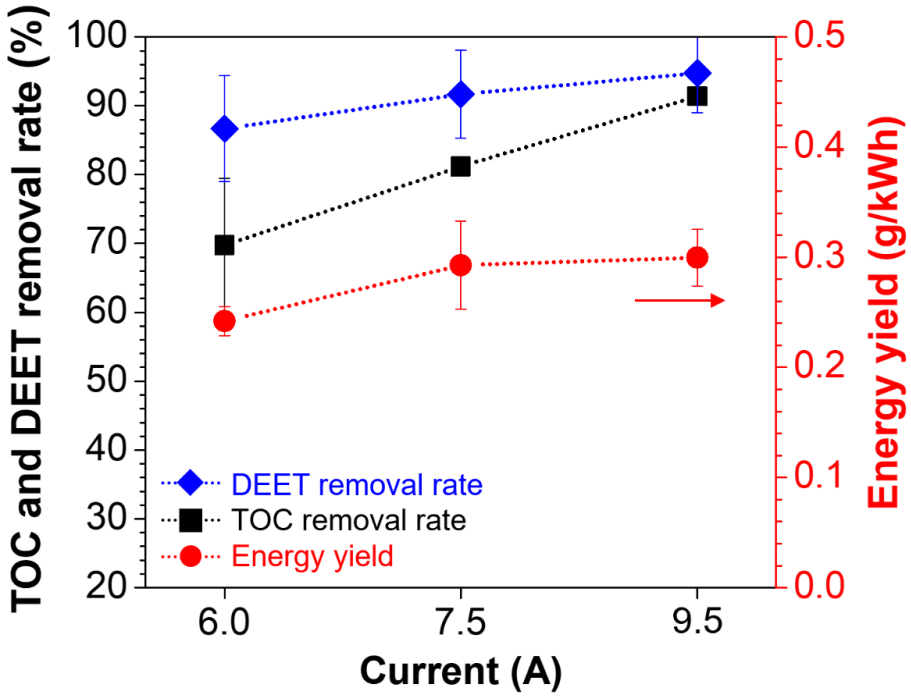

Fig. 3.11. Effect of arc current on TOC and DEET removal rates and energy yield.

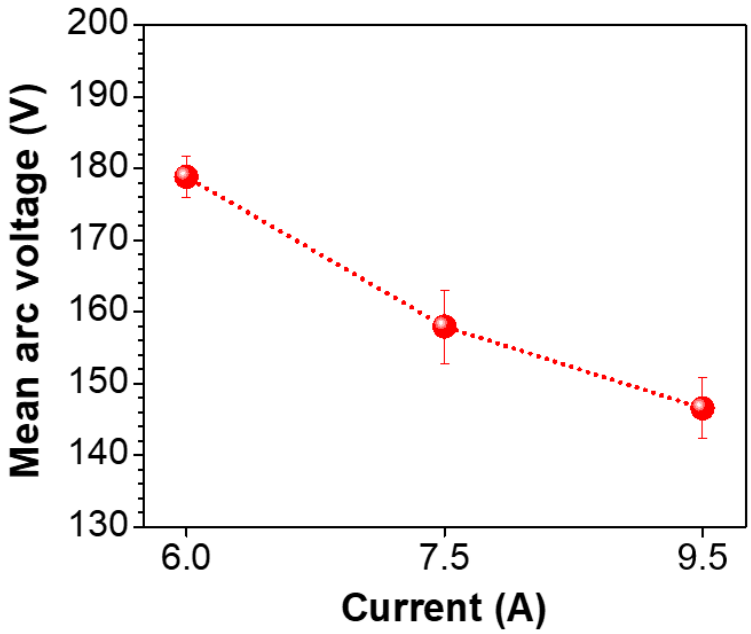

Fig. 3.12. Mean arc voltage at different arc currents

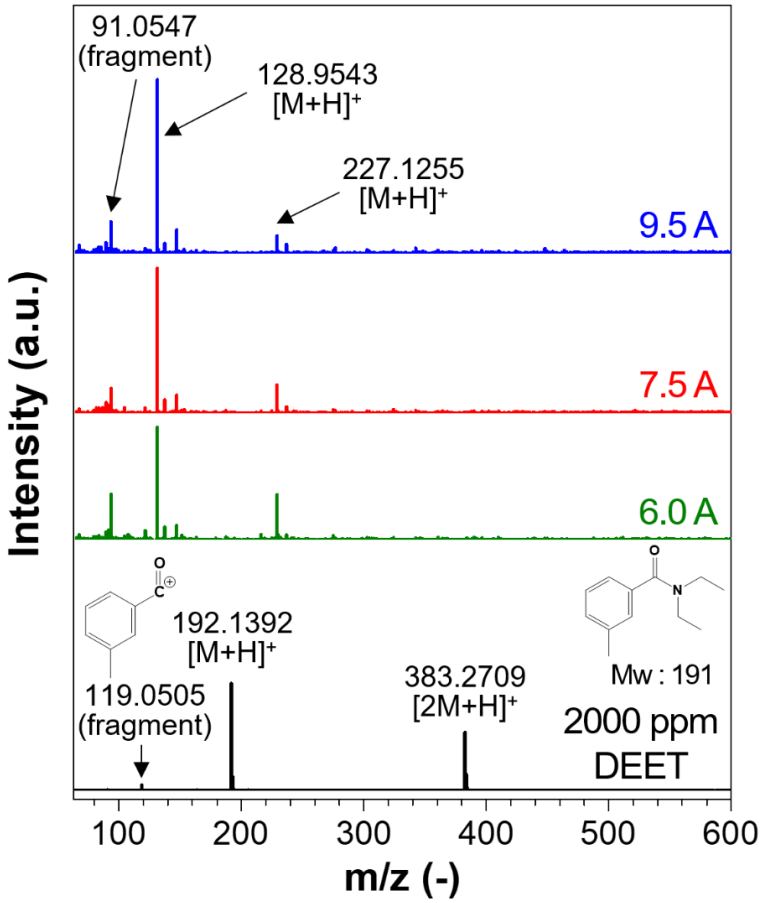

Fig. 3.13. ESI-MS spectra in the positive mode for effluent liquid at different currents.

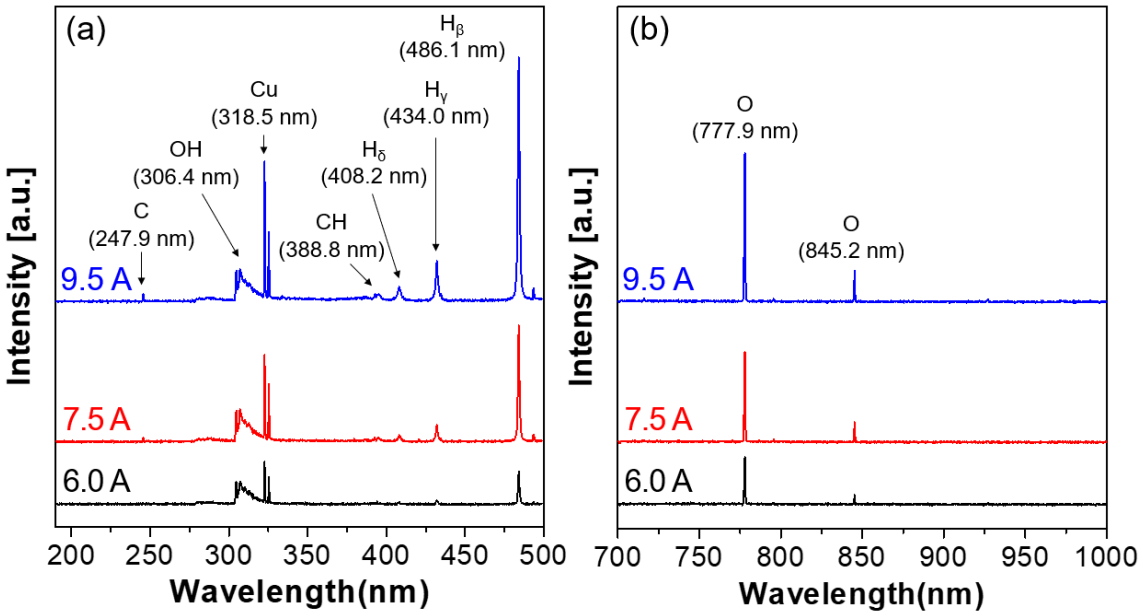

Fig. 3.14. Excited species of (a) H, OH, and (b) O detected during the decomposition of 2000 ppm DEET.

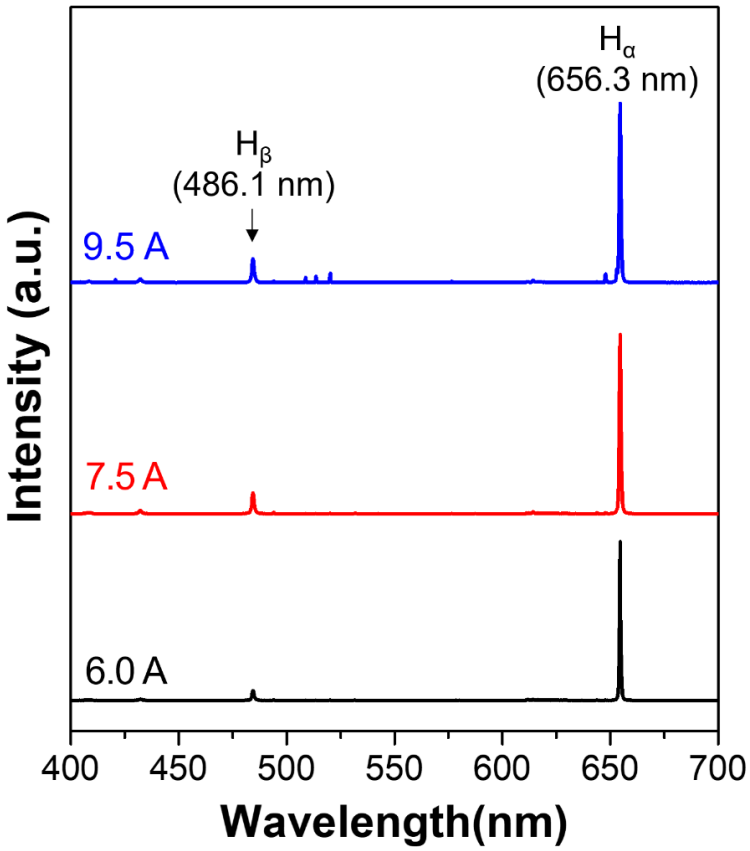

Fig. 3.15. Excited species of H_α and H_β at different arc currents during the decomposition of 2000 ppm DEET.

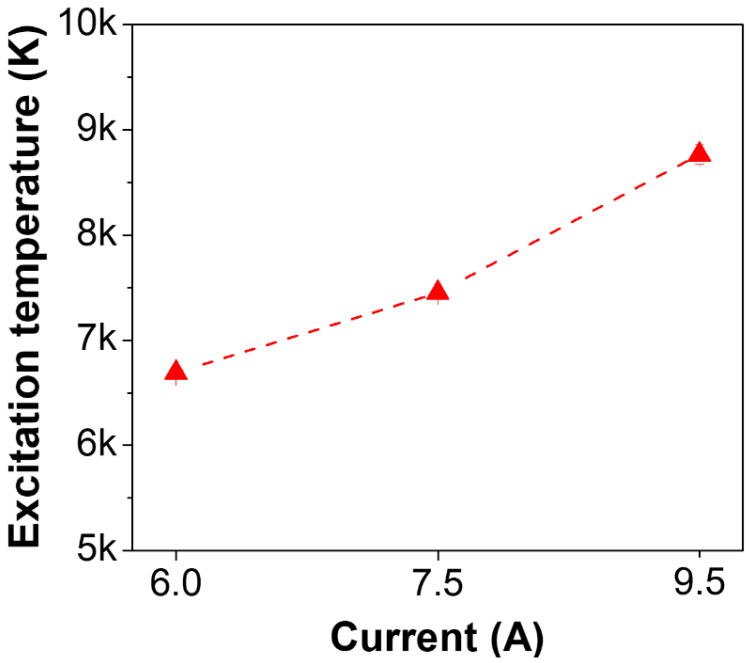

Fig. 3.16. Plasma temperature at exit nozzle at different arc currents.

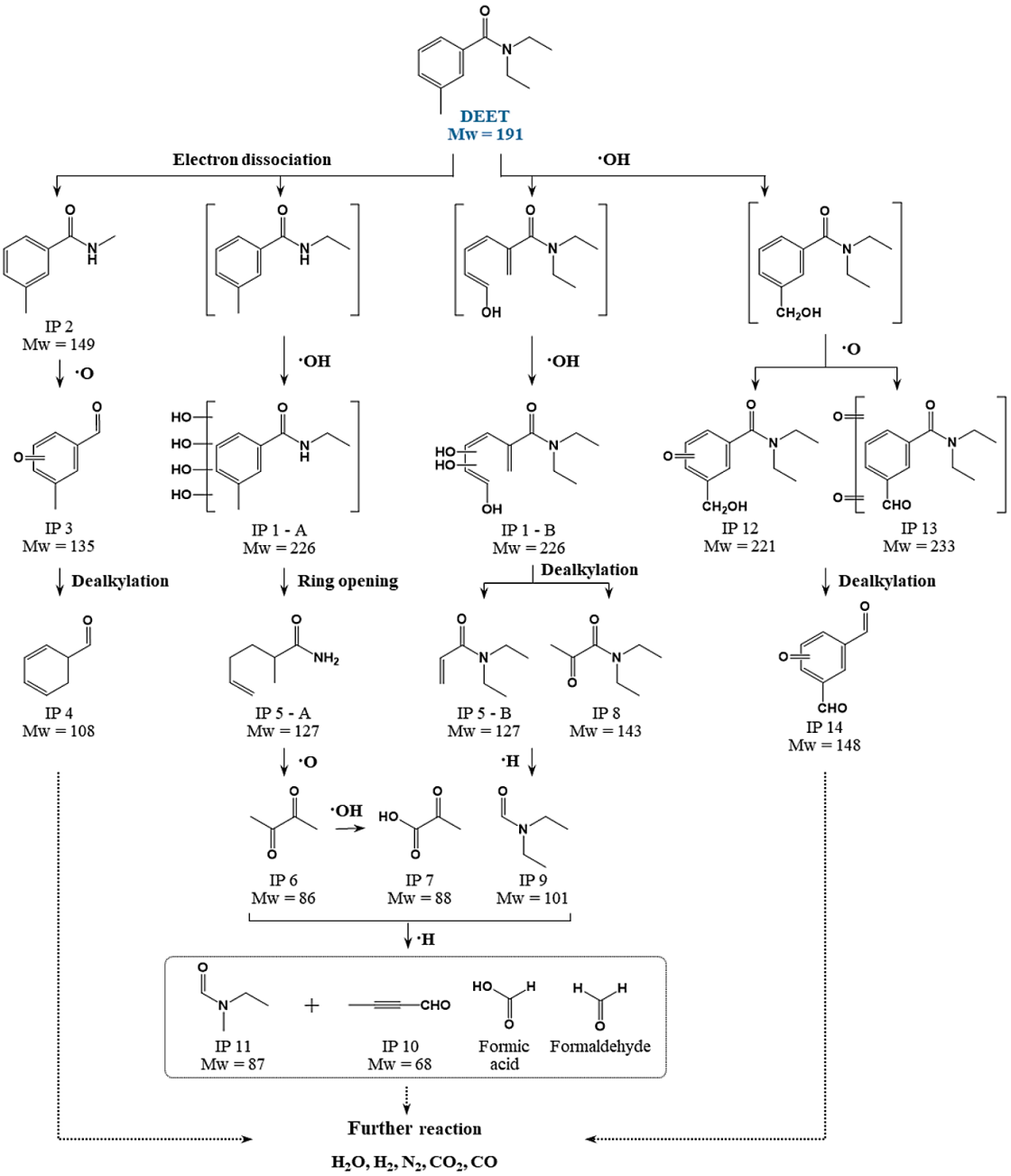

Fig. 3.17. Proposed DEET decomposition mechanism.

4. Decomposition of Caffeine by Water Plasma

4.1 Introduction

Emerging contaminants (ECs) are widely detected and ubiquitous in environments around the world, which include a wide range of natural and chemical compounds, such as pharmaceuticals and personal care products (PPCPs), endocrine-disrupting chemicals (EDCs), hormones, food additives, and surfactants [1,2]. The extent of ECs is currently larger and expanding with the introduction of new chemicals [3].

Of all the ECs, Caffeine (CAF) is the most widely used psychoactive legal drug worldwide and has been regarded as the first frequently consumed drug worldwide [4,5]. The physicochemical property of CAF is shown in **Table 4.1**. CAF is also in many consumed beverages and foods such as tea, energetic drinks, chocolate, and especially coffee in our daily life [6,7]. Moreover, the average CAF consumption reaches about 70 mg/person in a day worldwide [8]

CAF however has been highly detected in the environment through the residues of consumed caffeine, disposal into the sink, excretion via urine, and inappropriate treatment of expired CAF-containing drugs in households and hospitals [9]. For this reason, CAF was the highest concentration in the seawater of other countries such as the USA, Australia, Portugal, Japan, and China, with concentrations ranging from 3 to 11 mg/L. Therefore, CAF was adopted as a chemical marker for wastewater.

CAF has also a negative impact on the environment and human health. Aquatic organisms in the environment are disturbed due to its toxicity, bioaccumulation, high solubility, and low octanol-water partition coefficient [10,11]. Simultaneously, it poses serious health risks in humans such as osteoporosis, cardiac arrhythmia, muscular instability, and the causation of

various cancers [12,13]. Thus, it is necessary to seek another effective approach for CAF treatment due to its extensive consumption, and conventional low-grade sewerage infrastructure and sewage treatment [14].

Water plasma has been considered as one of the most promising waste treatments as discussed previous chapter. First and foremost is that the water molecule allows higher plasma enthalpy and thermal conductivity than those of general plasma gases such as Ar, N_2, and O_2, which is hence followed by higher heat transfer into the treated wastes [15]. Secondly, a considerable quantity of highly reactive radicals such as H, O, and OH generated by high temperature catalyze various homogeneous and heterogeneous chemical reactions.

Herein, the decomposition of CAF using the DC water plasma with mist generation was experimentally investigated. The experiments were conducted under different three arc currents at the constant CAF concentration. The effluent gas and liquid were analyzed quantitatively and qualitatively. Moreover, radical species generated from the water plasma were verified, including measurement of plasma temperature. Additionally, intermediate products were identified by electrospray ionization-mass spectroscopy (ESI-MS) and finally, the decomposition pathway was proposed.

4.2 Thermodynamic Consideration

The thermodynamic calculation method can be found in **Chapter 3**. Thermodynamic analysis for a mixture of CAF and water plasma was calculated to determine equilibrium compositions within the temperature range of 1000–9000 K with atmosphere pressure conditions. The equilibrium compositions of 20 g/L CAF are presented in **Fig. 4.1.** The CAF conversion was 100%, indicating that the possible products determined are molecules more thermodynamically stable than CAF, i.e., they show lower values of the Gibbs free energy. An increase of

concentrations in H_2, CO, H, O, NO, and OH were observed from 1700 K with thermal dissociation of water molecules. At over 3000 K, H_2O was fully dissociated into H and O atoms. Also, a significant quantity of OH radicals was produced in a range of 2000–4000 K, with the peak concentration at 3500 K. H_2 was produced by high degree of dissociation of H_2O and rapid quenching rate, and CO and CO_2 were formed by the reaction of carbon atoms in the CAF molecule with O radicals due to the oxidative environment. Moreover, N_2 gas was produced by fracture of the C–N bond. Particularly, many kinds of nitrogenous compounds such as NH, NH_2, NO, and NO_2 with low concentrations were also produced, which is assumed to be a high concentration of nitrogen in the CAF molecule and complex reactions with radicals.

4.3 Experimental

4.3.1 Experimental Setup

The water plasma system equipped with mist generation for decomposition of 20 g/L CAF solution. A detailed description about experimental apparatus can be found in **Chapters 3**.

Experimental conditions for the decomposition of 20 g/L CAF are shown in **Table 4.2**. The concentration of CAF solution was fixed at 20 g/L in the whole experiments, and the volume of CAF solution was adjusted at 55 mL by feed pump during all experiments. The power of the mist regulator was set at the one position of the maximum for mist generation. The torch was operated at an arc current of 6.0 A, 7.5 A, and 9.5 A corresponding to the discharge voltage from 119 to 137 V. Each run was operated for 10 min at room temperature and atmospheric pressure. Each experiment was performed at least three times for reproducibility.

4.3.2 Analytical Methods

4.3.2.1 Effluent Gas Analysis

The effluent gas generated during the decomposition of 20 g/L CAF solution was quantitatively analyzed by gas chromatography with a thermal conductivity detector (GC-TCD, GC-14B, Shimadzu, Japan) and a Shincarbson ST 50/80 (6 m × 3.0 mm) packed column (Shinwa Chemical Industries Ltd, Japan). Pure Ar gas (> 99.999%) was used as the carrier gas.

4.3.2.2 Effluent Liquid Analysis

The concentration of CAF after decomposition was determined by high-performance liquid chromatography (HPLC, V-550, Jasco, Japan) at a wavelength of 294 nm with a UV detector (UV-975) and an Inertsil ODS-3V (C18) (250 mm × 4.6 mm, 5 μm) column. The mobile phase was acetonitrile and ultrapure water (75:25, v/v) at 40 ℃ with a flow rate of 0.8 mL/min. The detailed analysis condition for HPLC is shown in **Table 4.3**, and the result of the calibration curve with various concentrated CAF solutions is indicated in **Fig. 4.2**. The mineralization was measured using a total carbon organic analyzer (TOC-L, Shimadzu, Japan) with the measurement condition as shown in **Table 4.4**.

The quantification of ammonium ion (NH_4^+) and nitrite (NO_2^-) in the effluent liquid was conducted by the well-known colorimetric assays: Nessler's and Griess reagent methods, respectively, using UV-vis spectrometer (V-550, Jasco, Japan). NH_4^+ analysis was determined via a mixture of Nessler's reagent and 500 g/L potassium sodium tartrate tetrahydrate with the measurement at 420 nm. The principle of Nessler reaction and calibration curve with various concentrated CAF solutions were shown in **Fig. 4.3** and **Fig. 4.4**, respectively. NO_2^- was estimated by Griess reagent (1:1 of 1% sulfanilamide in 5% phosphoric acid and 0.1% *N*-1-naphthylethylenediamine dihydrochloride in 5% phosphoric acid) of which the absorbance was acquired at 540 nm. Nitrate (NO_3^-) was then determined by using HPLC at 210 nm. The principle

of Griess reaction and calibration curve with various concentrated CAF solutions for NO_2^- detection were shown in **Fig. 4.5** and **Fig. 4.6**, respectively. The calibration curve for NO_3^- is also shown in **Fig. 4.7**. Every analysis of the above was performed using ammonium sulfate, sodium nitrite, and nitrate solutions, respectively.

4.3.2.3 Decomposition Rate, Mineralization, and Energy Yield

The decomposition rate and mineralization of CAF after decomposition was determined by HPLC and TOC as follows:

$$\text{CAF decomposition rate [\%]} = \frac{C_o - C}{C_o} \times 100 \tag{4.1}$$

$$\text{TOC reduction rate [\%]} = \frac{T_o - T}{T_o} \times 100 \tag{4.2}$$

where C_o is the initial concentration of CAF solution (g/L), C is the CAF concentration in the effluent liquid (g/L), T_o is the initial TOC value of CAF solution (ppm), T is the TOC value for the effluent liquid (ppm).

The energy yield for the water thermal plasma torch explained as the amount of CAF degraded per kWh of energy consumed was estimated according to the following equation:

$$\text{Energy yield [g/kWh]} = \frac{(C_o - C) \times V}{P \times t} \tag{4.3}$$

where C_o and C are the initial and final concentration of the CAF (g/L), V is the treated solution volume (L), P is the electrical power (kW), t is the reaction time (h).

4.3.2.4 Intermediate Products Analysis

Intermediate products (IPs) formed in CAF decomposition were identified using a high-resolution quadrupole time of flight mass spectrometer (QTOF-MS, micrOTOF-Q III, Bruker, USA). The spectra were obtained in the positive ion mode by electrospray ionization (ESI) and

the *m/z* range was from 50 to 1000. Electrospray conditions are indicated in **Table 4.5**. The eluent consisted of methanol and ultrapure water (50/50, v/v) and the flow rate was 1.0 mL/min.

4.3.2.5 Spectroscopic Diagnosis and Temperature Measurement

Optical emission spectra (OES) were measured to identify the excited species in the gas phase during water plasma discharge using an optical emission spectrometer (iHR550, HORIBA Jobin Yvon, Japan). The optical fiber was fixed to the nozzle exit and 45 cm away from the nozzle exit. The excitation temperatures were calculated by the Boltzmann plot through H_α and H_β atom lines. Measurement conditions for the optical emission spectroscopy are shown in **Table 4.6**.

4.4 Results

4.4.1 Effect of Arc Current on Caffeine Decomposition

Figure 4.8 exhibits generation rates for liquid, gas, and solid where the solid was calculated via mass and carbon balance [16]. The calculation method for the generation rates was explained in section 3.3.2.2. The generation rates in the liquid and gas including the feed rate increased, whereas that of the solid decreased with an increase of arc current. This is due to larger Joule heating at a higher arc current, which accelerates higher evaporation and dissociation of water molecules for CAF decomposition. Here, at lower arc currents at 6.0 A and 7.5 A, the generation rate of solid is higher than that of gas, indicating that arc current has a significant influence on the oxidative environment.

4.4.2 Analysis of Effluent Gas

The gas composition generated during CAF decomposition is shown in **Fig. 4.9**. The main gas products were H_2 (40.9–49.2%), CO_2 (10.0–10.2%), CO (19.3–21.3%), and N_2 (19.3–29.8%). This is good agreement with the equilibrium gas compositions qualitatively as a final product as shown in **Fig. 4.1**. An increase of concentrations in H_2, CO, H, O, NO, and OH was observed from 1700 K with thermal dissociation of water molecules. At over 3000 K, H_2O was fully dissociated into H and O atoms. Also, a significant quantity of OH radicals was produced in a range of 2000–4000 K, with the peak concentration at 3500 K. This denotes that the water plasma could provide a thermodynamically beneficial condition for radical formation. The mole fractions of H_2, CO, and CO_2 increased as arc current increased, which is primarily ascribed to the significantly increased O radicals formed by the dissociation of water molecules. In particular, the H_2/CO ratio is in the range of 2.1 to 2.3, which is highly suitable for the Fischer-Tropsch synthesis (H_2/CO ratio > 2) [17]. Therefore, the water plasma system could be potentially proposed for the synthesis of gas and biofuel production.

4.4.3 Analysis of Effluent Liquid

The effect of arc current on the carbon balance is depicted in **Fig. 4.10**. The carbon balance is a proportion of the total carbon amount for 20 g/L CAF solution to that for solid, liquid, and gas in unit time. The solid products were estimated as 100% carbon. The amount of carbon in solid showed no significant change, while those in gas and liquid were evidently changed. An increase of the amount of higher carbon amount in gas at a higher arc current is attributed to a substantial content of oxygen from dissociated water molecules. Carbons in the CAF molecules thus react more with oxygen and results in higher production of CO and CO_2 than that of liquid.

The nitrogenous compounds presented in **Fig. 4.1** were measured as evidence for the reaction pathway of nitrogen and the CAF decomposition mechanism. The concentrations of ammonium

ion (NH_4^+), nitrite (NO_2^-), and nitrate (NO_3^-) in the effluent liquid were determined in this study as shown in **Fig. 4.11**. The amount of NH_4^+ was the almost same for all arc currents, corresponding to the thermal decomposition of NH_3 due to high temperature [18]. On the other hand, the concentration of NO_2^- dropped and concomitantly NO_3^- increased with the increase of arc current. This can be explained by the formation mechanism in detail as follows: nitrogen oxide (NO) is the dominant gas species under 3500 K which is considered to be an important intermedium for NO_x production through reactions with radicals. The NO is then oxidized into NO_2 and NO_3 by mainly OH and O radicals at lower temperature regions through the following reactions: (i) NO + $\cdot$O → NO_2; (ii) NO + $\cdot$OH → HNO_2; and (iii) NO_2 + $\cdot$OH → HNO_3 [19,20]. Afterward, the generated NH_3, HNO_2, and HNO_3 would be dissolved in the liquid effluent due to the high quenching effect in thermal plasma and in turn become stable aqueous compounds in the liquid such as NH_4^+, NO_2^-, and NO_3^-, respectively [21]. Here, HNO_3 is required to be more oxidized than that of HNO_2, proving that higher oxidation was achieved at a higher arc current and thereby increasing the concentration of NO_3^-.

The TOC and CAF removal rates, and energy yield under different arc currents were studied as shown in **Fig. 4.12**. The result of HPLC analysis for decomposition rate is indicated in **Fig. 4.13**. With the increasing arc current from 6.0 to 9.5 A, the degradation rates were improved in not only the TOC reduction rate from 84.5% to 91.1%, but also in the CAF decomposition rate as high as 97.1–99.8%; thus, the oxidation of CAF molecules was enhanced at higher arc current. On the other hand, the removal rate for TOC is lower than that of CAF, reflecting the formation of various smaller organic intermediates. To calculate energy yield, the mean arc voltage was also measured using an oscilloscope as shown in **Fig. 4.14**. The energy yield decreased with the increasing decomposition rate. This could be explained by the increased power at a higher arc current. In other words, considering Eq. 4.3, the energy yield seems to be more affected by increased power

than that of increased treated solution volume in this study even though a higher arc current leads to a higher feed rate. Nonetheless, the energy yield in water plasma is located at high values than that of other processes such as DBD and AOPs [11,22,23], which is attributed to a one-step process for high concentrated CAF decomposition together with the direct generation of radicals with no other additive chemicals.

4.4.4 Identification of Intermediate Products

IPs in the effluent liquid after decomposition were identified as shown in **Fig. 4.15**. The peak of CAF was dramatically decreased after water plasma treatment compared to 20 g/L CAF solution. Also, it was found that the peak intensities under *m/z* 100 increased with arc current increase. This demonstrates that CAF was decomposed into smaller molecules at a higher arc current in accordance with a higher degree of decomposition rate.

4.4.5 Spectroscopic diagnostic for reactive species

OES spectra were achieved to not only identify excited species but also to study the decomposition mechanism. As shown in **Fig. 4.16**, excited species such as C (247.9 nm), OH (306.4 nm), Cu (318.5 nm), CH (388.8 nm), H_δ (408.2 nm), H_γ (434.0 nm), H_β (486.1 nm), and O (777.9 and 845 nm) were examined at nozzle exit in all conditions. OH, H, and O radicals could be originated from the electron collisions of water molecules ($H_2O + e^- \rightarrow 2{\cdot}H + {\cdot}O + e^-$) molecules as well as the thermal dissociation of H_2O molecules ($H_2O \rightarrow {\cdot}OH + {\cdot}H$) in the plasma [24,25]. Furthermore, the emission intensities of H, OH, and O increased by the increase in arc current and atomic nitrogen was also confirmed in the condition of 9.5 A, proving that higher oxidative and/or reductive environments were achieved due to higher plasma temperatures. The peak of Cu was attributed to vaporization and erosion of the anode and cathode materials.

4.5 Discussion

4.5.1 Plasma Temperature Measurement

The plasma temperature was calculated by the Boltzmann plot method as explained in **Chapter 2**. The intensities of H_α and H_β atom lines are shown in **Fig. 4.17**. Here, the intensity of H_β is higher with an increase of arc current, which is due to the higher arc current needed for ionization of the H atom. As seen from **Fig. 4.18**, the plasma temperature increased with an increase of arc current in a range of 5800–7700 K. Here, the water plasma has three regions according to temperature gradient: (a) arc region, (b) plasma flame region, and (c) downstream region [26]. The plasma temperature calculated is very close to that near the arc region where the highest temperature is observed. Therefore, we can conclude that the higher arc current obviously prompts not only plenty of reactive species but also higher temperature, resulting in finally a higher decomposition rate. The decomposition mechanism was also suggested in accordance with the plasma temperature in the next section.

4.5.2 Decomposition Mechanism of Caffeine

The possible 11 IPs from CAF molecule with different values of *m/z* were postulated by the ESI-MS analysis as shown in **Table 4.7**, in which some of the proposed IPs were also provided in the literature before [27–29]. Taking into consideration the identified IPs by the water plasma, a tentative decomposition mechanism for CAF is proposed in **Fig. 4.19** and discussed.

IP 1 and IP 2 could be generated under electrophilic ·OH attacks to C4=C5 and N9=C8 double bonds, respectively, converting them to weaker single bonds. This is due to low average local ionization energy near the C5, C8, and N9 [30]. Furthermore, they were reported to be thermodynamically stable compounds by exergonic reaction in the previous work [22]. Afterward,

IP 3 can be formed by consecutive hydroxylation to the feeblish C–N bond and H attack to the C4–C5 bond, by which the cleavage of the imidazole ring and the pyrimidine ring occurs, respectively. In addition, IP 4 would be originated by the addition of H at O and N atoms at the same time with the loss of H_2 and CO. MS^2 product ions for IP 2–IP 4 were also studied to confirm their fragmentation patterns as shown in **Fig. 4.20**.

Furthermore, IP 5 could be formed via the electron impact and further O radicals by way of arc and plasma flame regions. The electrostatic potential and average local ionization energy show a low value near the N9 [30], by which the imidazole ring opening could be likely to take place via the electron impact with the high electron energy density in the water plasma arc column [31]. O could be immediately attached for the generation of the aldehyde group, followed by further oxidation into the carboxyl and demethylation from N7 generating CO_2 and H_2O. IP 5 eventually evolved to a further oxidized product noted as IP 6 together with pyrimidine ring opening.

IP 7 is likely the decomposed product by electron dissociation and hydroxylation pathway similar to the mechanism proposed for IP 5 and this intermediate has not yet been reported before. The two carbonyl groups in the CAF molecule act as electron-withdrawing groups, where thus they become electrophilic. Therefore, it is susceptible to being attracted by electrons and radicals, by which the pyrimidine ring could be fractured [23]. Thereafter, with oxidation by O for CO and CO_2 generation, IP 8 also could be formed.

Finally, some of the IPs generated could react more with radicals to produce short-chain organic compounds (*N, N*-dimethylacetamide, glycerol, and oxalic acid) which then eventually would derive micromolecules and/or gaseous [29]. Herein, it was found that the peak intensities under *m/z* 100 increased with arc current increase as discussed in **Fig. 4.15**. This demonstrates that CAF was decomposed into smaller molecules at a higher arc current in accordance with a higher degree of decomposition rate.

4.6 Comparison of Experimental Results with Other Works

Table 4.8 shows some different processes of CAF treatments for the purpose of comparing performance assessment. Other processes used for the decomposition of organic compounds usually need other additive chemicals for activating reactive species. Furthermore, a long treatment time has been taken even if the high decomposition rate. On the other hand, water plasma shows a higher percentage of decomposition even at higher initial concentration and in shorter reaction time without other additive chemicals. Moreover, the energy yield shows a high level, which is due to no additional cooling system and a one-step decomposition process by stable feeding with mist generation.

4.7 Comparison of *N, N*-diethyl-m-toluamide and Caffeine Decompositions

Table 4.9 shows the comparison of the results obtained from DEET and CAF decompositions at 9.5 A in terms of gas composition, plasma temperature, decomposition rate, and energy yield.

In the gas composition, the amounts of H_2 and CO_2 were higher in the DEET decomposition than those in the CAF decomposition. This is considered to be a relatively lower concentration of DEET (2 g/L) and the resultant higher radical reaction from H_2O evaporation and dissociation. Mist consists of H_2O and organic compound, where the content of H_2O increases in the lower concentration of DEET solution (2 g/L) than that of CAF solution (20 g/L). Subsequently, enhanced evaporation and dissociation of H_2O occur for radical generation, which is finally followed by higher generations of H_2 and CO_2.

The plasma temperature was higher in DEET decomposition, which can be also explained from the concentration's point of view. More energy is consumed to decompose more CAF molecules than H_2O. This then makes lower reactivity of radicals including H_α and H_β, which consequently results in lower plasma temperature calculated by the Boltzmann plot method. On the other hand,

the decomposition rate was lower in DEET decomposition. This may be attributed to the stable molecular structure of the benzene ring by the delocalized π bonding [32]. The CAF decomposition showed a higher value of energy yield because of the higher initial concentration.

4.8 Conclusion

Water plasma with mist generation was applied to remove 20 g/L of aqueous Caffeine (CAF) solution. A competent decomposition performance and mineralization of CAF were achieved within a short treatment time. The highest decomposition rate of 99.8% was achieved at an arc current of 9.5 A with a high energy yield of 3.5 g/kWh, which indicates that arc current has a significant effect on the decomposition of organic compounds.

H_2, CO, CO_2, and N_2 were major effluent gaseous, of which the H_2 generation was more than 40% for all conditions. Furthermore, the nitrogenous compounds were investigated for the reaction pathway of nitrogen and the CAF decomposition mechanism. The nitrate (NO_3^-) in the effluent liquid showed a high-level concentration at a higher arc current, which results from further oxidation reaction.

The detailed decomposition mechanism was proposed based on eleven intermediate products through a quadrupole time of flight mass spectrometer (QTOF-MS), in which it was found that electronic dissociation and hydroxylation brought about preliminary decomposition for the imidazole and the pyrimidine rings. It was considered that hydroxylation and electron attack started from near the C5, C8, and N9 due to the low average local ionization energy in the CAF molecule.

In summary, CAF as a representative pharmaceuticals and personal care products (PPCPs) could be decomposed in water plasma. The high decomposition rate was achieved stable mist generation system, which would be of interest and prospective from an environmental viewpoint for processing further harmful organic wastes.

References

[1] K.M. Gani, N. Hlongwa, T. Abunama, S. Kumari, F. Bux, Emerging contaminants in South African water environment-A critical review of their occurrence, sources and ecotoxicological risks, Chemosphere 269 (2021) 128737.

[2] M.V. Capparelli, I. Cipriani-Avila, E. Jara-Negrete, S. Acosta-López, B. Acosta, A. Pérez-González, J. Molinero, V. Pinos-Vélez, Emerging contaminants in the northeast Andean foothills of Amazonia: The case of study of the city of Tena, Napo, Ecuador, Bulletin of Environmental Contamination and Toxicology 107(1) (2021) 2–10.

[3] O.M. Rodriguez-Narvaez, J.M. Peralta-Hernandez, A. Goonetilleke, E.R. Bandala, Treatment technologies for emerging contaminants in water: A review, Chemical Engineering Journal 323 (2017) 361–380.

[4] S. Kleywegt, M. Payne, F. Ng, T. Fletcher, Environmental loadings of active pharmaceutical ingredients from manufacturing facilities in Canada, Science of The Total Environment 646 (2019) 257–264.

[5] G.R. Quadra, J.R. Paranaíba, J. Vilas-Boas, F. Roland, A.M. Amado, N. Barros, R.J.P. Dias, S.J. Cardoso, A global trend of caffeine consumption over time and related-environmental impacts, Environmental Pollution 256 (2020) 113343.

[6] L. Vieira, A. Soares, R. Freitas, Caffeine as a contaminant of concern: A review on concentrations and impacts in marine coastal systems, Chemosphere 286 (2022) 131675.

[7] J.L. Temple, C. Bernard, S.E. Lipshultz, J.D. Czachor, J.A. Westphal, M.A. Mestre, The safety of ingested caffeine: a comprehensive review, Frontiers in Psychiatry 8 (2017) 80.

[8] C.V.T. Rigueto, M.T. Nazari, C.F. De Souza, J.S. Cadore, V.B. Brião, J.S. Piccin, Alternative techniques for caffeine removal from wastewater: an overview of opportunities and challenges, Journal of Water Process Engineering 35 (2020) 101231.

[9] S. Li, B. He, J. Wang, J. Liu, X. Hu, Risks of caffeine residues in the environment: necessity for a targeted ecopharmacovigilance program, Chemosphere 243 (2020) 125343.

[10] T.R. Dias, M.G. Alves, R.L. Bernardino, A.D. Martins, A.C. Moreira, J. Silva, A. Barros, M. Sousa, B.M. Silva, P.F. Oliveira, Dose-dependent effects of caffeine in human Sertoli cells metabolism and oxidative profile: relevance for male fertility, Toxicology 328 (2015) 12–20.

[11] G. Iervolino, V. Vaiano, V. Palma, Enhanced removal of water pollutants by dielectric barrier discharge non-thermal plasma reactor, Separation and Purification Technology 215 (2019) 155–162.

[12] P. Nawrot, S. Jordan, J. Eastwood, J. Rotstein, A. Hugenholtz, M. Feeley, Effects of caffeine on human health, Food Additives and Contaminants 20(1) (2003) 1–30.

[13] S.N. Gummadi, B. Bhavya, N. Ashok, Physiology, biochemistry and possible applications of microbial caffeine degradation, Applied Microbiology and Biotechnology 93(2) (2012) 545–554.

[14] R. Raj, A. Tripathi, S. Das, M. Ghangrekar, Removal of caffeine from wastewater using electrochemical advanced oxidation process: A mini review, Case Studies in Chemical and Environmental Engineering 4 (2021) 100129.

[15] M. Hrabovsky, M. Hlina, V. Kopecky, A. Maslani, P. Krenek, A. Serov, O. Hurba, Steam plasma methane reforming for hydrogen production, Plasma Chemistry and Plasma Processing 38(4) (2018) 743–758.

[16] S. Choi, T. Watanabe, Decomposition of water-insoluble organic waste by water plasma at atmospheric pressure, Journal of Physics: Conference Series (2012) 012003.

[17] A. Tamošiūnas, D. Gimžauskaitė, R. Uscila, M. Aikas, Thermal arc plasma gasification of waste glycerol to syngas, Applied Energy 251 (2019) 113306.

[18] S. Li, J.A. Medrano, V. Hessel, F. Gallucci, Recent progress of plasma-assisted nitrogen fixation research: a review, Processes 6(12) (2018) 248.

[19] M. Pavlovich, T. Ono, C. Galleher, B. Curtis, D. Clark, Z. Machala, D. Graves, Air spark-like plasma source for antimicrobial NO_x generation, Journal of Physics D: Applied Physics 47(50) (2014) 505202.

[20] P. Lamichhane, R. Paneru, L.N. Nguyen, J.S. Lim, P. Bhartiya, B.C. Adhikari, S. Mumtaz, E.H. Choi, Plasma-assisted nitrogen fixation in water with various metals, Reaction Chemistry & Engineering 5(11) (2020) 2053–2057.

[21] P. Peng, P. Chen, M. Addy, Y. Cheng, Y. Zhang, E. Anderson, N. Zhou, C. Schiappacasse, R. Hatzenbeller, L. Fan, In situ plasma-assisted atmospheric nitrogen fixation using water and spray-type jet plasma, Chemical Communications 54(23) (2018) 2886–2889.

[22] T.A. Fernandes, S.G. Mendo, L.P. Ferreira, N.R. Neng, M.C. Oliveira, A. Gil, M.D. Carvalho, O.C. Monteiro, J.M. Nogueira, M.J. Calhorda, Photocatalytic degradation of acetaminophen and caffeine using magnetite–hematite combined nanoparticles: kinetics and mechanisms, Environmental Science and Pollution Research 28(14) (2021) 17228–17243.

[23] J. Wang, Y. Sun, H. Jiang, J. Feng, Removal of caffeine from water by combining dielectric barrier discharge (DBD) plasma with goethite, Journal of Saudi Chemical Society 21(5) (2017) 545–557.

[24] T. Zhang, R. Zhou, P. Wang, A. Mai-Prochnow, R. McConchie, W. Li, R. Zhou, E.W. Thompson, K.K. Ostrikov, P.J. Cullen, Degradation of cefixime antibiotic in water by atmospheric plasma bubbles: Performance, degradation pathways and toxicity evaluation, Chemical Engineering Journal 421 (2021) 127730.

[25] P. Bruggeman, D.C. Schram, On OH production in water containing atmospheric pressure plasmas, Plasma Sources Science and Technology 19(4) (2010).

[26] Narengerile, T. Watanabe, Acetone decomposition by water plasmas at atmospheric pressure, Chemical Engineering Science 69(1) (2012) 296–303.

[27] I. Dalmázio, L.S. Santos, R.P. Lopes, M.N. Eberlin, R. Augusti, Advanced oxidation of caffeine in water: on-line and real-time monitoring by electrospray ionization mass spectrometry, Environmental Science & Technology 39(16) (2005) 5982–5988.

[28] C. Indermuhle, M.J.M. de Vidales, C. Sáez, J. Robles, P. Cañizares, J.F. García-Reyes, A. Molina-Díaz, C. Comninellis, M.A. Rodrigo, Degradation of caffeine by conductive diamond electrochemical oxidation, Chemosphere 93(9) (2013) 1720–1725.

[29] O. Ganzenko, N. Oturan, D. Huguenot, E.D. Van Hullebusch, G. Esposito, M.A. Oturan, Removal of psychoactive pharmaceutical caffeine from water by electro-Fenton process using BDD anode: Effects of operating parameters on removal efficiency, Separation and Purification Technology 156 (2015) 987–995.

[30] M. Li, Q. Mei, D. Han, B. Wei, Z. An, H. Cao, J. Xie, M. He, The roles of HO•, ClO• and BrO• radicals in caffeine degradation: A theoretical study, Science of The Total Environment 768 (2021) 144733.

[31] J. Jenista, Water-vortex stabilized electric arc: II. Effect of non-uniform evaporation of water, Journal of Physics D: Applied Physics 32(21) (1999) 2777.

[32] J. Hicks, P. Vasko, J. M. Goicoechea, S. Aldridge, Reversible, Room-Temperature C—C Bond Activation of Benzene by an Isolable Metal Complex 141(28) (2019) 11000–11003

[33] C. Castañeda, J.J. Martínez, L. Santos, H. Rojas, S.M. Osman, R. Gómez, R. Luque, Caffeine photocatalytic degradation using composites of NiO/TiO_2-F and CuO/TiO_2-F under UV irradiation, Chemosphere 288 (2022) 132506.

Table 4.1. Physicochemical properties of Caffeine.

Molecular Structure	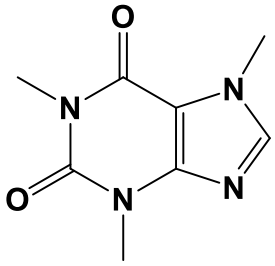
Molecular Formula	$C_8H_{10}N_4O_2$
Chemical Name	Caffeine
Molecular Weight [g/mol]	194.194
Wavelength of Maximum Absorbance [nm]	294
Melting Point [℃]	235–238
Boiling Point [℃]	-
Specific Gravity [-]	1.23
Water Solubility at 25 ℃ [mg/L]	2170

Table 4.2. Experimental conditions for the decomposition of CAF.

Pressure [kPa]	101.3 (Atmosphere Pressure)
Temperature [℃]	25
Arc Current [A]	6.0, 7.5, 9.5
Mean Arc Voltage [V]	119 –137
Plasma Supporting Gas	Water, CAF
CAF Solution Concentration [ppm]	20

Table 4.3. Analysis conditions for high-performance liquid chromatography for effluent liquid analysis.

Equipment		CO-966, PU-980 (Jasco, Japan)
Detector		UV-975
Column	Inner diameter [mm]	4.6
	Length [mm]	250
	Packed column	Inertsil ODS-3V (5 μm)
Mobile Phase (v/v)		Acetonitrile : H_2O = 75 : 25
Flow rate of Mobile Phase [mL/min]		0.8
Column Temperature [℃]		40
Injection Volume [mL]		0.5
Absorbance Wavelength of CAF [nm]		294

Table 4.4. Measurement conditions of total organic carbon for effluent liquid analysis.

Equipment	TOC-L (Shimadzu, Japan)
Carrier gas	Air (99.9%)
Flow Rate of Carrier Gas [mL/min]	150
Combustion Temperature [℃]	680
Dehumidifier Temperature [℃]	0.6
Detect Method	NDIR (Non-dispersive infrared detector)
Injection Volume [μL]	150
Injection Time [-]	3
Dilution Ratio [-]	3–4

Table 4.5. Measurement conditions of quadrupole time of flight mass spectrometer for intermediate products analysis.

Equipment	micrOTOF-Q III (Bruker Daltonics, USA)
m/z scan range [-]	50–1000
Solvent (v/v)	Methanol : H_2O = 50 : 50
Sample Concentration with Solvent [ppm]	10
Flow Rate of Sample [mL/min]	1
Capillary [V]	4500
Nebulizer [bar]	0.3
Flow Rate of Dry Gas [L/min]	4 (N_2)
Dry Gas Temperature [°C]	180
Collision Energy [eV]	35

Table 4.6. Measurement conditions of optical emission spectrometer for detection of reactive species.

Equipment	iHR550 (Horiba Jobin Yvon)
Detector	Charge-Coupled Device (CCD) (1024×256)
Exposure Time [s]	0.1
Entrance Slit [mm]	0.03
Grating [gr/mm]	150
Distance between Plasma and Lens [cm]	50

Table 4.7. Summary of intermediates products determined by QTOF-MS.

Products	Molecular Formula	Proposed Structure	Experimental m/z $[M+H]^+$
Caffeine	$C_8H_{10}N4O_2$	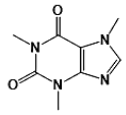	195.0875
IP 1	$C_8H_{12}N_4O_4$	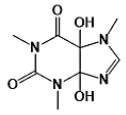	229.07
IP 2	$C_8H_{14}N_4O_5$	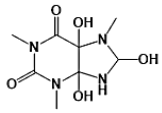	247.2404
IP 3	$C_7H_{11}N_3O_9$	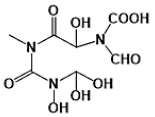	282.2775
IP 4	$C_6H_{13}N_3O_8$	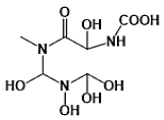	256.2619
IP 5	$C_7H_8N_4O_5$	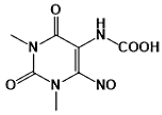	229.07
IP 6	$C_6H_8N_2O_5$	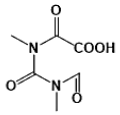	187.8812
IP 7	$C_4H_4N_2O$	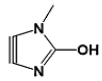	97.098
IP 8	$C_3H_6N_2O_4$	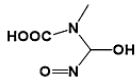	135.1142
IP 9	C_4H_9NO		88.0749
IP 10	$C_2H_2O_4$	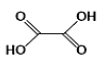	91.0538
IP 11	$C_3H_8O_3$	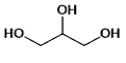	93.0691

Table 4.8. Comparison of the performance of CAF decomposition with other processes.

Process	Initial concentration (ppm)	Tr (min)	Decomposition rate (%)	Additive chemicals	Energy yield (g/kWh)	Ref.
Water plasma	20000	10	99.8	None	3.5	This study
AOPs	20	60	98	Magnetite and hematite	0.006	[22]
AOPs	25	180	90	TiO_2	Not indicated	[33]
DBD	50	24	94	Goethite	0.2	[23]
DBD	50	25	> 90	O_2	0.83	[11]

Table 4.9. Comparison of the results of DEET and CAF decompositions in 9.5 A.

Item		DEET	CAF
Molecular structure		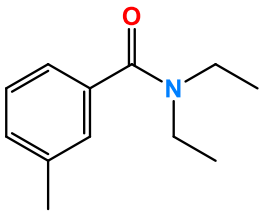	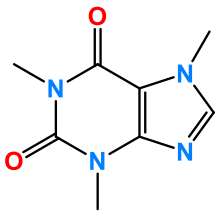
Gas composition [%]	H_2	54.7	49.2
	N_2	18.9	19.3
	CO	13.6	21.3
	CO_2	12.8	10.2
Plasma temperature [K]		8,700	7,700
Decomposition rate [%]		94.8	99.8
Energy yield [g/kWh]		0.3	3.5

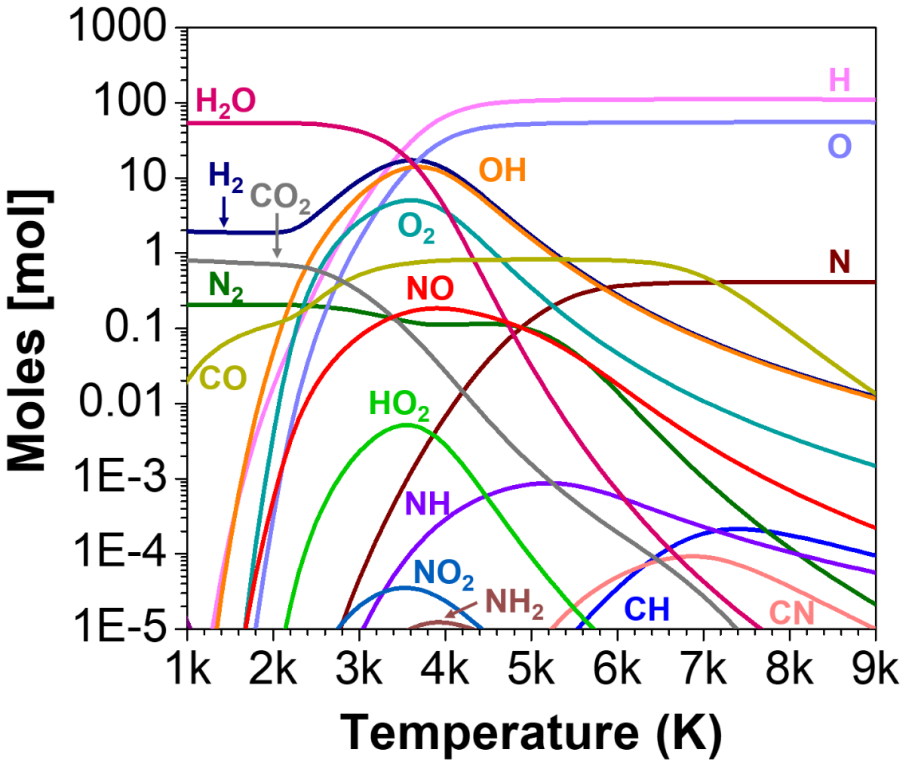

Fig. 4.1. Thermodynamic equilibrium composition of 20 g/L CAF solution.

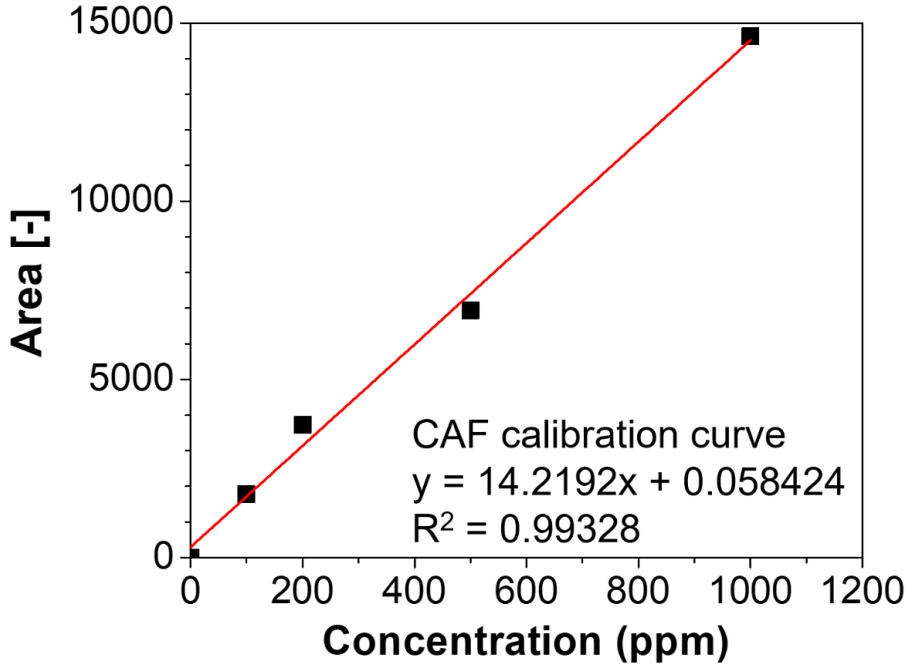

Fig. 4.2. Calibration curve of various concentrated CAF solutions in high-performance liquid chromatography.

$$NH_4Cl + 2K_2HgI_4 + 4KOH \rightarrow HgO.Hg(NH_2)I + 7KI + KCl + 3H_2O$$

Nessler's reagent

Fig. 4.3. Principle of the Nessler reaction for ammonium ion (NH_4^+) quantification.

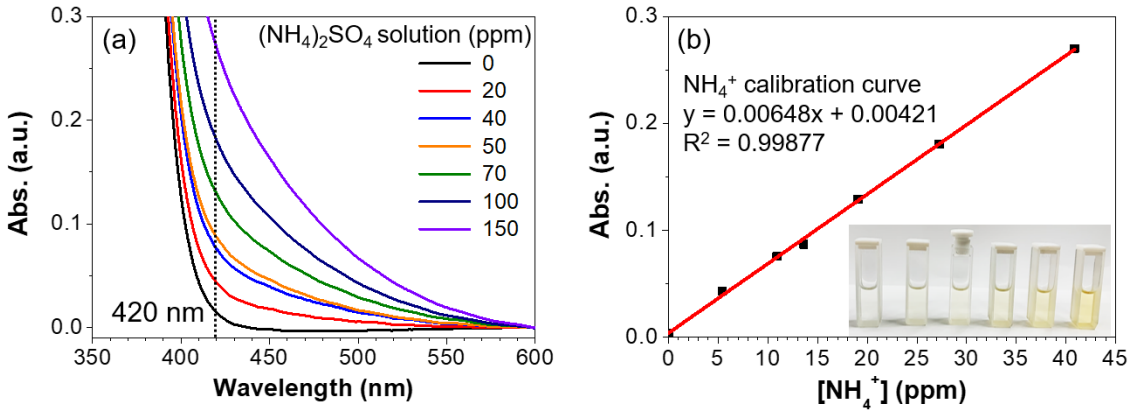

Fig. 4.4. (a) UV-vis spectra of various concentrated $(NH_4)_2SO_4$ solution and (b) the calibration curve of ammonium ion (NH_4^+).

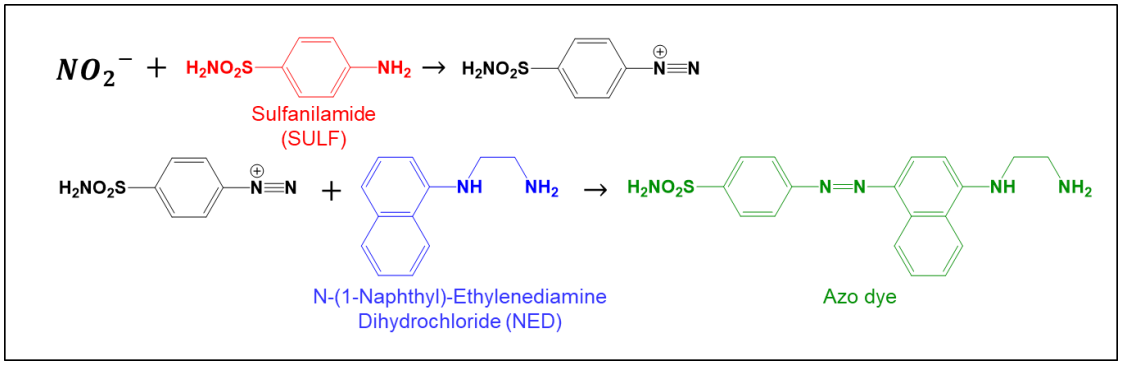

Fig. 4.5. Principle of the Griess reaction for nitrite (NO_2^-) quantification.

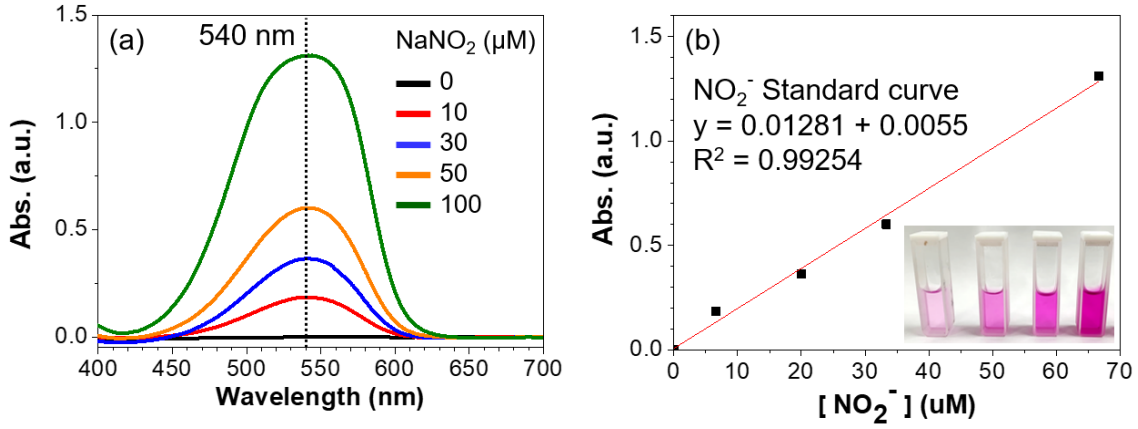

Fig. 4.6. (a) UV-vis spectra of various concentrated $NaNO_2$ solution and (b) the calibration curve of nitrite (NO_2^-).

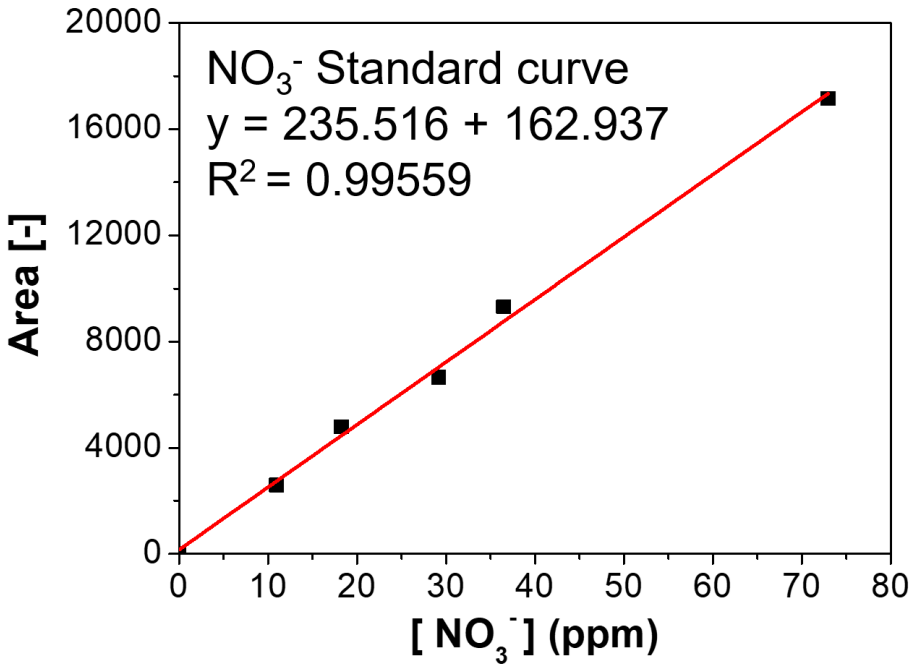

Fig. 4.7. Calibration curve of nitrate (NO_3^-) using $NaNO_3$ solution in high-performance liquid chromatography.

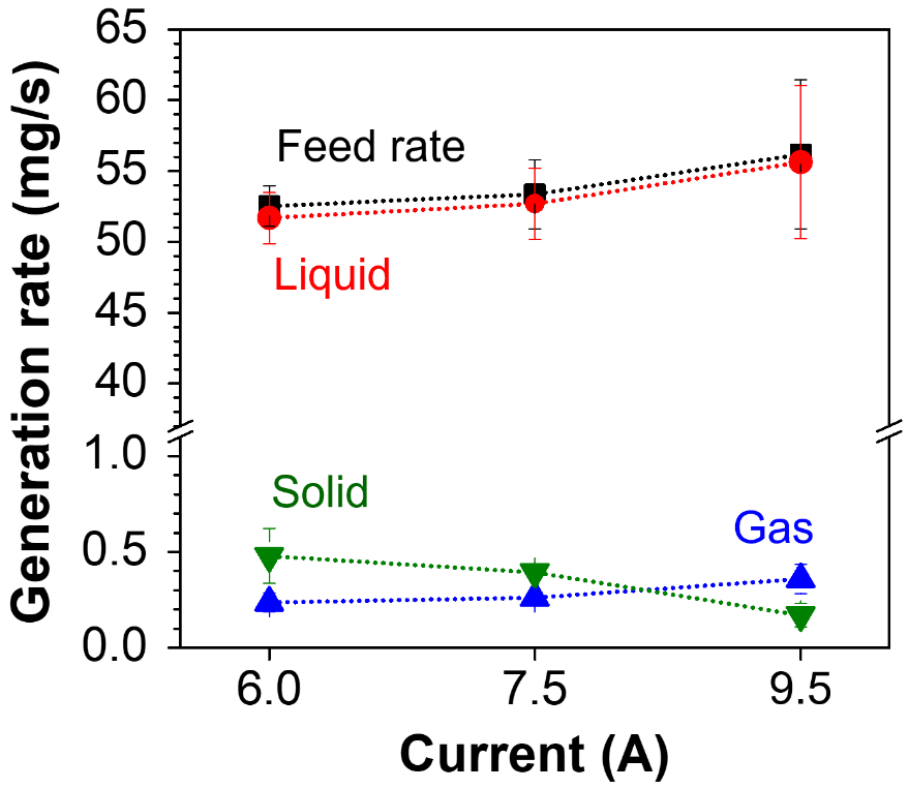

Fig. 4.8. Generation rates of liquid, gas, and solid during the decomposition of 20 g/L CAF at different arc currents.

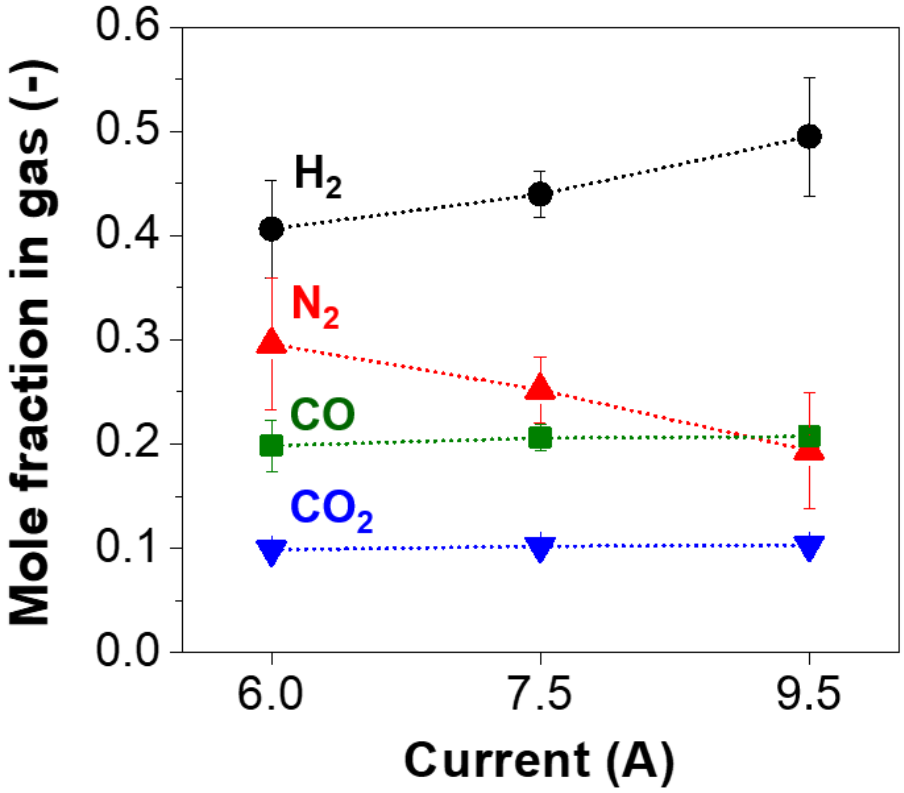

Fig. 4.9. Gas composition generated from 20 g/L CAF decomposition at various arc currents.

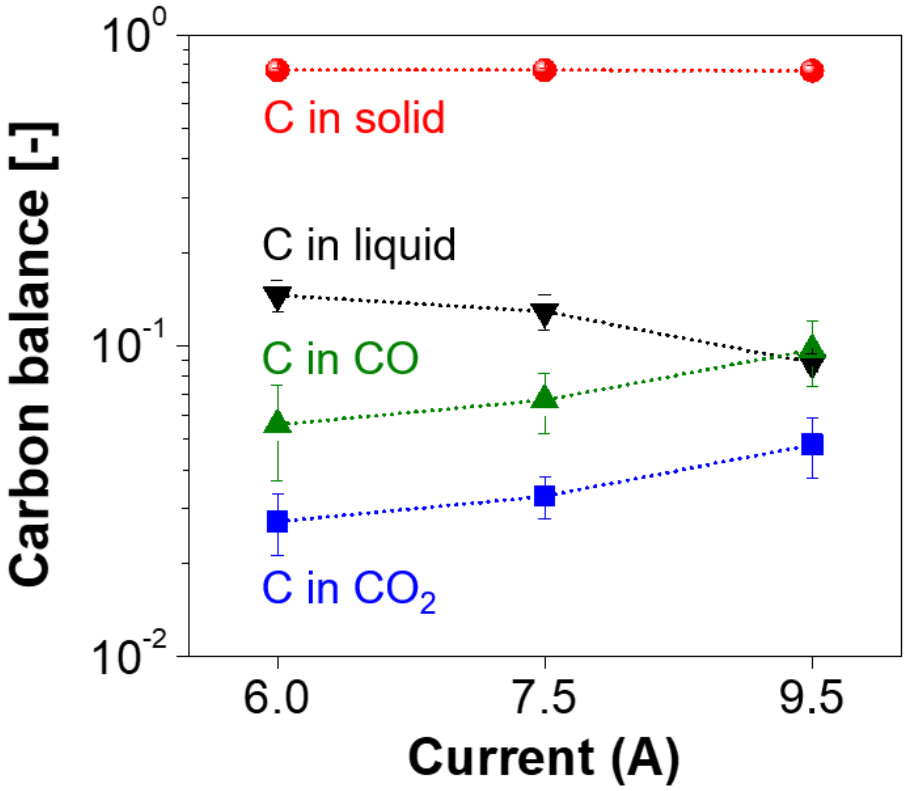

Fig. 4.10. Carbon balance calculated from each phase after decomposition of 20 g/L CAF.

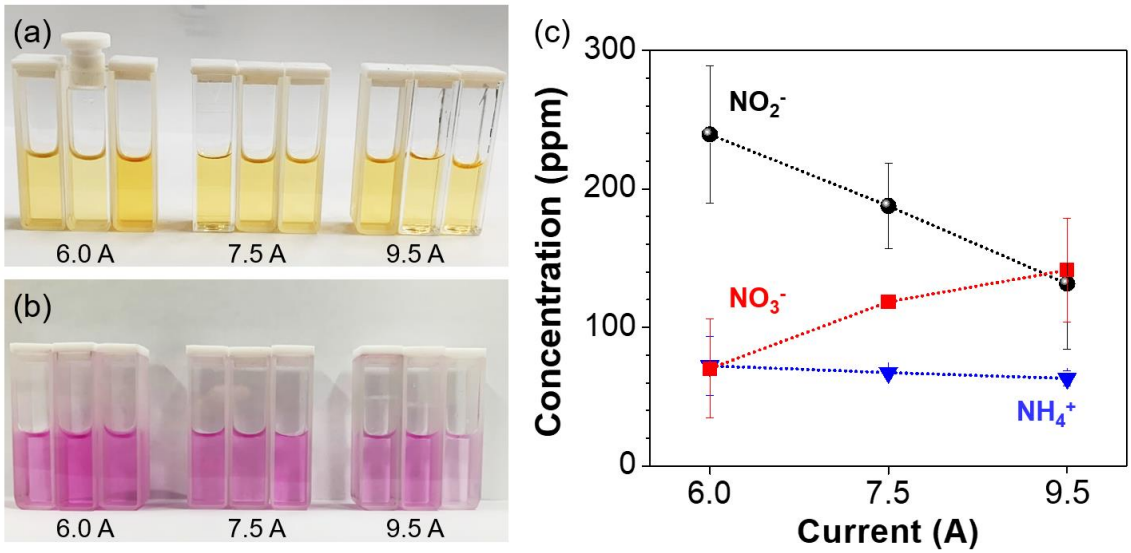

Fig. 4.11. (a) Photographs of result of Nessler test, (b) photographs of result of Griess test, and (c) the concentrations of nitrogenous compounds in the effluent liquid.

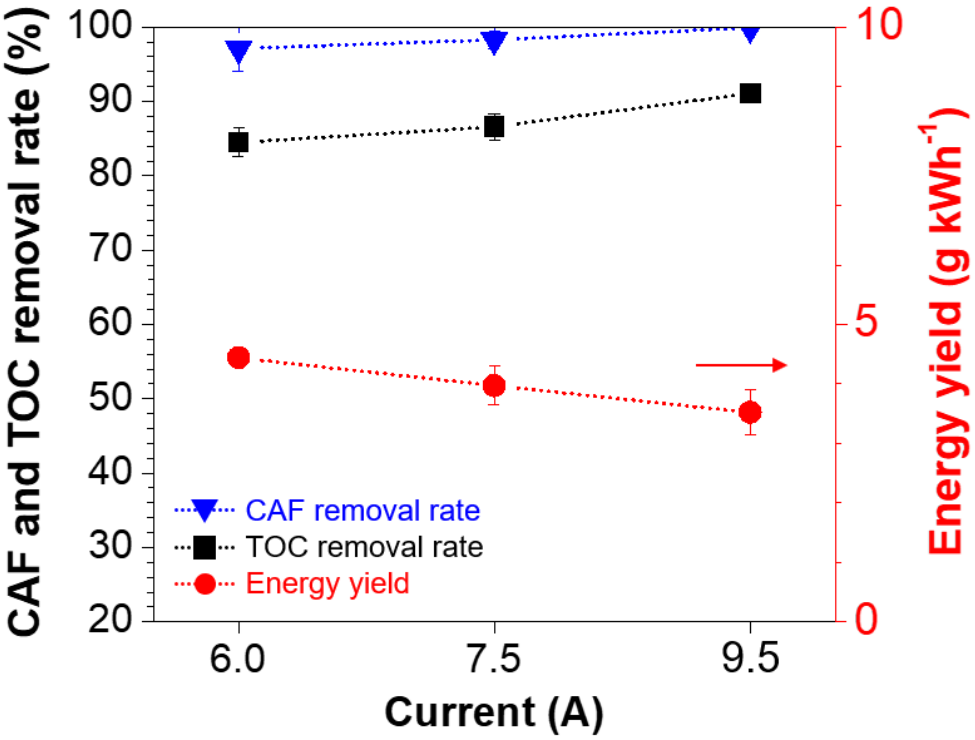

Fig. 4.12. Effect of arc current on TOC and CAF removal rates and energy yield.

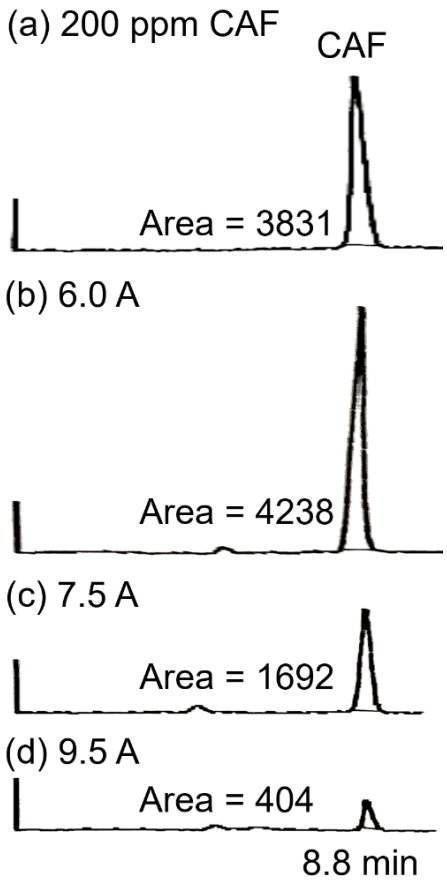

Fig. 4.13. HPLC results of 200 ppm CAF solution and effluent liquids after decomposition of 20 g/L CAF at different arc currents.

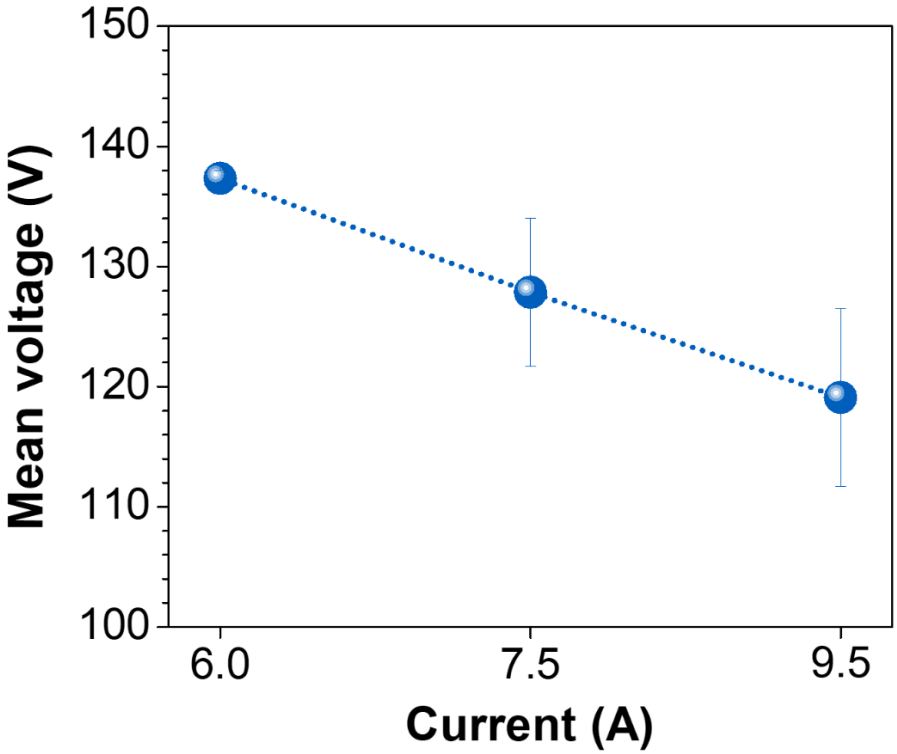

Fig. 4.14. Mean arc voltage at different arc currents.

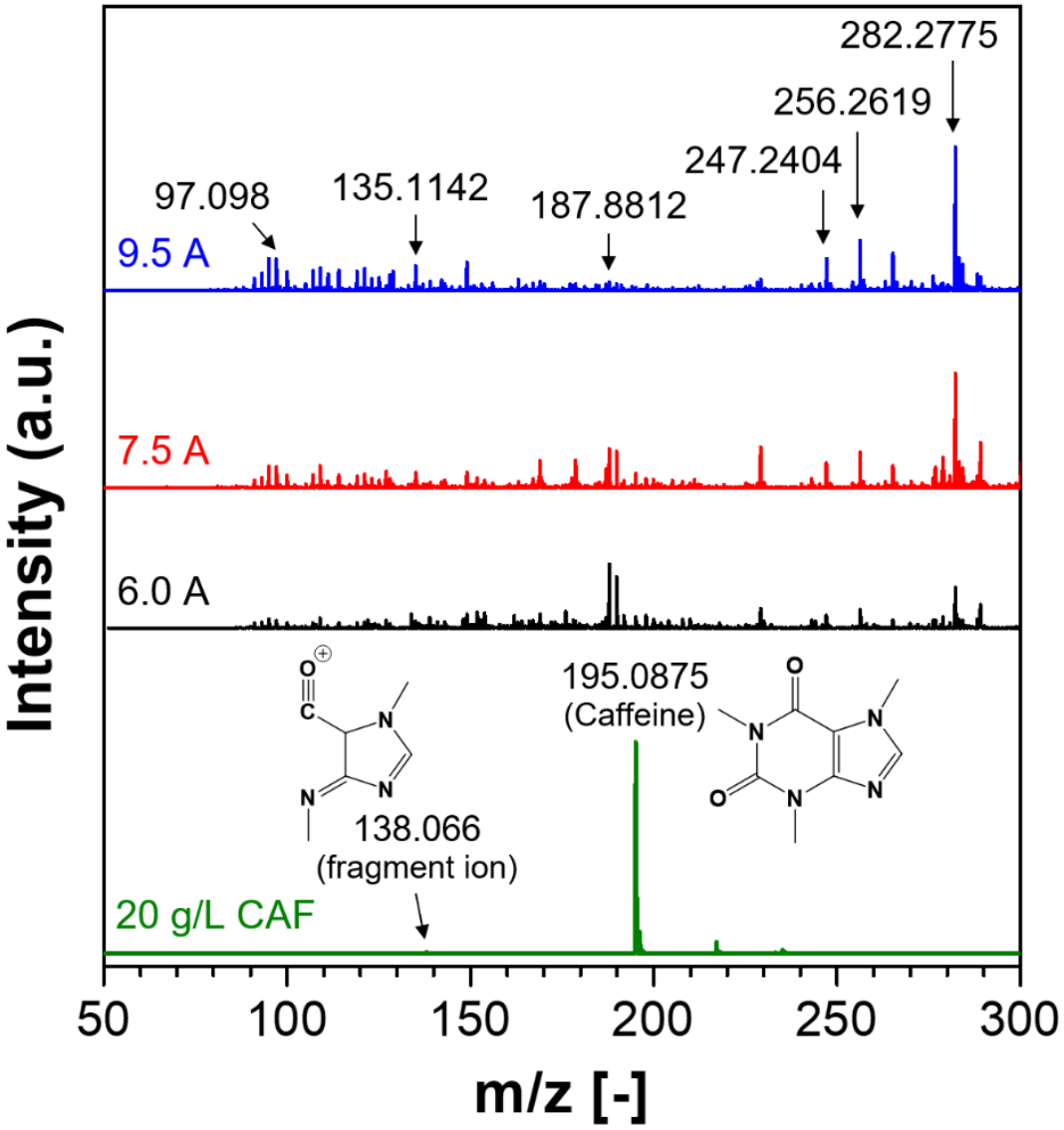

Fig. 4.15. ESI-MS spectra in the positive mode for effluent liquid at different currents.

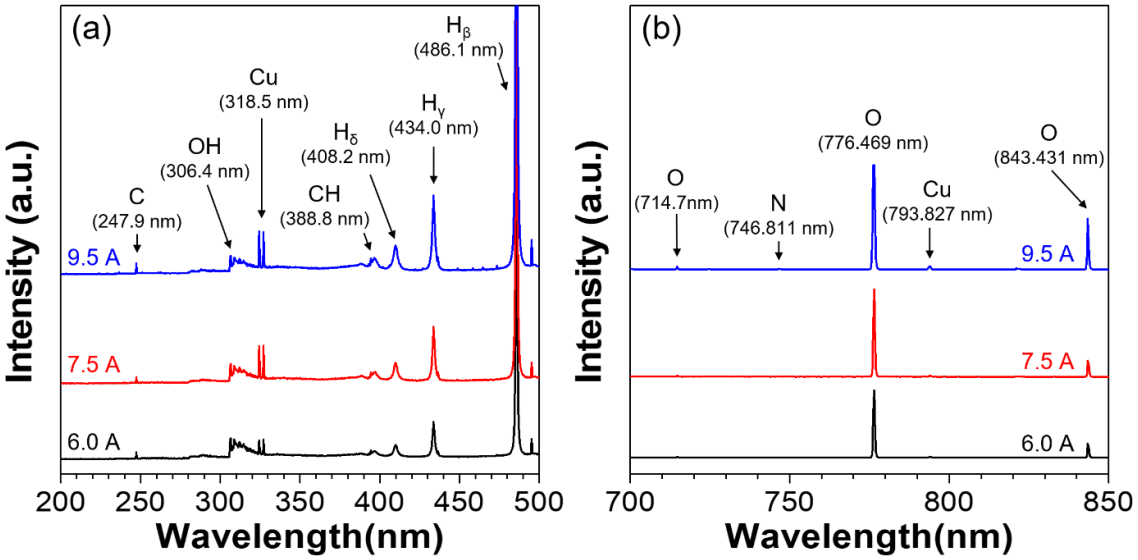

Fig. 4.16. OES spectra during CAF decomposition at (a) 200–500 nm and (b) 700–850 nm.

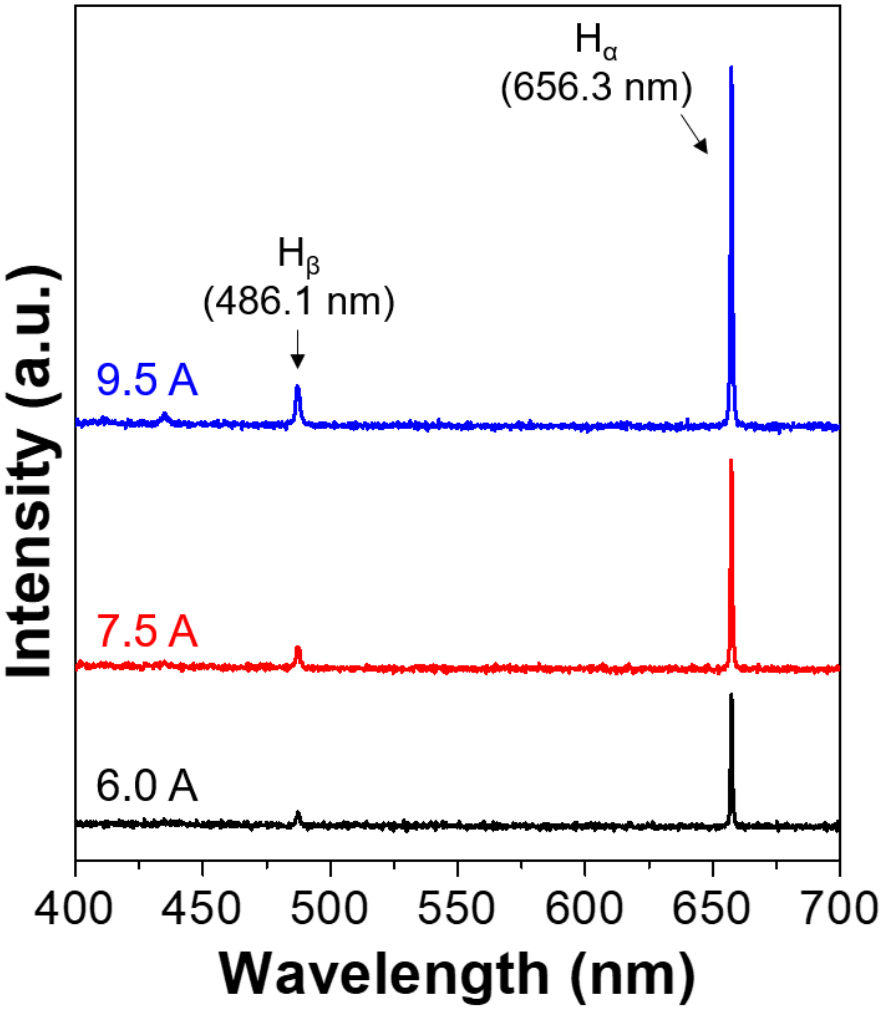

Fig. 4.17. Excited species of H_α and H_β at different arc currents during the decomposition of 20 g/L CAF.

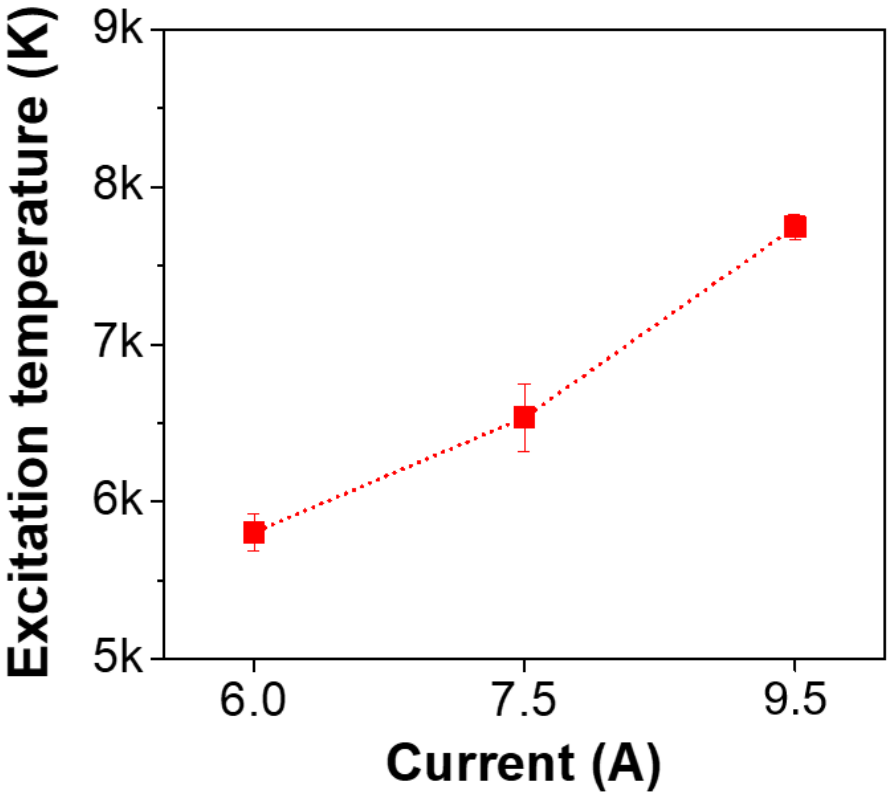

Fig. 4.18. Effect of arc current on the plasma temperature.

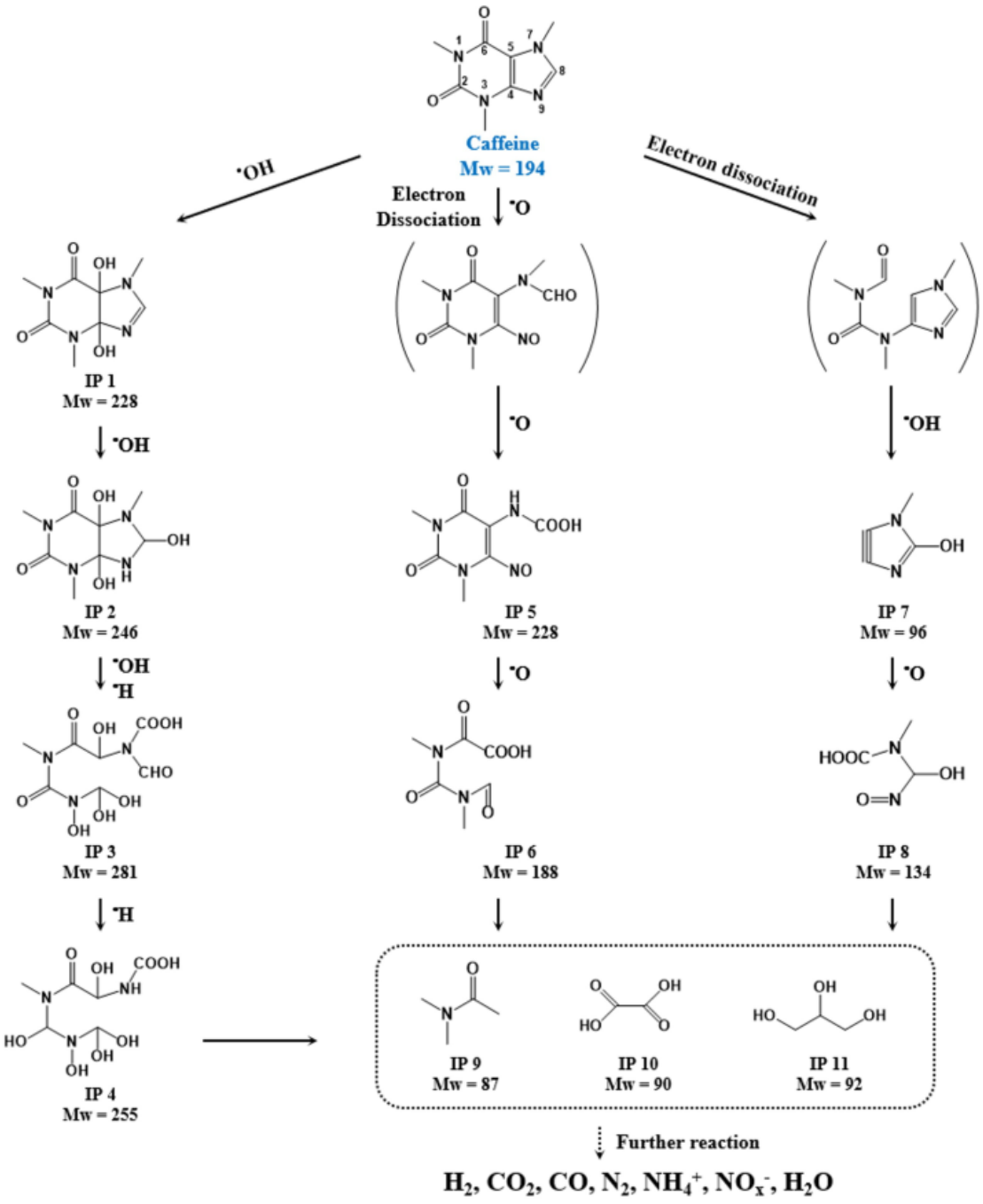

Fig.4.19. Proposed CAF decomposition mechanism.

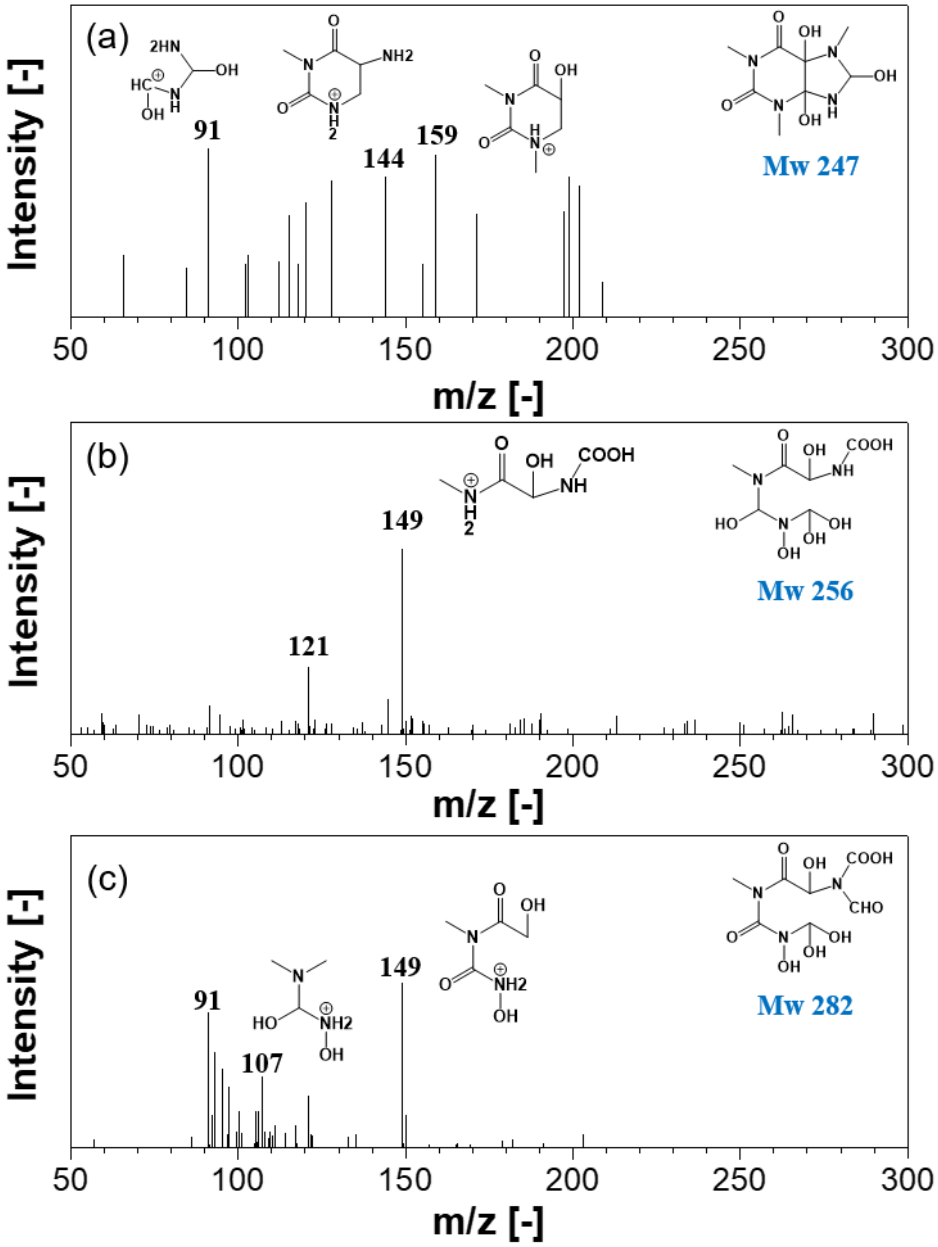

Fig. 4.20. MS^2 spectra obtained in the ESI positive mode for a precursor ion (a) *m/z* $[M + H]^+$ 247, (b) *m/z* $[M + H]^+$ 256, (c) *m/z* $[M + H]^+$ 282, and proposed fragmentation patterns.

5. Conclusion

5.1. Summary and Conclusion

This dissertation focuses on the decomposition of Pharmaceuticals and personal care products (PPCPs) by water plasma with mist generation system. The mist generation system was applied for the stable feed system, and this was proved by the investigation of fundamental arc characteristics. *N, N*-diethyl-m-toluamide (DEET) and Caffeine (CAF) as the most detected PPCPs in the water system were selected as target materials in this study. The gas and liquid effluents, intermediate products, decomposition rates, and further decomposition mechanisms were investigated by various analytic methods. The main conclusion remarks are drawn as follows:

In **chapter 1**, the method of thermal plasma was reviewed based on introductions of plasma definition and applications of thermal plasmas. Furthermore, various waste treatments by thermal plasma were introduced and reviewed with recent research. A major concern in the application of thermal plasma for waste treatment is the disadvantages like the addition of chemicals, high energy consumption, and long-time treatment, which still limits industrial applications. The specific objectives of this dissertation are then introduced.

In **chapter 2**, arc behavior and temperature distribution in water plasma were investigated with mist generation. The mist as plasma gas demonstrated the stable feeding. The effect of mist feeding rate on the arc was examined by speed cameras synchronized with arc voltage measurement. As the mist feeding rate increased, the arc voltage and length increased due to the higher drag force at constant arc current. The arc fluctuation rapidly increased with a restrike phenomenon due to low arc current and high feeding rate. Moreover, the high temperature area was also increased due to the increase of the arc voltage as well as heat convection. Therefore, it was feasible to control the arc fluctuation and area with a high temperature through a flow

parameter. Based on this, the water plasma with a mist generation system is expected to play a crucial role in the practical application of waste treatment and was applied to the decomposition of organic compounds.

In **chapter 3**, the effect of arc current (6.0, 7.5, and 9.5 A) on the decomposition of 2000 ppm *N, N*-diethyl-m-toluamide (DEET) was investigated. The decomposition of DEET was successfully conducted by water plasma method, and the decomposition mechanism was investigated in detail with experimental and thermodynamic calculation results. The highest decomposition rate of 94.8% was obtained at an arc current of 9.5 A with an energy yield of 0.3 g/kWh within 10 min treatment. The contents of H_2 and CO_2 in the effluent gas increased at a higher arc current due to an enhanced oxidative environment. Moreover, the total organic carbon (TOC) reduction rate increased from 69.7 to 91.4% with the increase of arc current. This results from the promoted formation of CO and CO_2 gases through the reactions with O radicals. The hydroxylated DEET molecule was clearly observed in all experimental conditions, which is the main key decomposition route at the early of decomposition. Based on seventeen main intermediates, the decomposition mechanism was proposed in detail, where electronic dissociation attacking weak C–N bond and hydroxylation to the ring structure were predominant factors at the early stage of decomposition. Other byproducts were formed by O and H radicals from the flame region.

In **chapter 4**, the decomposition of a high concentration of 20 g/L Caffeine (CAF) was investigated according to different arc currents. At torch power of 0.8–1.1 kW, the removal efficiency of TOC and CAF increased with an increase of arc current, reaching 92.5 and 99.8% at 9.5 A, respectively. H_2, CO, CO_2, and N_2 were major effluent gaseous, of which the H_2 generation was more than 40% for all conditions. The nitrogenous compounds were measured as evidence for the reaction pathway of nitrogen and the CAF decomposition mechanism. In particular, the concentration of nitrate (NO_3^-) in the effluent liquids was the highest with the

decrease of nitrite (NO_2^-) at 9.5 A, which results from a higher oxidation environment at a higher arc current. The detailed decomposition mechanism was proposed based on eleven intermediate products, in which it was found that electronic dissociation and hydroxylation brought about preliminary decomposition for the cleavage of the imidazole ring and the pyrimidine ring. In particular, OH radical was first considered to attack to double bonds to convert them to weaker single bonds, which are thermodynamically stable compounds.

In summary, the obtained results in the dissertation can improve the understanding of the decomposition mechanism for harmful pharmaceuticals and personal care products in water plasma method, which would be a significant development for the waste treatment toward the green environment

5.2. Future Research Subjects

Pharmaceuticals and personal care products were decomposed by water plasma with mist generation at atmospheric pressure in the dissertation, and some research for the future work are presented as follows:

5.2.1 Additional simulation analysis of plasma jet

The precise control of the DC water plasma process for decomposition of organic compounds is still difficult because of the high quenching rate. Furthermore, radical reactions for the decomposition and byproduct formations occur within a short time. Also, there have been many studies about simulations of DC non-transferred arc and radio frequency plasmas except for the water plasma. The preceded simulation study of plasma flow allows prediction for the practical experiment, which is followed by the process qualities of applications. Therefore, to get more precise results for the application of water plasma, the simulation study will be also combined.

5.2.2 Further decomposition of other pharmaceuticals and personal care products by adding surfactant

Pharmaceuticals and personal care products have basically low solubility characteristic due to their high molecular weight and ring structure of them, which makes it difficult to analyze the decomposition mechanism and select of the target material to be decomposed. High soluble molecules mixed with water generate higher gas generation by reaction of highly concentrated organic compounds with radicals, which would be easy to analyze gas effluent as well as decomposition mechanism. From this point of view, the surfactant that forms micelle structure between the molecules and water can be used. The validation of surfactant for increasing the solubility has been examined with nitrobenzene ($C_6H_5NO_2$), and the solubility increased from 2 to 5 g with adding 0.5 g surfactant. From this preliminary experiment, the range of target material will be broad. Furthermore, this will lead to a detailed understanding of the decomposition mechanism of various compounds.

5.2.3 Further investigation of byproducts

There are many byproducts in water plasma due to complex reactions with radicals and the temperature gradient of the plasma jet. However, the detection of smaller molecules under *m/z* 50 are difficult due to the equipment detection limitation. Therefore, nitrogenous byproducts such as ammonium ions, nitrite, and nitrate were analyzed by thermodynamic calculation and reagents as discussed in **Chapter 4**. For more detailed analysis, gas chromatography-mass spectroscopy (GC-MS) can be used, which can analyze liquids as well as gas effluents for smaller molecules. This will therefore lead to a better understanding decomposition mechanism of pharmaceuticals and personal care products.

Acknowledgements

During the doctoral course, I am thankful to those who have offered me encouragement and support at Kyushu University.

I am deeply indebted to my supervisor, Dr. Takayuki Watanabe, a professor at the Department of Chemical Engineering at Kyushu University. I really feel grateful to Prof. Watanabe for giving me the chance to study interesting research for the Ph.D. course in Japan. His considerate insight and accuracy affected not only research but also life. He has provided me with beneficial help and offered me precious comments during the whole process of the doctoral course, by which I could finish the Ph.D. course. Most of all, Prof. Watanabe always greeted me and the other students with a gentle smile. This was encouraging for me for 3 years whenever I was tired. Lastly, I'm grateful for leaving a memory that I can never forget forever.

I also would like to express my appreciation to Dr. Jun Fukai and Dr. Masahiro Kishida, Professors at the Department of Chemical Engineering, Kyushu University. This dissertation has been finalized thanks to their valuable comments, deliberate suggestions, and sophisticated advice.

I also want to express my gratitude to Dr. Manabu Tanaka, Associate Professor of the Department of Chemical Engineering at Kyushu University. Prof. Tanaka always gave me deliberate advice when I got in trouble with research. Moreover, his passionate attitude to research and lifestyle and warm heart to a person gave me great inspiration for me to make an effort in terms of research and life.

The water plasma teammates are also appreciated for 3 years, Mr. Hiroki Munekata, Mr. Hiiro Murakami, Ms. Minori Itoyama, Mr. Chengyuan Duan, Mr. Sun Qiran, and Mr. Kakeru Nishiyama. I think I must have not finished my dissertation without their help, and the time we

spent together was really valuable.

Furthermore, it was a great honor for me to be with all the staff and members of lab 5 for their cooperation and help. I want to express my thanks to Mrs. Mayumi Matsuzaki, a secretary in our lab. She always gave kindhearted help to students with a smile. I am grateful to Mr. Byeong-il Min, and Ms. Yiran Wang to give me warm advice for the research. Moreover, I want to thank Ms. Eri Kumai for sharing the culture of Japan at 823 every day.

Thanks to Mr. Hirokazu Akamatsu, Mr. Kohei Yamashita, Ms. Aika Tamae, and Mr. Yuki Takemoto, our laboratory could be much supported by their efforts and roles. I also want to show my respect to Mr. Koichiro Fujii, Ms. Ritsu Sogo, and Mr. Ryo Takenaka, who showed their untiring passion for research until late at night.

The financial support from the Korean Scholarship Foundation and the Japan Science and Technology Agency (JST) SPRING, is highly acknowledged.

Last but not least, I sincerely would like to express my heartfelt gratitude to my warm-hearted father, mother, and older sisters. They have given their endless affection and encouragement to me until now and I felt sorry to receive unstinting support alone from them. I will make it up to their love. They are the most precious and loving people to me in the world.

September 2022

KIM SOONHO